Search for collective structures in the ^{186}Os and ^{150}Gd nuclei

Linda Mdletshe

Faculty of Science & Agriculture
Department of Physics

University of Zululand

A thesis submitted in fulfilment of the requirements for the degree of Doctor of Philosophy

Supervisor: Prof. S. S. Ntshangase
co-supervisors: Prof. E. A. Lawrie
Prof. J. F. Sharpey-Schafer
Dr. S. N. T. Majola

April 2022

Declaration

I, Linda Mdletshe, declare that apart from the recognized references and help, the dissertation submitted for the degree of Doctor of Philosophy to the University of Zululand is my own work and has not been submitted to any other University for a degree.

Signature:........................ Date: April 2022

“Only those who will risk going too far can possibly find out how far one can go.”

T. S. Eliot

Abstract

Despite the extensive experimental and theoretical studies that have been conducted on the low-lying positive-parity 0_2^+, 2_2^+, and 4_3^+ states in the transitional deformed nuclei, their microscopic identity remains unclear. It is still one of the major challenges in nuclear structure physics to properly understand the nature of these states. To give more insight on the underlying nature of such states, the excited bands in ^{186}Os and ^{150}Gd nuclei were investigated at iThemba laboratory for accelerator based sciences (iThemba LABS) using the ^{186}W(^{4}He, 4n)^{186}Os and ^{150}Sm(^{4}He, 4n)^{150}Gd reactions. The AFRODITE γ-ray spectrometer was used for detection of γ-ray energies emitted during the experiments.

The decay scheme of ^{186}Os has been improved. In particular, a total of 21 new γ-ray transitions have been added to the level scheme of ^{186}Os. Most importantly, bands built on the excited 0_2^+, 2_2^+, and 4_3^+ states have not only been confirmed but extended up to spins of 12^+, 15^+, and 8^+, respectively. In addition, a number of new linking transitions were identified. Angular distribution and linear polarization measurements were employed to accurately assign spins and parities to the known and new levels in ^{186}Os. The properties of the excited states in ^{186}Os, such as level energies and branching ratios, are interpreted in the context of the systematics of neighboring even-even $^{182-192}$Os isotopes. Furthermore, the validity of the K-selection rule which emanates from a description based on an axially symmetric nuclear shape is examined. The observed decays between the rotational bands support a description where K is conserved. However, some K-forbidden decays were also identified, thus suggesting that a model allowing for small K admixtures is probably required.

The excited bands in this nucleus are compared with the five-dimensional collective Hamiltonian calculations based on covariant density functional theory (5DCH-CDFT), calculations within the quasiparticle triaxial-rotor (QTR) model and predictions by a simple rotational-vibrational model. The 5DCH-CDFT calculations predict that the collective structures are associated with different nuclear shapes, varying in quadrupole deformation, triaxiality and γ-softness.

The decay scheme of ^{150}Gd has been considerably extended. The data did not provide new information on the low-spin states, which was the initial aim of this experiment, however, 31 new transitions were identified at high spins. The present study for these transitions was confined to γ-coincidence analysis. The results for ^{150}Gd are presented in the appendix section.

Keywords

AFRODITE
Fusion evaporation reaction
Gamma-ray spectroscopy
Gamma bands
Angular distribution ratios
Linear polarization asymmetry
Level scheme.

Publications

1. **L. Mdletshe**, X. Q. Yang, E. A. Lawrie, M. A. Sithole, S. N. T. Majola, S. S. Ntshangase, J. F. Sharpey Schafer, J. J. Lawrie, S. H. Mthembu, T. D. Bucher, L. Msebi, R. A. Bark, A. A. Avaa, M. V. Chisapi, P. Jones, S. Jongile, Z. P. Li, L. Makhathini, K. L. Malatji, A. A. Netshiya, Z. Shi, B. Y. Song, L. Wang, J. Xiang, and S. Q. Zhang: *Collective rotational bands at low excitation energy in* ^{186}*Os: vibrational and rotational degrees of freedom.* **Submitted to Phys. Rev. C.**

2. **L. Mdletshe**, S.S. Ntshangase, J.F. Sharpey-Schafer, S.N.T. Majola1, T.R.S. Dinoko, N.A. Khumalo, E.A. Lawrie, R.A. Bark, T.D. Bucher, N. Erasmus, P. Jones, S. Jongile, B.V. Kheswa, J.J. Lawrie, L. Makhathini, K.L. Malatji, B. Maqabuka, J. Ndayishimye, S.P. Noncolela, O. Shirinda, and M.A. Sithole: *Low-lying positive parity bands in* ^{162}*Yb.* **Eur. Phys. J. A 54, 176 (2018)**

3. S. N. T. Majola, M. A. Sithole, **L. Mdletshe**, D. Hartley, J. Timár, B. M. Nyakó, J. M. Allmond, R. A. Bark, C. Beausang, L. Bianco, T. D. Bucher, S. P. Bvumbi, M. P. Carpenter, C. J. Chiara, N. Cooper, D. M. Cullen, D. Curien, T. S. Dinoko, B. J. P. Gall, P. E. Garrett, P. T. Greenlees, J. Hirvonen, U. Jakobsson, P. M. Jones, R. Julin, S. Juutinen, S. Ketelhut, B. V. Kheswa, F. G. Kondev, A. Korichi, W. D. Kulp, T. Lauritsen, E. A. Lawrie, L. Makhathini, P. L. Masiteng, B. Maqabuka, E. A. McCutchan, D. Miller, S. Miller, A. Minkova, L. Msebi, S. H. Mthembu, J. Ndayishimye, P. Nieminen, P. Z. Ngcobo, S. S. Ntshangase, J. N. Orce, P. Peura, P. Rahkila, N. Redon, L. L. Riedinger, M. A. Riley, D. G. Roux, P. Ruotsalainen, J. Piot, J. Saren, J. F. Sharpey-Schafer, C. Scholey, O. Shirinda, J. Simpson, J. Sorri, I. Stefanescu, S. Stolze, J. Uusitalo, X. Wang, V. Werner, J. L. Wood, C.-H. Yu, S. Zhu, and G. Zimba: *First candidates for gamma vibrational bands built on the [505]11/2*$^{-}$ *neutron orbital in odd-A Dy isotopes.* **Phys. Rev. C 101 (2020)**

4. M. A. Sithole, E. A. Lawrie, **L. Mdletshe**, S. N. T. Majola, A. Kardan, T. D. Bucher, J. F. Sharpey-Schafer, J. J. Lawrie, S. S. Ntshangase, A. A. Avaa, R. A. Bark, M. V. Chisapi, P. Jones, S. Jongile, D. Kenfack, T. C. Khumalo, L. Makhathini, K. L. Malatji, B. Maqabuka, S. H. Mthembu, L. Msebi, A. A. Netshiya, G. O'Neill, O. Shirinda, P. M. Someketa, and B. R. Zikhali: *Structure of collective states built on the 11/2$^+$ isomer in ^{187} Os: Quasiparticle-plus-triaxial-rotor model and interpretation as tilted-precession bands.* **Phys. Rev. C 104, 044326 (2021)**

5. M. A. Sithole , J. F. Sharpey-Schafer, E. A. Lawrie, S. N. T. Majola, A. Kardan, T. D. Bucher, J. J. Lawrie, **L. Mdletshe**, S. S. Ntshangase, A. A. Netshiya, P. Jones, L. Makhathini, K. L. Malatji, P. L. Masiteng, I. Ragnarsson, B. Maqabuka, J. Ndayishimye, O. Shirinda, B. R. Zikhali, S. Jongile, G. O'Neill, L. Msebi, P. M. Someketa, D. Kenfack, S. H. Mthembu, T. C. Khumalo, and M. V. Chisapi: *Low- and medium-spin negative parity bands in the ^{187}Os nucleus.* Phys. Rev. C 103 (2021)

6. M.A. Sithole, J.F. Sharpey Schafer, S.N.T. Majola, T.D. Bucher, T.R.S. Dinoko, S.S. Ntshangase, E.A. Lawrie, N.A. Khumalo, S. Jongile, **L. Mdletshe**, R.A. Bark, N. Erasmus, P. Jones, B.V. Kheswa, J.J. Lawrie, L. Makhathini, K.L. Malatji, B. Maqabuka, S.P. Noncolela, J. Ndayishimye, O. Shirinda, B.R. Zikhali, and P.L. Masiteng: *New collective structures in the ^{163}Yb nucleus.* Eur. Phys. J. A 55 (2019)

7. C. Y. Niu, A. C. Dai, C. Xu, H. Hua, S. Q. Zhang, S. Y. Wang, R. A. Bark, J. Meng, C. G. Wang, X. G. Wu, X. Q. Li, Z. H. Li, S. M. Wyngaardt, H. L. Zang, Z. Q. Chen, H. Y. Wu, F. R. Xu, Y. L. Ye, D. X. Jiang, R. Han, C. G. Li, X. C. Chen, Q. Liu, J. Feng, B. Yang, Z. H. Li, S. Wang, D. P. Sun, C. Liu, Z. Q. Li, N. B. Zhang, R. J. Guo, G. S. Li, C. Y. He, Y. Zheng, C. B. Li, Q. M. Chen, J. Zhong, W. K. Zhou, B. J. Zhu, L. T. Deng, M. L. Liu, J. G. Wang, P. Jones, E. A. Lawrie, J. J. Lawrie, J. F. Sharpey-Schafer, M. Wiedeking, S. N. T. Majola, T. D. Bucher, T. Dinoko, B. Magabuka, L. Makhathini, **L. Mdletshe**, N. A. Khumalo, O.Shirinda, and K. Sowazi: *Spectroscopic study of the possibly triaxial transitional nucleus ^{75}Ge.* Phys. Rev. C97, 0556-2813 (2018)

8. S. N. T. Majola, R. A. Bark, L. Bianco, T. D. Bucher, S. P. Bvumbi, D. M. Cullen, P. E. Garrett, P. T. Greenlees, D. Hartley, J. Hirvonen, U. Jakobsson, P. M. Jones, R. Julin, S. Juutinen, S. Ketelhut, B. V. Kheswa, A. Korichi, E. A. Lawrie, P. L. Masiteng, B. Maqabuka, **L. Mdletshe**, A. Minkova, J. Ndayishimye, P. Nieminen,

R. Newman, B. M. Nyakó, S. S. Ntshangase, P. Peura, P. Rahkila, L. L. Riedinger, M. Riley, D. Roux, P. Ruotsalainen, J. Saren, J. F. Sharpey-Schafer, C. Scholey, O. Shirinda, A. Sithole, J. Sorri, S. Stolze, J. Timár, J. Uusitalo, and G. Zimba : *Spectroscopy of low-spin states in* ^{157}*Dy Search for evidence of enhanced octupole correlations.* Phys. Rev. C 100 (2019)

9. S. N. T. Majola, Z. Shi, B. Y. Song, Z. P. Li, S. Q. Zhang, R. A. Bark, J. F. Sharpey-Schafer, D. G. Aschman, S. P. Bvumbi, T. D. Bucher, D. M. Cullen, T. S. Dinoko, J. E. Easton, N. Erasmus, P. T. Greenlees, D. J. Hartley, J. Hirvonen, A. Korichi, U. Jakobsson, P. Jones, S. Jongile, R. Julin, S. Juutinen, S. Ketelhut, B. V. Kheswa, N. A. Khumalo, E. A. Lawrie, J. J. Lawrie, R. Lindsay, T. E. Madiba, L. Makhathini, S. M. Maliage, B. Maqabuka, K. L. Malatji, P. L. Masiteng, P. I. Mashita, **L. Mdletshe**, A. Minkova, L. Msebi, S. M. Mullins, J. Ndayishimye, D. Negi, A. Netshiya, R. Newman, S. S. Ntshangase, R. Ntshodu, B. M. Nyakó, P. Papka, P. Peura, P. Rahkila, L. L. Riedinger, M. A. Riley, D. G. Roux, P. Ruotsalainen, J. J. Saren, C. Scholey, O. Shirinda, M. A. Sithole, J. Sorri, M. Stankiewicz, S. Stolze, J. Timár, J. Uusitalo, P. A. Vymers, M. Wiedeking, and G. L. Zimba: *Beta and gamma bands in* $N = 88$*, 90, and 92 isotones investigated with a five-dimensional collective Hamiltonian based on covariant density functional theory: Vibrations, shape coexistence, and superdeformation.* Phys. Rev. C 100 (2019)

10. B. Ding, C. M. Petrache, S. Guo, E. A. Lawrie, I. Wakudyanaye, Z. H. Zhang, H. L. Wang, H. Y. Meng, D. Mengoni, Y. H. Qiang, J. G. Wang, C. Andreoiu, A. Astier, A. Avaa11, T. Bäck, R. A. Bark, D. Bazzacco, A. Boso8, T. D. Bucher, B. Cederwall, M. V. Chisapi, H. L. Fan, F. Galtarossa, F. H. Garcia, A. Goasduff, G. Jaworski, P. Jones, I. Kuti, J. J. Lawrie, G. S. Li, R. Li, M. L. Liu, Z. Liu, B. Lomberg, B. F. Lv, T. Marchlewski, L. Mdletshe, L. Msebi, S. H. Mthembu, D. R. Napoli, A. Netshiya, M. F. Nkalanga, J. N. Orce, K. Ortner, F. Recchia, S. Riccetto, A. Rohilla, T. W. Seakamela, M. Siciliano, M. A. Sithole, D. Sohler, J. Srebrny, D. Testov, A. Tucholski, J. J. Valiente-Dobón, F. Wentzel, K. Whitmore, Y. H. Zhang, K. K. Zheng, X. H. Zhou, and B. R. Zikhali: *Signature splitting of the* $g_{7/2}[404]7/2^+$ *bands in* ^{131}*Ba and* ^{133}*Ce.* Phys. Rev. C 104, 064304 (2021)

11. D. W. Luo, C. Xu, Y. K. Wang, Z. H. Li, R. A. Bark, S. Q. Zhang, H. Hua, S. Y. Wang, J. Peng, X. Q. Li, H. Y. Wu, X. Wang, C. G. Wu, Q. T. Li, J. Lin, Y. Jin, W. Z. Xu, L. Mu, J. Meng, F. R. Xu, Y. L. Ye, D. X. Jiang, P. Jones, E. A. Lawrie, P. Papka, M. F. Nkalanga, T. D. Bucher, M. V. Chisapi, L. Msebi, S. Jongile, S. Ntshangase, B. R. Zikhali, S. H. Mthembu, T. Seakamela, M. A.

Sithole, O. Shirihda, A. A. Aava, **L. Mdletshe**, K. L. Malatji, S. Mhlongo, and L. Makhathini: *Collective structures in* ^{62}Cu. Phys. Rev. C 105, 024305 (2022)

Acknowledgements

I would like to express my sincere gratitude and appreciation to the following people for making this thesis a success:

- To my supervisors, Prof. S. S. Ntshangase, Dr. E. A. Lawrie, Dr. S. N. T. Majola, and Prof. J. F. Sharpey-Schafer, thank you for the support and guidance you provided throughout the duration of the project. Thank you for the knowledge you have imparted to me. I will forever be grateful to have worked under your supervision.

- To my colleague, Dr. M. A. Sithole, I am extremely grateful to have walked this journey with you. Thank you my brother for your contribution in making this thesis a success.

- Words of appreciation to the AFRODITE collaborators for their assistance during data collection.

- Words of appreciation to iThemba LABS accelerator group for providing the beam, N. Kheswa for preparing the ^{150}Sm targets, and John Simpson and the STFC Daresbury Laboratory for supplying the ^{186}W targets.

- I am grateful to iThemba labs staff, Unizulu department of physics staff, and UWC department of physics staff for their support and assistance.

- I am grateful to my family and friends for their support and encouragement.

- Last but not least, I would like to thank the National Research Foundation and Unizulu research office for their financial assistance. This research project would not have been possible without their support.

Contents

List of Figures

List of Tables

Chapter 1

Introduction and scientific motivation

1.1 Introduction

One of the fundamental aims of nuclear structure physics is to understand the shapes of different atomic nuclei across the nuclear chart and the structure of the excited states that correspond to each shape. The nuclear shape is often described by the nuclear density distributions with respect to the three principal nuclear axes (x, y, z). The nuclear shape can vary from spherical to ellipsoidal depending on the quadrupole and triaxial deformation parameters (β, γ). The most important nuclear shapes are spherical, deformed with axial symmetry, and deformed without axial symmetry. Nuclei with spherical shapes have equal principal axes $(x = y = z)$. One of the most important features of spherical nuclei is that they have zero quadrupole moment. When a nucleus breaks spherical symmetry, it becomes deformed. For a deformed axially symmetric shape, one of the nuclear axes becomes longer (or shorter) than the other two axes $(x = y \neq z)$. Nuclei with such unequal principal axes are not spherical, and they have a non-zero quadrupole moment. The deformed axially symmetric nuclear shapes are prolate and oblate shapes, see Fig. 1.1.

When a nucleus breaks the axial symmetry, it becomes axially asymmetric (or triaxially deformed). The three principal axes of the nuclear density distributions become unequal $(x \neq y \neq z)$. The principal axes that describe the triaxial shape are the short, intermediate, and long axes. The moment of inertia with respect to the intermediate axis is the largest and thus low energy is required to rotate a nucleus around this axis.

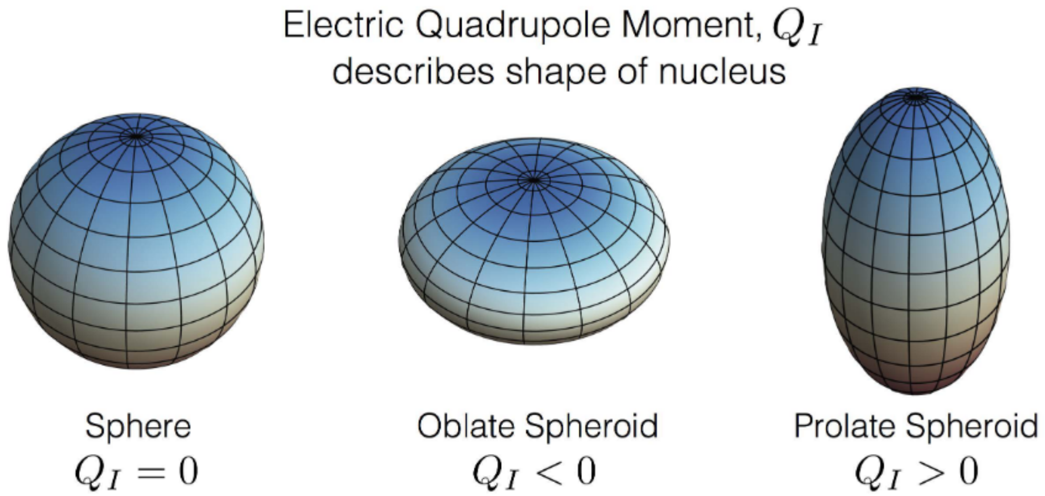

FIGURE 1.1: Electric quadrupole moment describing the nuclear shapes.

Triaxially deformed nuclei can be γ-soft or γ-rigid. When a nucleus is in the γ-soft mode, it oscillates easily around an average triaxial deformation, moving freely in the γ direction. A triaxial nucleus in a γ-rigid mode, does not undergo shape oscillations, as the lengths of the nuclear axes remain fixed.

1.2 Scientific motivation

Experimentally, nuclear shapes are determined through the detailed study of the nuclear properties of the excited states of the nuclei such as level energies, spins and parities. Considerable progress has been made in identifying and explaining the experimentally observed levels in many nuclei, including spherical and deformed nuclei. However, understanding and explaining in detail the properties of the excited non-yrast states remains a major challenge in nuclear structure physics for most nuclei.

The present study focuses on identifying and understanding the structure of deformed even-even nuclei, particularly those that lie in the transitional region – the region where nuclear shape changes rapidly from spherical to a well deformed shape. The nuclei in the transitional region are often moderately deformed, and consequently undergo collective motions such as rotations and vibrations. Thus, such nuclei can have excited levels that are formed as a result of nuclear rotation or vibration. Typical rotational and vibrational bands are shown in Fig. 1.2.

The nucleus of interest, ^{186}Os, has 76 protons and 110 neutrons, and is one of the nuclei that is located in the transitional region. Understanding the collective structures in the Os isotopes that are located towards the end of the $N = 82 - 126$ shell is currently a subject of great interest in nuclear structure physics [1–4]. In the even-even $^{182-192}$Os isotopes, the 2_2^+ and 4_3^+ states have been interpreted in various different ways. Interestingly, these isotopes have 2_2^+ γ bands at very low energy and their excitation energies decrease with neutron number, see Fig. 1.3. In effect, the excitation energy of the 2_2^+ band head in ^{192}Os has the lowest excitation energy in the entire nuclear chart. This shows that the nuclear shapes are strongly affected by the triaxial degree of freedom. However, whether the shape corresponds to a rigid triaxial shape, or is axially symmetric on average, but affected by γ vibrations, remains a controversial topic.

The various investigations of the observed rotational bands at low spins, including the 2_2^+ and 4_3^+ bands in the Osmium even-even isotopes have been a subject of great interest in the nuclear structure community because their features may shed light on the corresponding nuclear shapes. The observed 4_3^+ bands have been interpreted in several alternative ways, e.g. (i) as due to two-phonon γ vibrations [1], or (ii) involving proton excitations and hexadecapole deformation [5], or (iii) as possibly due to the rotation of an axially asymmetric shape. The 4_3^+ band heads in the Os isotopes are positioned at almost exactly twice the excitation energy of the 2_2^+ band heads, making them the most ideal candidates for two-phonon excitations [1] . However, these band heads are strongly populated in stripping and pick-up reactions as well as in elastic scattering [3, 5–7]. This suggests that they have an important proton contribution in their wave functions. Bands based on particle-hole excitations can have strong $M1$ transitions between even- and odd-spin members of the band while a hexadecapole shape will allow $E4$ excitations to populate the 4^+ band head directly from the ground state.

The Coulomb excitation data of Wu et al. [1] have been reanalyzed by Allmond et al. [2] using their triaxial model which corresponds to a rotation of rigid triaxial nucleus and does not involve phonon excitations. They find that triaxiality improves the agreement with experiment for the 2_2^+ bands but not for the 4_3^+ bands. In a phonon model $E_{4_3^+}/E_{2_2^+}$ = 2, whereas in a rigid triaxial model this ratio depends on the γ deformation, it is approximately 4 for $\gamma = 30°$.

It should be noted that the available information on the 4_3^+ bands in these Os nuclei is scarce, see Fig. 1.3, particularly for the lighter isotopes where the experimental data is limited to the first two states only. Thus, to give more insight into the underlying microscopic identity of the low-lying bands in the Os isotopes, we performed an experiment on ^{186}Os, and compared the results with those of the neighboring Os isotopes. The features of the linking transitions between the low-energy bands were also re-examined. The 4_3^+ band was extended up to higher spins. These findings are discussed in terms of a comparison with the corresponding expectations from a simple vibrational-rotational model and from a triaxial rotor model. In addition new results from the five-dimensional collective Hamiltonian coupled with the covariant density functional theory (5DCH-CDFT)

[8, 9] for the 4_3^+ band are presented. Similar calculations have been used to reproduce the experimental observations for the low-lying 0_2^+ and 2_2^+ bands in the $A \sim 160$ mass region [10] and for a systematic study of the nuclei in the Er to Pt region [11].

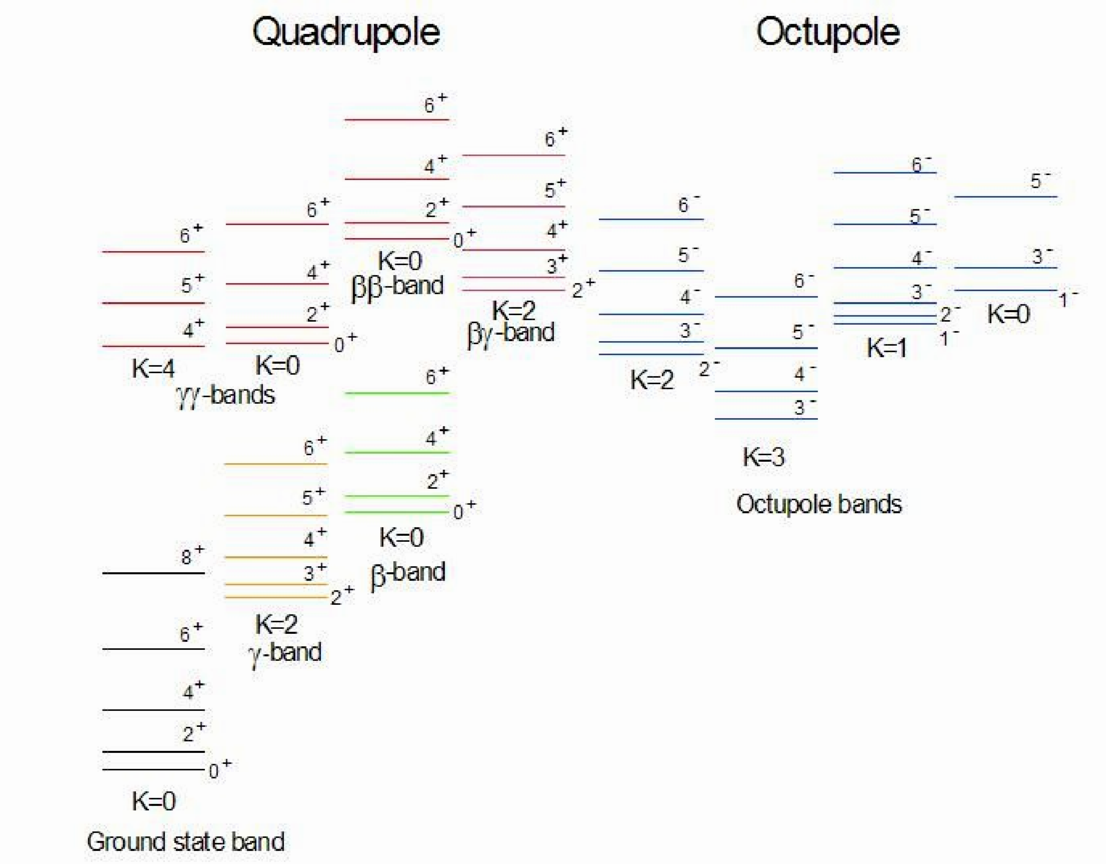

FIGURE 1.2: Typical vibrational and rotational levels of deformed nuclei.

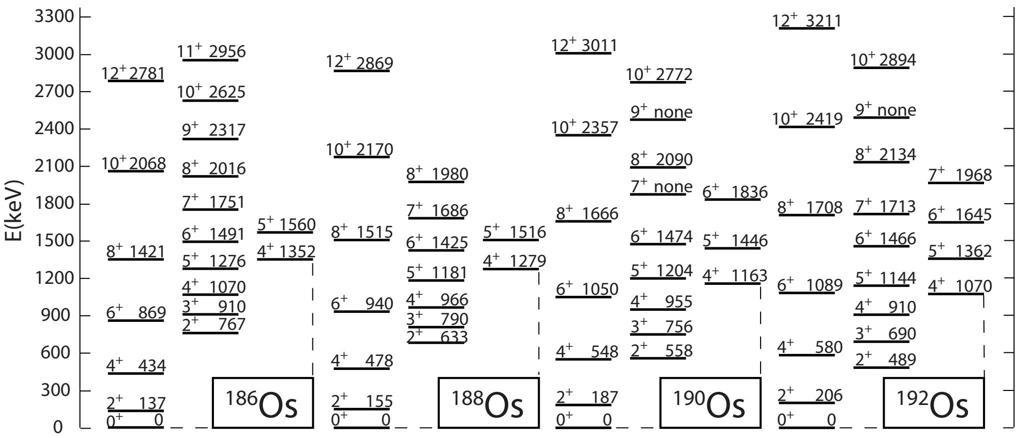

FIGURE 1.3: Excitation energy levels for the ground-state, 2_2^+ and 4_3^+ bands in the even-even $^{184-192}$Os isotopes [2].

Chapter 2

Nuclear structure theory

Ever since the discovery of the atomic nucleus, a number of models to describe the nuclear behaviour have been developed [8, 12–19]. Some of the most popular, successful, and widely used models to explain and predict nuclear behavior are liquid-drop and shell models and also rotational and vibrational models. The liquid-drop and the shell models describe a nucleus as if it was behaving like something else by analogy. The liquid-drop model describes a nucleus as if it was behaving like a drop of liquid, and the shell model describes the nucleons in a nucleus as if they were moving independently in a common potential, like the electrons in an atom. These models are discussed below.

2.1 Liquid-drop model

The Liquid-drop model [20–22] is one of the models that was able to account for prominent aspects of nuclear properties and behaviour. The basic assumption of this model is that each nucleon in a nucleus interacts only with its neighbors like a molecule in a liquid. The analogy with a drop of liquid is extremely useful in understanding certain aspects of nuclear behaviour. A picture of a nucleus as a drop of liquid permits the correlation of many facts about the nuclear masses and binding energies, and it is useful in explaining nuclear fission. Despite the success of the model in explaining some important features of the nuclei, there are other features that cannot be described by the model. For instance the high stability of nuclei with magic numbers of nucleons and the concept of pairing cannot be explained using this model.

2.2 Spherical nuclear shell model

The nuclear shell model [23–25] requires that each nucleon in a nucleus interacts mainly with an averaged nuclear potential produced by all other nucleons. The nucleons in a nucleus are described as moving independently in this potential, like the electrons move in the Coulomb potential inside an atom. The description follows quantum mechanics rules, so specific quantum states are permitted and no more than two nucleons (of the same type) can occupy each state. The electrons in an atom occupy states that are grouped in shells and are described by four quantum numbers: n, l, m_l, and m_s. The degree of occupancy of the outermost shell determines important aspects of the behaviour of an atom. For instance, atoms that have all their electron shells completely filled have high binding energies and are highly stable. The same kind of effect is observed with respect to nuclei. Nuclei that have 2, 8, 20, 28, 50, and 82 protons or neutrons or 126 neutrons are more stable than other nuclei of similar mass numbers [26]. Such nuclei are known as magic nuclei and have zero quadrupole moments (the measure of how much the nuclear charge distributions depart from sphericity), and hence have spherical shape.

The spherical shell model, uses a modified harmonic oscillator potential with ℓ^2 and spin-orbit ($\ell.s$) terms added to the standard harmonic oscillator potential. It has the same radial dependence along all three nuclear axes and is often applied to describe the nuclear phenomena. The nucleon states are characterized by the following quantum numbers: principal (n), orbital angular momentum (ℓ), and total angular momentum (j). The total angular momentum j is obtained by coupling the intrinsic spin momentum s and the orbital angular momentum ℓ. One of the successes of the nuclear shell model is its ability to predict the properties of the ground and excited states in many spherical nuclei. All protons and neutrons in even-even nuclei are paired off, and their angular momenta cancel out to give a ground-state spin of zero. The ground-state spin in odd-mass nuclei is determined by the half-integer angular momentum of the unpaired nucleon occupying the closest to the Fermi level shell-model state. In the odd-odd nuclei the ground-state spin is obtained by combining the half-integer angular momenta of the two unpaired nucleons. Excited states are generated by promoting an odd nucleon to a higher-energy shell-model state.

The spherical nuclear shell model is successful in describing spherical nuclei near magic numbers, however, it fails to describe the structure of nuclei that have many valence nucleons outside closed shells. The model cannot explain the properties of nuclei with large deformation. Thus, a model that can account for the effect of deformation in nuclei had to be developed.

2.3 Deformed shell model

In the early 1950s, Sven Gösta Nilsson developed a model for deformed nuclei by modifying the spherical harmonic oscillator potential [13]. The deformed harmonic oscillator potential has a radial dependence and includes the spin-orbit ($\ell.s$), and the ℓ^2 terms. The model was developed for nuclei with considerable quadrupole deformation and axial symmetry. The presence of quadrupole deformation splits the degenerate energy levels of the spherical shell model. In the spherical shell model, all the states with the same total angular momentum j have the same energy. However, in the deformed shell model their energies depend on the projection Ω of the total angular momentum j along the symmetry axis (z-axis). The larger the deformation ε_2, the larger the energy difference between the states emanating from the same j sub-shell having different projections Ω.

The Nilson diagrams for neutrons and protons are shown in Figs 2.1 and 2.2. Each state within the Nilsson model is characterized by $[N, n_z, \Lambda]\Omega^\pi$ quantum numbers, and the parity of each state is defined as $\pi = (-1)^\ell$. N is the number of the oscillator shell (principal quantum number), n_z is the number of the oscillator quanta along the z-axis, Λ is the projection of the orbital angular momentum ℓ of the nucleon along the z-axis, Ω is the projection of the total angular momentum j of the nucleon on the symmetry axis, $\Omega = \Lambda \pm \Sigma = \Lambda \pm 1/2$ where Σ is the projection of the spin angular momentum s of the nucleon along the z-axis.
The prolate and oblate nuclear deformations are represented by positive and negative values of ε_2, respectively. The orbitals with low Ω have the lowest energy among the orbitals emanating from the same j sub-shell for prolate, and highest energy among these orbitals for oblate shape, respectively. There are some instances where the protons and the neutrons favour different shapes. In such cases, the nucleus may become triaxially deformed.

One interesting feature that many deformed nuclei exhibit is shape coexistence. It is observed when the total energy of the nucleus is similar for two or more different shapes. Thus the nucleus can exist in any of these shapes. The ^{186}Pb nucleus is one of the cases where shape coexistence was reported [27]. Three different shapes were observed in ^{186}Pb, where the ground state corresponds to spherical shape, while two excited 0^+ states correspond to prolate and oblate shapes, respectively.

The Nilsson model has been successful in accounting for most of the experimentally observed features of single-particle levels in a number of deformed nuclei. One of the important properties of the deformed shell model is that the total angular momentum j of a nucleon is not a good quantum number but the projection Ω is a good quantum number. A schematic illustration of the coupling of angular momenta for a deformed

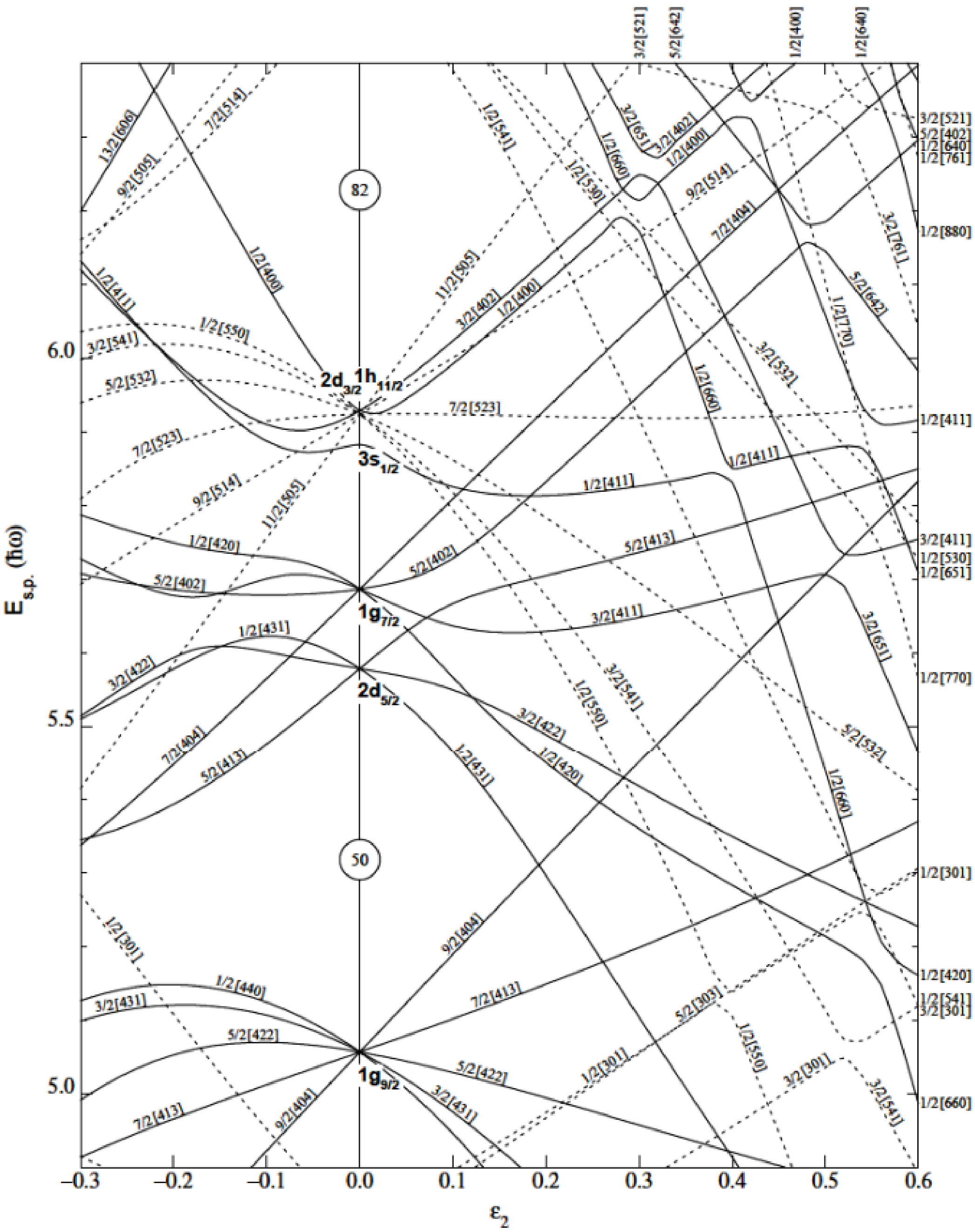

FIGURE 2.1: Nilsson diagram showing the single-particle proton energies as a function of quadrupole deformation ε_2. The orbitals are described by the $[Nn_z\Lambda]\Omega^\pi$ quantum numbers. The solid lines represent the states with positive parity $\pi = +1$, and the dashed lines represent those with negative parity $\pi = -1$.

nucleus is illustrated in Fig. 2.3, showing the projections Λ, Σ, and Ω of the single particle angular momenta $\vec{l}$, $\vec{s}$, and $\vec{j}$, respectively.

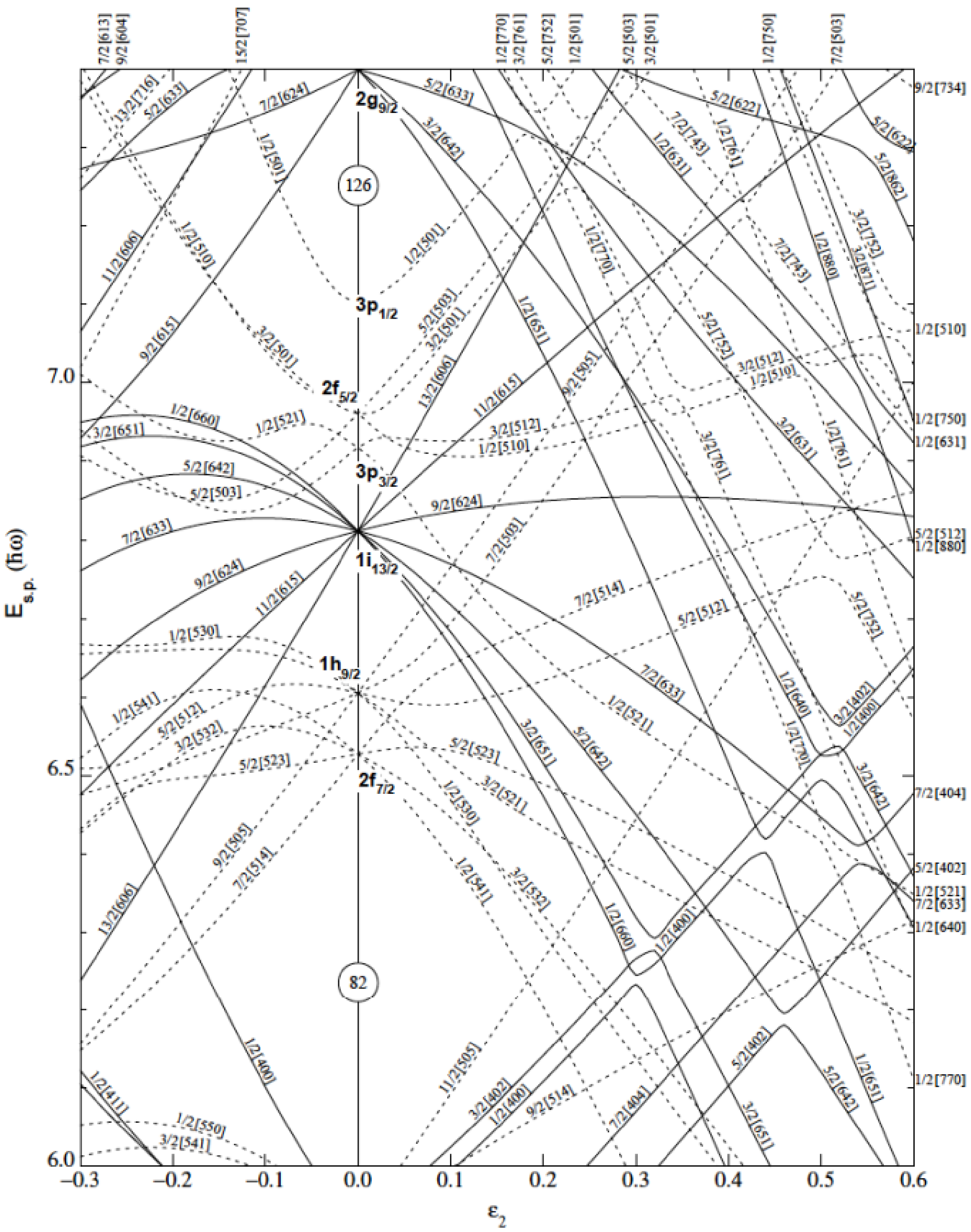

FIGURE 2.2: Nilsson diagram showing the single-particle neutron energies as a function of the quadrupole deformation ε_2. The orbitals are characterised by the $[Nn_z\Lambda]\Omega^\pi$ quantum numbers. The solid lines represent the states with positive parity $\pi = +1$, and the dashed lines represent those with negative parity $\pi = -1$.

2.4 The Collective Model

The nuclear collective model of A. Bohr and B. Mottelson [28] describes the collective behaviour of nuclei. The model takes into account the effect of a non-spherically symmetric potential, which leads to a large deformation in many nuclei and consequently large electric quadrupole moments. In the collective model, many nucleons contribute

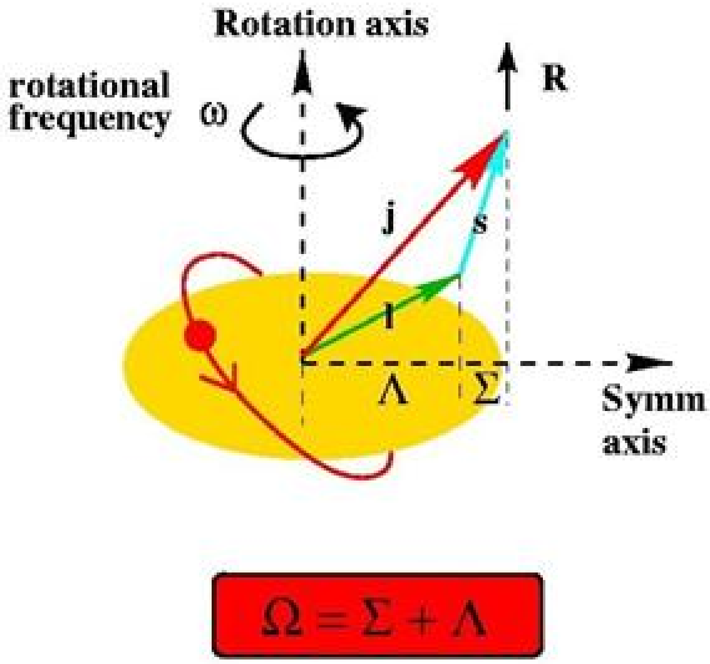

FIGURE 2.3: Schematic of coupling of angular momenta for a collective rotation of an axially deformed nucleus. Ω is the projection of the total angular momentum j of the nucleon on the symmetry axis. Λ is the projection of the orbital angular momentum ℓ of the nucleon along the z-axis. Σ is the projection of the spin angular momentum s of the nucleon along the z-axis, $\Omega = \Lambda \pm \Sigma = \Lambda \pm 1/2$.

cooperatively to the nuclear properties. The kind of collective motions that the deformed nuclei may exhibit include rotations and vibrations.

2.4.1 Rotational motion

A nucleus whose nucleon density distributions are spherically symmetric cannot have rotational excitations. Rotational excitations can only be observed in nuclei with non-spherical or deformed shape. According to the laws of quantum mechanics nuclei cannot rotate around an axis of symmetry since there are no observable changes. Therefore, spherical nuclei cannot rotate because all their axes are axes of symmetry. A deformed axially symmetric nucleus can only rotate around an axis perpendicular to the symmetry axis. Triaxially deformed nucleus can rotate around any of its axes. Figure 2.4 shows the rotation of an axially deformed nucleus around the axis (a) perpendicular to the axis of symmetry (c).

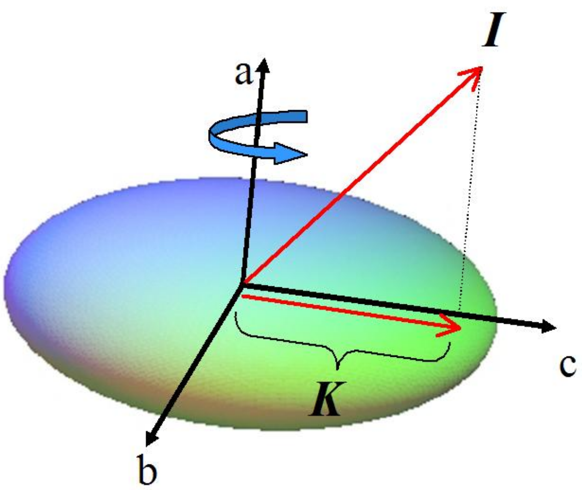

FIGURE 2.4: A deformed nucleus with axial symmetry rotating around the axis (a) that is perpendicular to the nuclear symmetry axis (c). I is the total angular momentum and K is the projection of I onto the symmetry axis (c).

The excited levels of a rotating nucleus have different energies which depend on the number of nucleons in a nucleus. A nucleus with even numbers of both protons and neutrons, generates excited rotational levels (E_{Rot}) with energies of

$$E_{Rot} = \frac{I(I+1)\hbar^2}{2\mathcal{I}}, \tag{2.1}$$

where I is the rotational angular momentum, and $\mathcal{I}$ is the moment of inertia of the nucleus. Only even values of I are allowed for even-even nuclei. The rotational levels corresponding to strong coupling in odd-mass nuclei are defined as,

$$E_{Rot} = \frac{(I(I+1) - K^2)\hbar^2}{2\mathcal{I}}, \tag{2.2}$$

where K is projection of I on the symmetry axis. Here I can take the values K, $K+1$, $K+2$, $K+3$ etc. More details about different rotational coupling are described in sec. 2.5.2

2.4.2 Vibrational motion (nuclear shape oscillation)

A mode of oscillation of the nuclear shape can be described in terms of spherical harmonics $Y_{\lambda\mu}(\theta,\phi)$, as a function of position (θ,ϕ) on the nuclear surface. A distance (R) from the center of the nucleus to all points on its surface gives an indication on whether the surface is spherical or non-spherical. For instance, if the distance from all surface points to the center is the same then a nuclear surface is spherical and R does not depend on (θ,ϕ). The distance R becomes dependent on (θ,ϕ) if the nuclear surface is non-spherical and can be represented in the basis of the spherical harmonics [29, 30]:

$$R(t) = R_{av} + \sum_{\lambda\geq 1}\sum_{\mu=-\mu}^{+\lambda} a_{\lambda\mu}(t)Y_{\lambda\mu}(\theta,\phi), \tag{2.3}$$

where R_{av} is an average radius and $a_{\lambda\mu}(t)$ is a time dependent expansion coefficient. The a_{00} coefficient represents changes in the radius and the $a_{1\mu}$ coefficient represents translation of the nucleus. To keep the volume of a nucleus constant, a_{00} =0 and to work with stationary nuclei, $a_{1\mu}$=0.

The nuclear shape with the lowest λ is quadrupole with $\lambda = 2$, see for example Fig. 2.6. The vibration of the quadrupole shape can be divided into two modes – the γ and β vibrations. A nucleus in a γ vibrational mode (fluctuations in the γ parameter) oscillates around an average triaxial deformation between a prolate and an oblate shape. For small magnitude vibrations around an axially symmetric shape, the γ phonon carries $2\hbar$ of angular momentum that is aligned along the symmetry axis [31]. Thus the projection of the total angular momentum along the symmetry axis is conserved and K=2. The γ vibration is a result of γ softness of the nuclear shape.

The nucleons in a β vibrational mode move coherently, representing oscillations between a less and more deformed shape (fluctuations in the quadrupole parameter), see Fig. 2.5. The β-vibrational phonon carries zero angular momentum, hence the projection of the total angular momentum along the symmetry axis is zero (K=0) [32]. Experimentally, these modes of vibrations are manifested through a series of levels built on the first excited 0_2^+ (K=0) and 2_2^+ (K=2) states.

The $\lambda = 3$ term describes octupole shapes, Fig. 2.6. A nucleus in a octupole vibrational mode is oscillating around a pear shape, as illustrated in Fig. 2.5. The experimentally observed bands associated with this mode of vibration are built on the 3^-, and 1^- states. The $\lambda = 4$ term describes hexadecapole shapes, see Fig. 2.6. The oscillation of the hexadecapole shape is experimentally manifested as bands built on a $K = 4^+$ state, decaying via E4 transitions to the ground-state band.

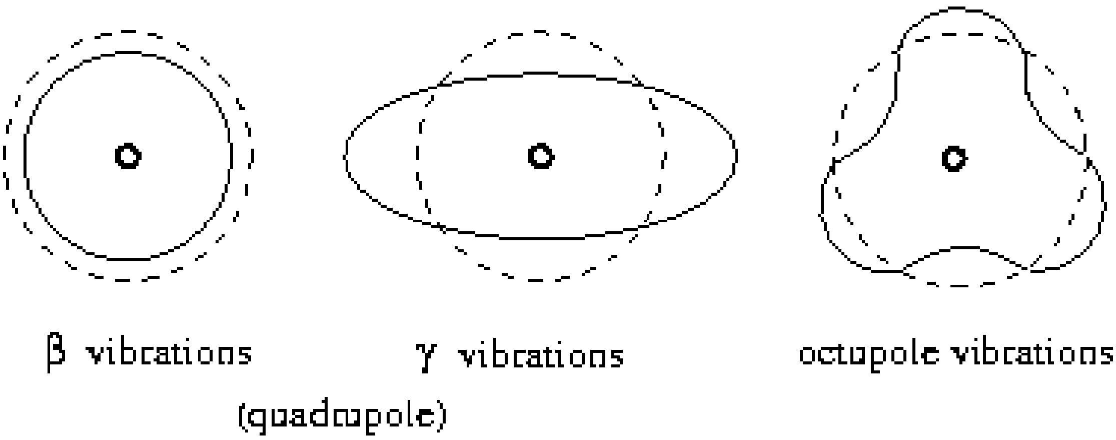

FIGURE 2.5: The quadrupole and octupole modes of vibrations viewed along the symmetry axis.

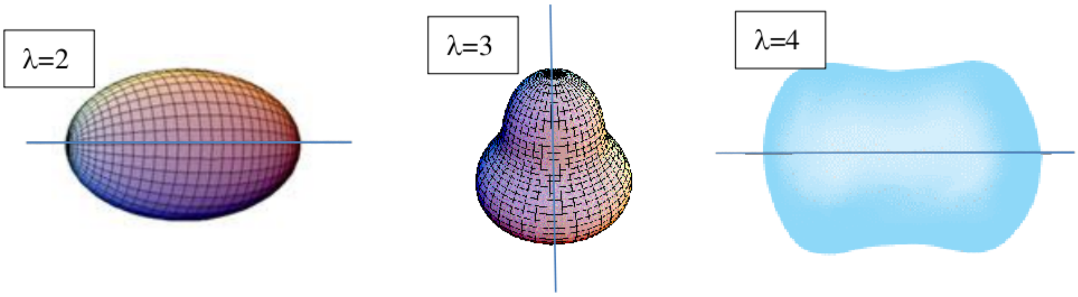

FIGURE 2.6: Examples showing axially symmetric nuclear shapes with quadrupole ($\lambda = 2$), octupole ($\lambda = 3$), and hexadecapole ($\lambda = 4$) deformation.

2.5 Even-even nuclei

All nuclei with even numbers of both protons and neutrons have 0^+ ground state. The first excited state in most nuclei is a 2^+ state. The collective properties of these nuclei vary smoothly and gradually with nucleon number. Figure 2.7 shows some of the important properties of such nuclei that reveal collective behaviour. It can be seen in this figure that the level spacing between the 0^+ and 2^+ states decreases smoothly with the increase in nucleon number. That is, the energy of the 2^+ state decreases as one moves away from the closed-shell region. The ratio ($R_{4^+/2^+}$) of the energy of the 4^+ and 2^+ states is roughly 2 for spherical vibrator nuclei, and roughly 3.3 for deformed nuclei in the mid-shell region. Most spherical vibrator nuclei are located in the $A < 150$ mass region, and they have small electric quadrupole moments. Well deformed nuclei with the ~ 3.3 ratio are mostly found in the $150 < A < 190$ and $A > 230$ mass regions [33]. In these mass regions, the energies of the 2^+ states are exceptionally small and the electric quadrupole moments are quite large.

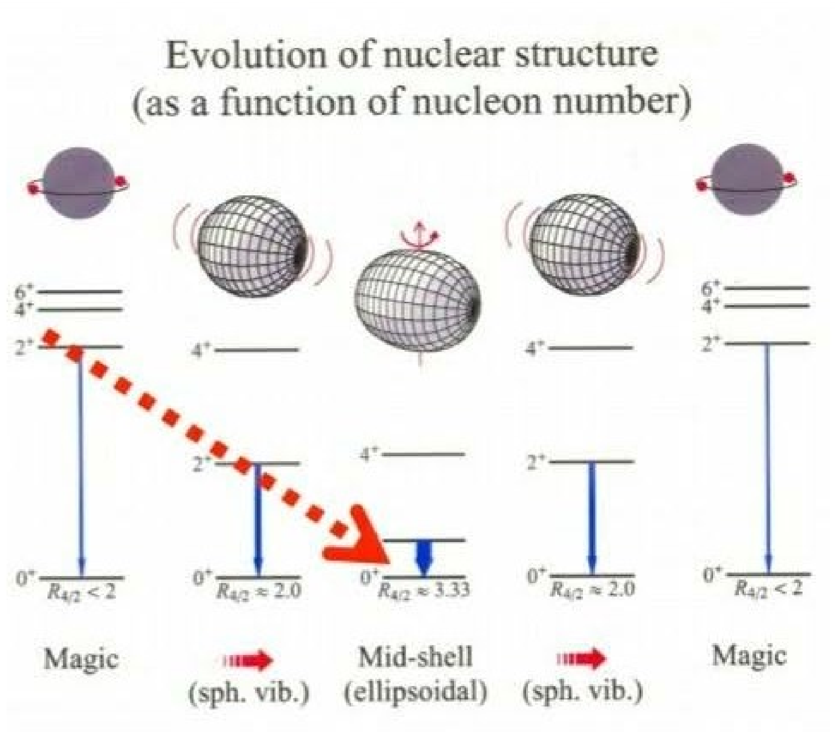

FIGURE 2.7: Evolution of nuclear structure as a function of nucleon number.

2.5.1 Modes of excitations of spherical and deformed nuclei

It is known that the more deformed the nucleus is, the larger its moment of inertia, and therefore the smaller the energies of its states for the same angular momentum. Thus a well deformed nucleus requires a lower excitation energy for the same angular momentum as compared to the excitation energy needed to promote a nucleon in spherical nuclei. The spherical and deformed nuclei have different modes of excitations. The experimentally characteristic features of these two modes of excitations are illustrated in Fig. 2.8. The single particle excitations produce a very irregular structure, while the rotational states follow a very regular pattern.

2.5.2 Particle-core coupling

Many nuclear properties can be understood by studying rotational bands in deformed nuclei formed as a result of particle excitations or coupling of an odd particle to the deformed core. The angular momentum of the odd-particle can couple strongly or weakly to the rotational axis. The experimentally observed properties of these two couplings are illustrated in Fig. 2.9.

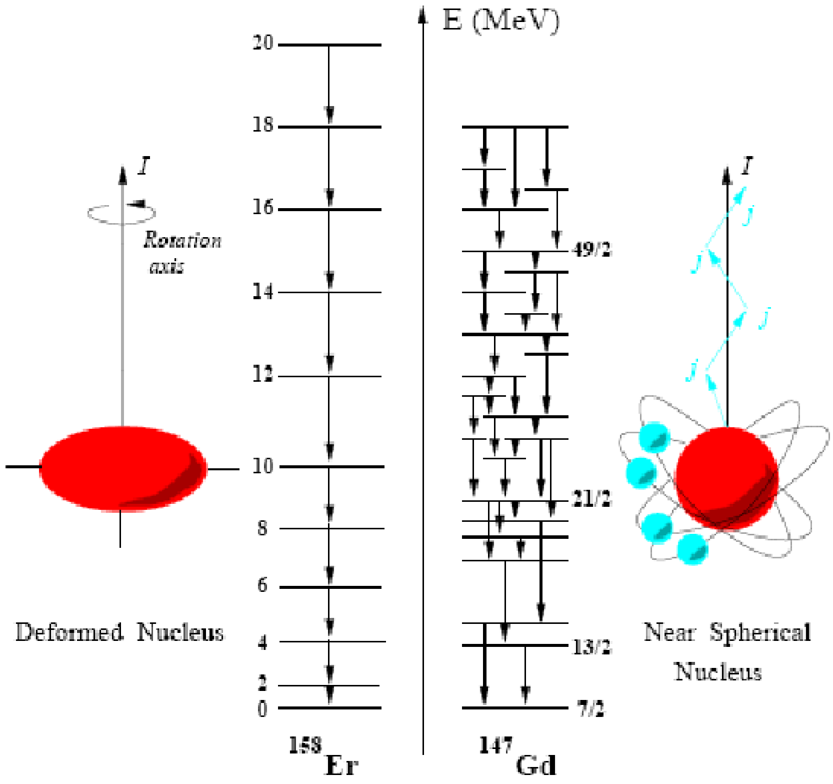

FIGURE 2.8: Modes of excitations of spherical and deformed even-even nuclei.

In the strong coupling limit, the aligned angular momentum of the odd-particle is small and the total projection $K = \Omega$ is large. The band head for such coupling has spin K and the bands show both odd- and even-spin levels linked by $\Delta I = 1$ decays, see Fig. 2.9 (b). When the Coriolis force becomes large, the strong coupling breaks down. In the weak coupling limit, high-j orbitals with low-Ω projections are involved. The rotation of the deformed core is coupled to the angular momentum of the odd-particle, and the bands built on such systems have energy spacings that are similar to those of the ground-state bands in even-even neighbouring nuclei, see Fig. 2.9 (a).

2.6 Rotational bands

2.6.1 Alignments and band crossings

Generally, two nuclear states with the same angular momentum and parity which lie close in energy can mix and interchange nuclear properties. This is normally caused by pair breaking with consequent alignment of the angular momenta of the two nucleons with the

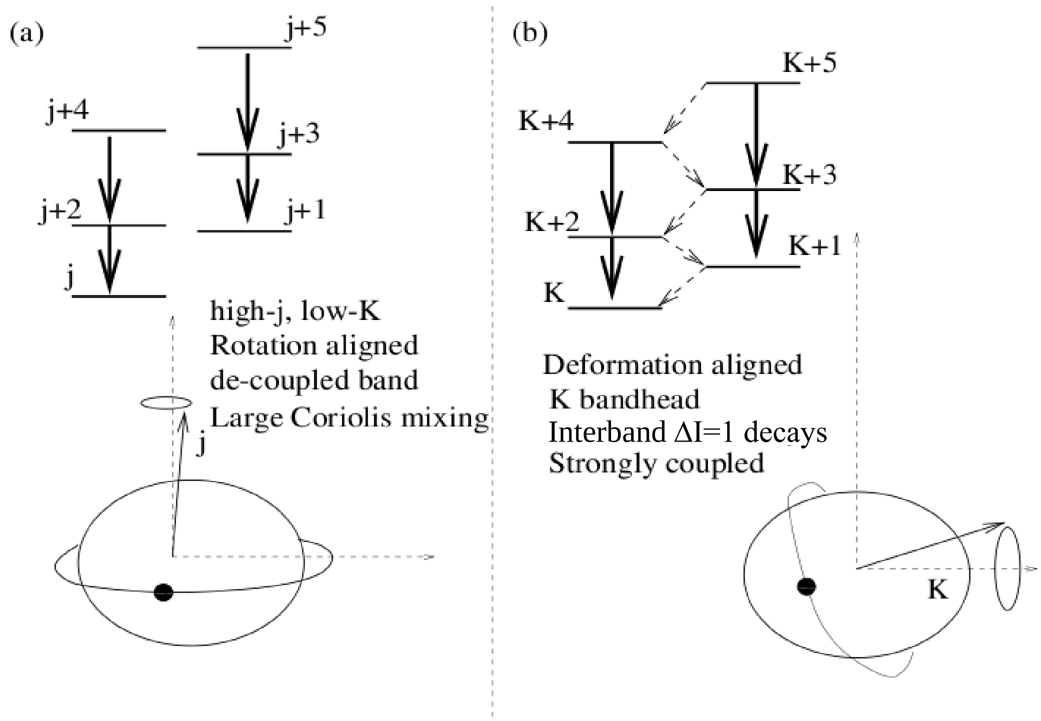

FIGURE 2.9: Decay schemes and descriptions of weak (b) and strong (a) coupling of an odd-particle to a deformed nuclear core.

rotational axis. Band mixing has been experimentally observed in a number of deformed nuclei. The plot of aligned angular momentum, i_x, as a function of the rotational frequency multiplied by $\hbar$ has been one of the methods that nuclear physicists use to identify cases where pairs break and the associated single particle angular momenta align along the rotational axis. The aligned angular momentum [34] is defined as

$$i_x = I_x - I_{xg}, \tag{2.4}$$

where I_x is the angular momentum along the rotation axis and I_{xg} is given by,

$$I_{xg} = (J_0 + J_1\omega^2)\omega. \tag{2.5}$$

In this equation, J_0 and J_1 are Harris parameters [35] and ω is the rotational frequency.

The experimental data can be compared with the cranked-shell model calculations by transforming the measured level energies and spins to the energies (e') in the rotating frame. The calculated quasi-neutron energies in the rotating frame are related to the aligned angular momentum i_x. That is, the single-particle alignment is the negative of the slope of the corresponding Routhian, $i_x = -de'/d\omega$. Band crossing can also easily be identified when one plots the experimental energies in a rotating frame (Routhian) as a function of $\hbar\omega$.

2.6.2 Transition rates and probabilities

One of the techniques used in nuclear structure physics to understand the properties of the observed excited bands is the measurement of B(E2) reduced transition probabilities. These measurements are instrumental in determining whether a nuclear state is collective or non-collective. The branching ratios for electric quadrupole and magnetic dipole transitions, depopulating the same state can be calculated using,

$$\frac{B(M1 : I- > I-1)}{B(E2 : I- > I-2)} = 0.697 \frac{[E_\gamma(I- > I-2)]^5}{[E_\gamma(I- > I-1)]^3} \frac{1}{(\delta^2+1)} \frac{1}{\lambda}, [\frac{\mu_N^2}{e^2 b^2}] \quad (2.6)$$

where E_γ is the γ-ray energy, δ is the mixing ratio parameter, which gives information about the $E2/M1$ admixture in the $I \rightarrow I-1$ transition and $\frac{1}{\lambda}$ is a ratio of the measured γ-ray intensities for the $I \rightarrow I-1$ and $I \rightarrow I-2$ transitions.

Chapter 3

Experimental methods

The experiment was carried out at iThemba LABS. The excited states of ^{186}Os were populated by a fusion evaporation reaction. The accelerated ions of the beam were delivered by the Separated-Sector Cyclotron (SSC) [36, 37]. The γ radiation emitted from the reaction products were detected by the AFRODITE γ-ray spectrometer [38]. Data sorting and analysis were carried out using Midas MTsort [39] and RadWare [40, 41] software packages. The techniques used to collect and analyse the data are discussed in greater details in the following subsections.

3.1 Acceleration of charged particle beams in a cyclotron

Atoms need to undergo ionization, a removal of one or more electrons from atoms, before they can be accelerated. During the fusion-evaporation experiment, beams of accelerated charged particles are used to bombard the target nuclei to form a highly excited compound nucleus that decays by emitting particles and radiation. At iThemba LABS, the solid-pole injector cyclotron (SPC) pre-accelerates beams of ions before an injection into a separated-sector cyclotron, shown in Fig. 3.1 [42], for final acceleration. Due to the presence of electric and magnetic fields in a cyclotron, the charged particles are successively accelerated resulting in energy gain, and experience a force perpendicular to its direction of motion which causes the charged particles to move in a circular path. The particles are accelerated until they reach a desired energy where they are deflected out of the cyclotron, and transported into the AFRODITE vault where they impinge on a target which is placed at the center of the AFRODITE array.

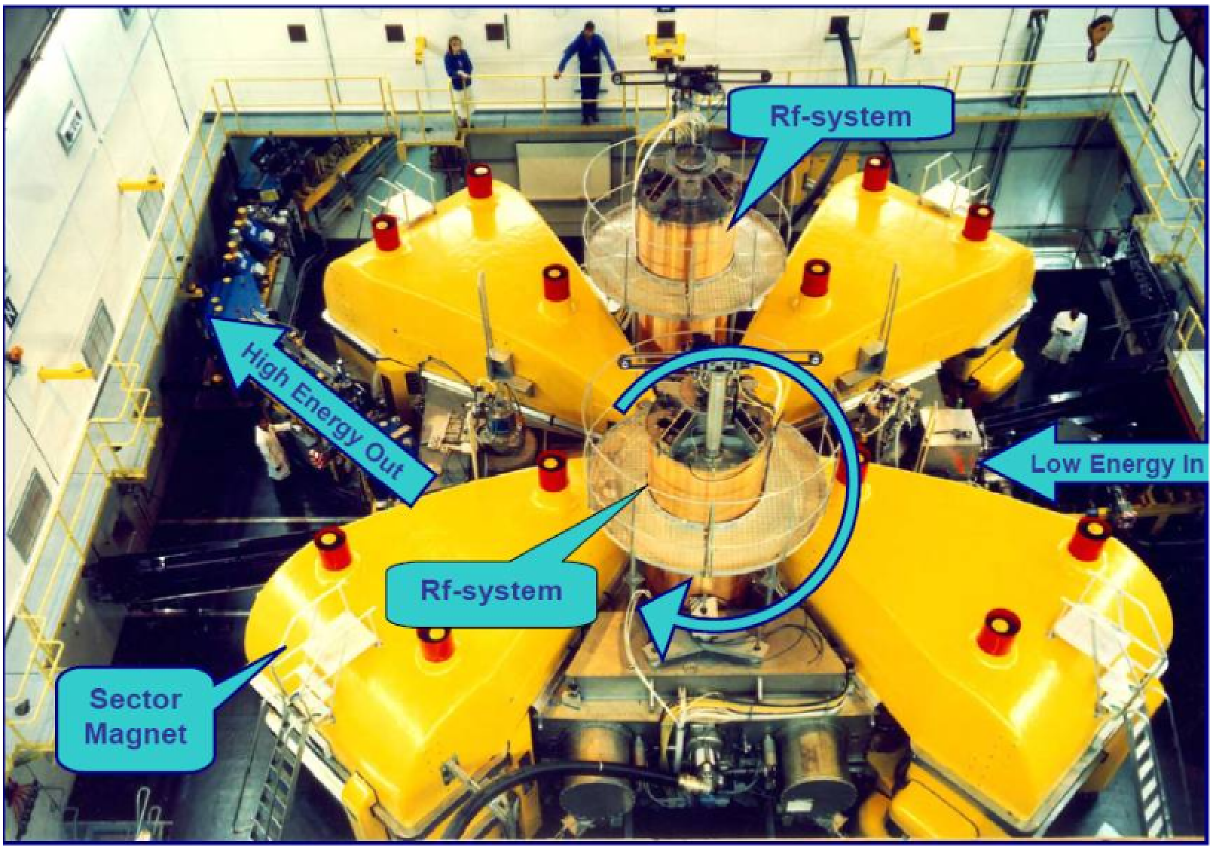

FIGURE 3.1: The iThemba LABS Separated Sector Cyclotron used to accelerate beam of projectiles towards the target nuclei during the experiment.

3.2 PACE4 calculations

Beams of particles with high energies are capable of overcoming the repulsive electric force (Coulomb barrier) between their own positively charged protons and those of the target nuclei and cause a nuclear reaction. In order for a fusion reaction to occur the energy of the projectile nucleus has to be high enough to overcome the Coulomb barrier. Before the experiment is carried out, the Coulomb barrier is calculated. Then a simulation to estimate the optimal beam energy is performed. In the present study, the Projected Angular Momentum Coupled Evaporation (PACE4) code [43] was used to estimate optimal beam energies for the ^{186}W(^{4}He, 4n)^{186}Os reaction. The Coulomb barrier [44] was calculated using

$$V_{cb} = \frac{1.44 Z_1 Z_2}{1.16(A_1^{1/3} + A_2^{1/3} + 2)}, \tag{3.1}$$

where $Z_1(A_1)$ and $Z_2(A_2)$ are the atomic (mass) numbers of the beam and target nuclei, respectively. The calculated Coulomb barrier for the ^{186}W(^{4}He, 4n)^{186}Os reaction was

$V_{cb} = 19.8$ MeV.

The PACE4 calculations performed before the $^{186}W(^{4}He, 4n)^{186}Os$ experiment are presented in Fig. 3.2. The figure shows yield percentages of the isotopes of Os that were populated during the experiment, plotted as a function of beam energy. It can be seen from this figure that the yield percentage at 48 MeV is about 90% for the nucleus of interest (^{186}Os), and less than 10% for other isotopes. It should be noted that in Fig. 3.2 the beam energy at 48 MeV is slightly above the maximum yield percentage of ^{186}Os. The reason for this is that the beam adjustment was made in order to take into account the energy loss in the target.

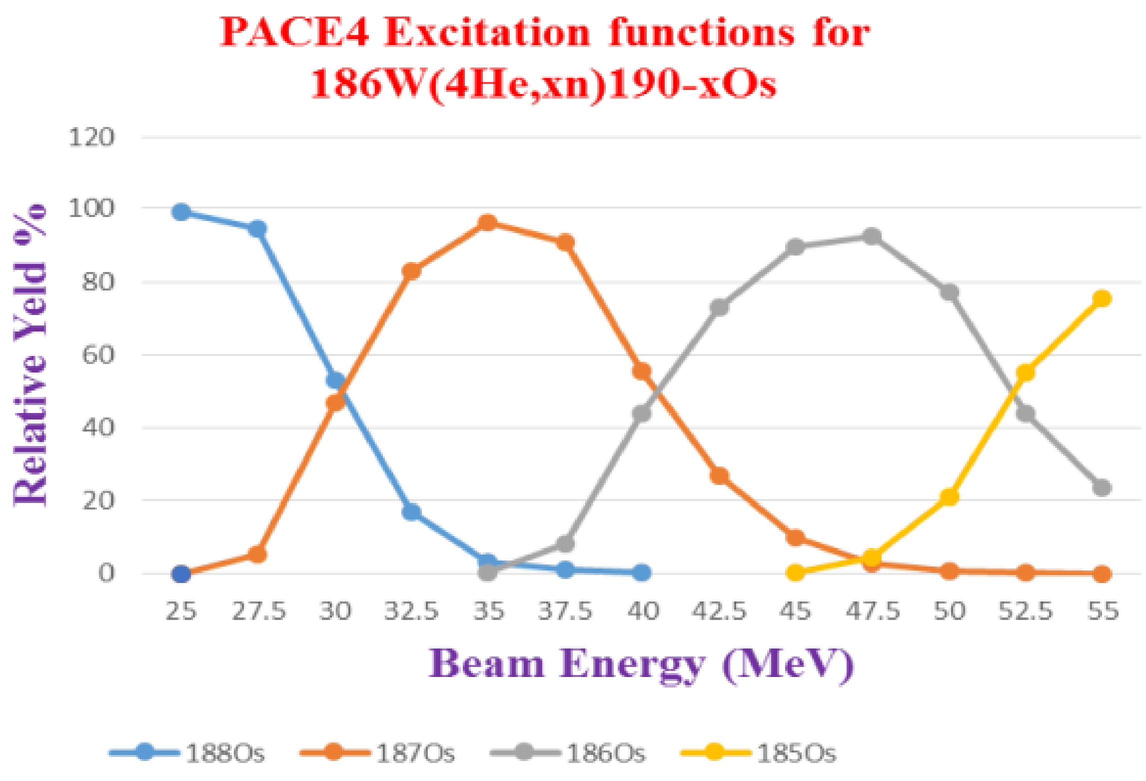

FIGURE 3.2: PACE4 calculations performed for the isotopes of Os.

3.3 Reaction used

As mentioned earlier, the reaction used to populate the excited states of the nucleus of interest is the fusion reaction. This reaction is one of the reactions that impart large angular momentum into the nucleus [45]. It is a widely used reaction to study high-spin states in nuclear structure physics. In the present work the ^{186}W(^{4}He, 4n)^{186}Os reactions was used to investigate the excited states of ^{186}Os.

In a fusion-evaporation-reaction experiment, a projectile nucleus is accelerated by a cyclotron and used to bombard a target nucleus, placed at the centre of the γ-ray spectrometer inside a target chamber. A projectile nucleus transfers all of its energy and momentum into a target nucleus, resulting in the formation of a compound nucleus which is highly excited and unstable, rotating at a very high frequency. A compound nucleus de-excites by emitting particles such as α, protons and neutrons, and then proceeds by emitting electromagnetic radiation such as γ-rays and X-rays. The emission of these particles and radiation take away a large amount of excitation energy and some angular momentum from the nucleus, which causes the nucleus to decay to lower excited states and eventually to its ground state. A schematic diagram displaying how the fusion evaporation reaction proceeds is shown in Fig. 3.3 [46]. Figure 3.4 [44] illustrates typical γ-ray de-excitation paths following the production of a compound nucleus.

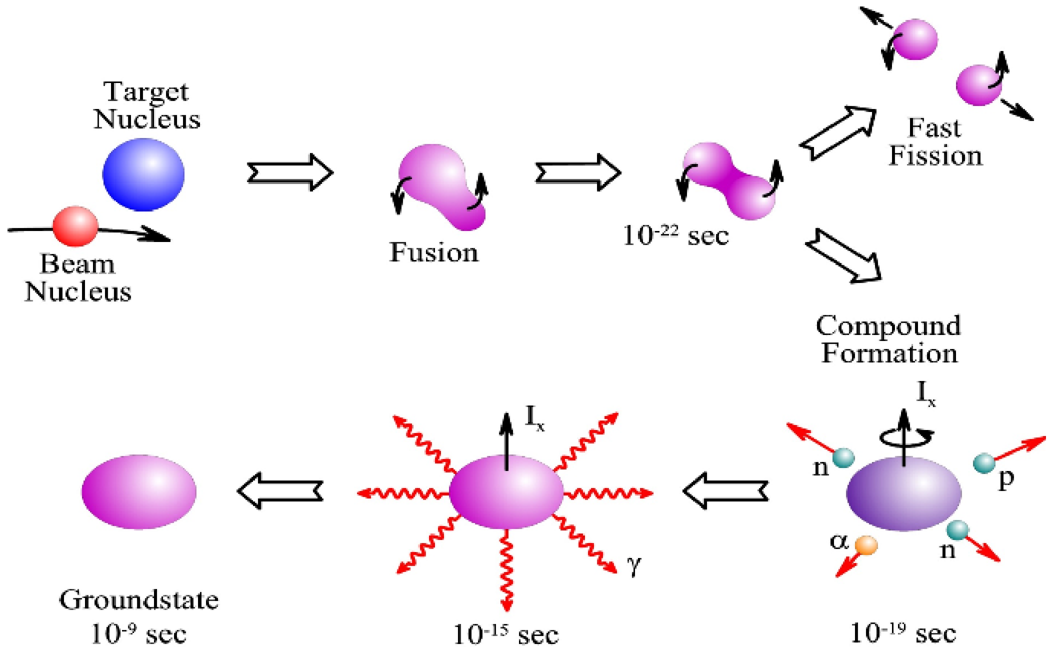

FIGURE 3.3: Schematic diagram showing how fusion evaporation proceeds.

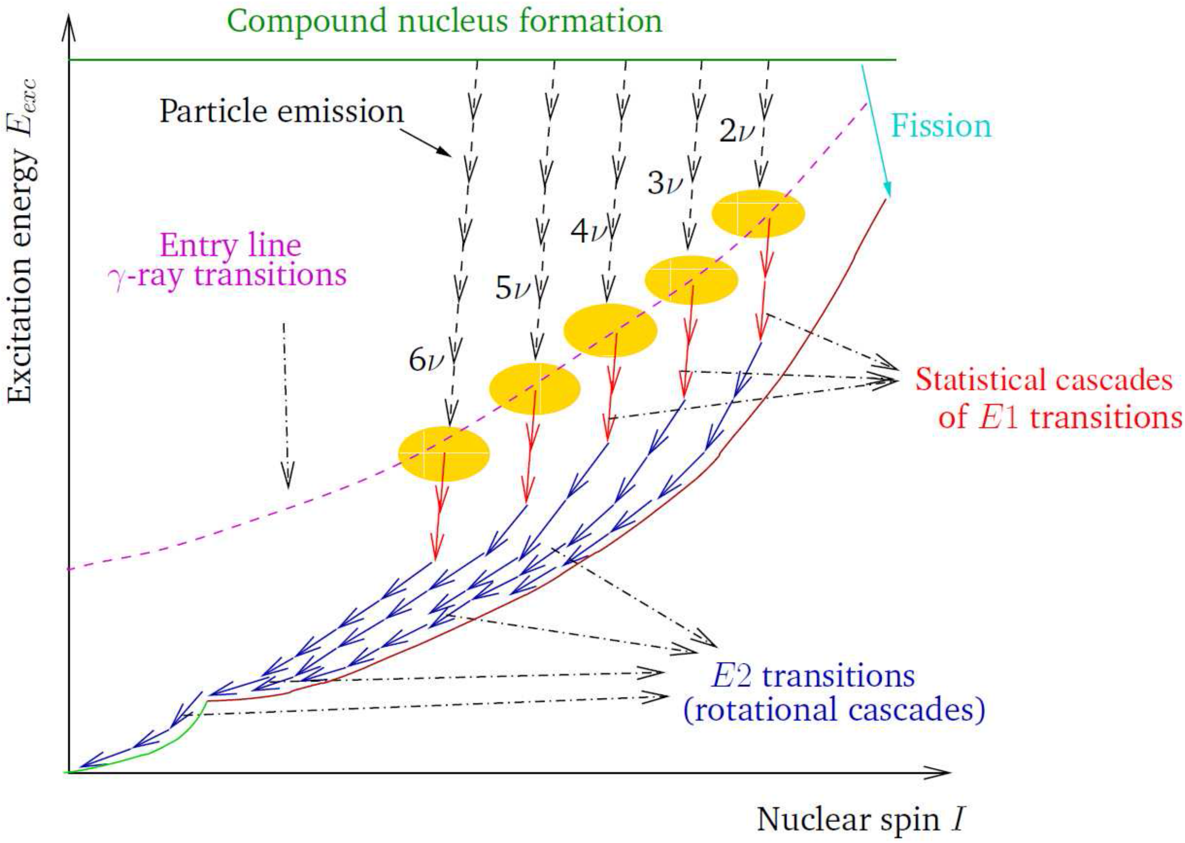

Figure 3.4: A diagram showing typical γ-ray de-excitation paths following the production of a compound nucleus in a fusion evaporation reaction.

3.4 Interaction of matter with gamma radiation

Unstable excited nuclei release energy in a form of particle emission or emission of electromagnetic radiation in order to regain stability. There are several processes that take place when the released nuclear energy comes into contact with matter. Here we discuss three major processes that occur when γ radiation interacts with matter. Such processes are the photoelectric effect, Compton effect, and pair production, see Fig. 3.5 [47]. In the photoelectric effect, an electron is ejected from an atom when a photon with sufficient energy shines on the matter. This phenomenon is dominant at low γ-photon energies. In the Compton effect, the incident γ photon gives some of its energy to an electron causing both the photon and the electron to scatter at different angles. This effect is usually observed at energies between those of the photoelectric effect and those of the pair production. The Compton effect leads to a large background in the γ-ray spectrum, which significantly affects the signal-to-noise performance of the detectors. The last phenomenon is pair production which only occurs at energies greater than 1022 keV. When a photon with sufficient energy comes in the vicinity of an atom, an electron-positron pair may be created. When a pair of electron and positron come into contact they annihilate, and result in the creation of a γ radiation - transforming matter into energy. The annihilation produces two γ photons with energy of 511 keV each that travel in opposite directions.

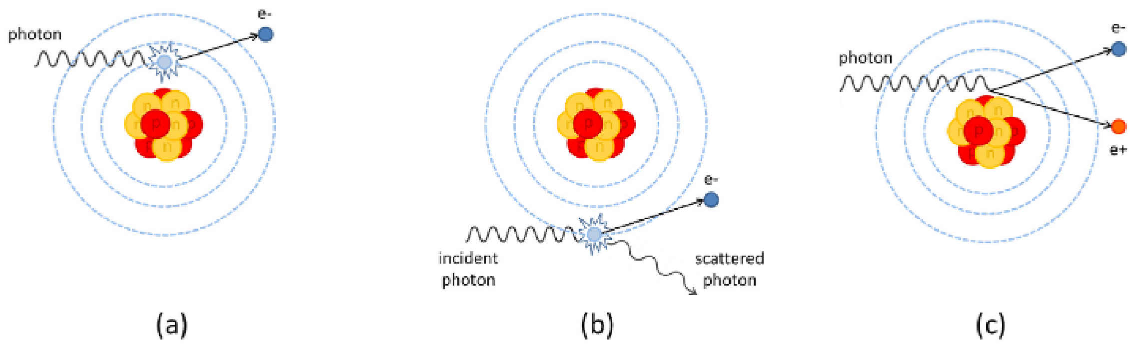

FIGURE 3.5: Three processes that occur when γ radiation interact with matter (a) photoelectric effect, (b) Compton effect, and (a) pair production. The e^- and e^+ symbols represent electron and positron, respectively.

3.4.1 Detection of gamma radiation

A number of different detectors are employed for detection of nuclear radiation. Such detectors are developed to detect different kinds of radiation. In our experiment, the γ radiation emitted from the reaction products were detected by the semi-conductor detectors of the AFRODITE array [38], which were placed around the target chamber as shown in Fig. 3.6. The semi-conductor detectors used in the experiment consisted of Compton-suppressed high-purity germanium (HPGe) clover detectors and low energy photons spectrometers commonly known as LEPS detectors. Each clover detector consists of four HPGe crystals arranged in a clover-leaf configuration. The four crystals of a clover detector mounted in the Bismuth Germanate Oxide (BGO) shield is illustrated in Fig. 3.7 [48].

During the experiment the ^{4}He beam was used to bombard a stack of four ^{186}W targets with a thickness of 100 $\mu g/\mathrm{cm}^2$ each, making a total thickness of 400 $\mu g/\mathrm{cm}^2$. A total of 11 clover detectors were used to detect the γ rays emitted by the reaction products, seven clovers were positioned at an angle of 90° and four at 135° with respect to the beam direction.

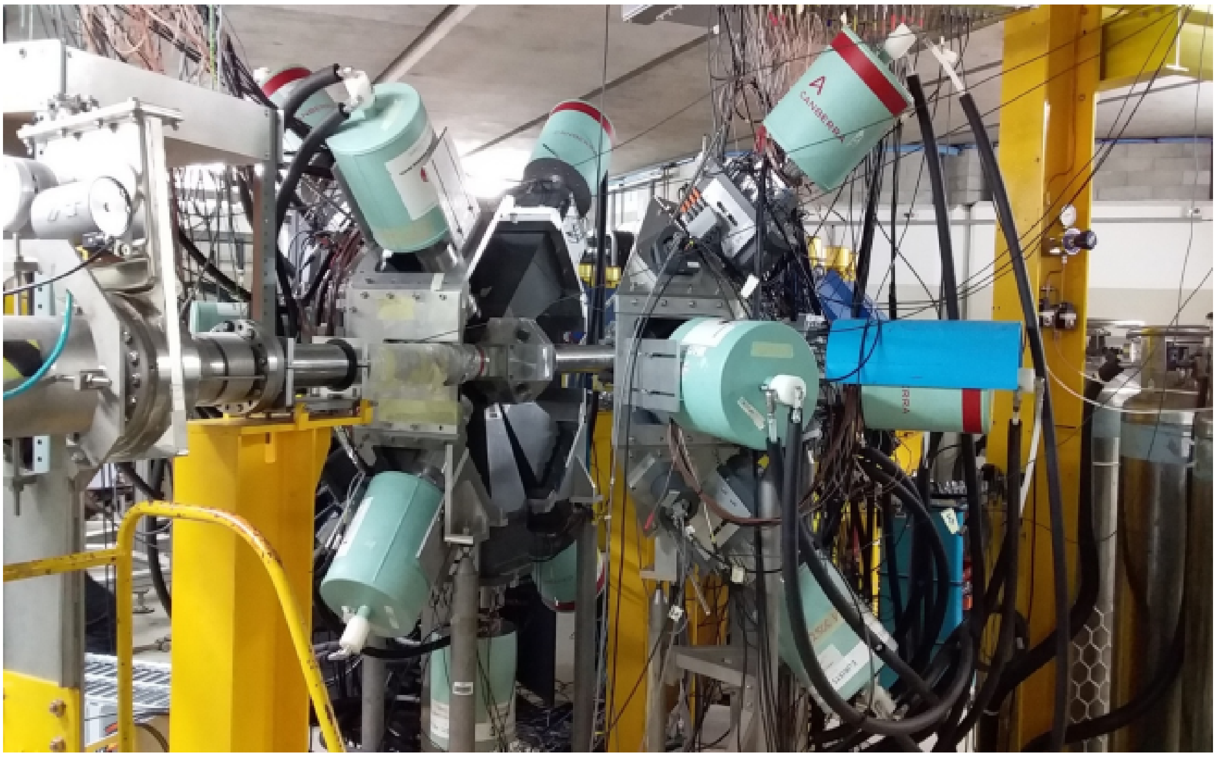

FIGURE 3.6: The iThemba LABS AFRODITE γ-ray spectrometer showing how the clover detectors were arranged in the experiment.

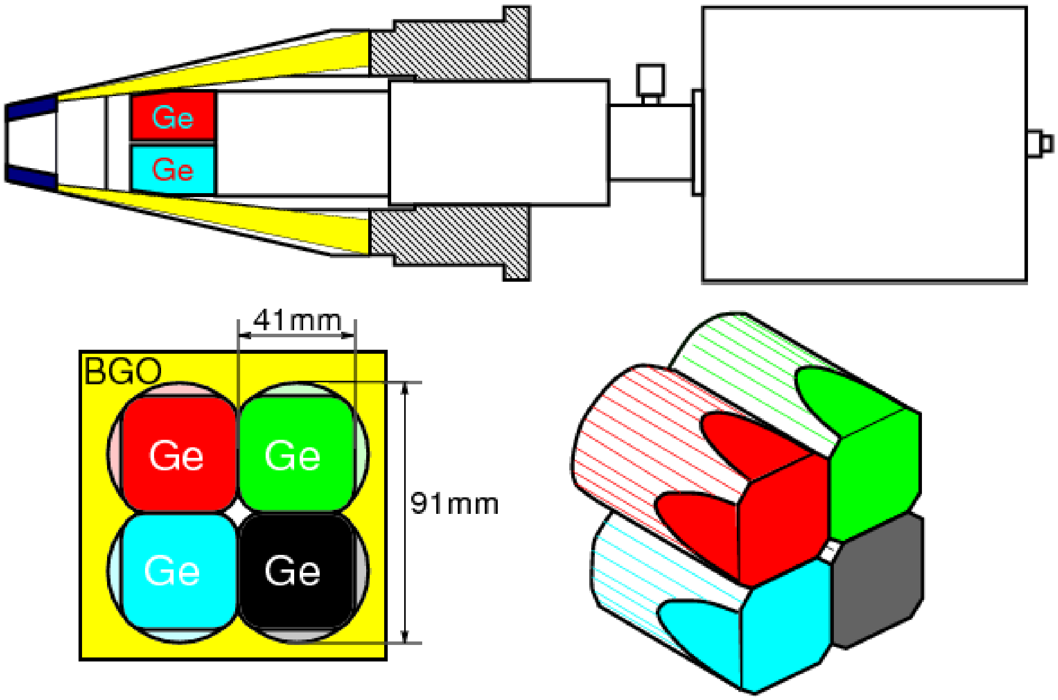

FIGURE 3.7: A diagram displaying the four-segmented clover detector mounted in the BGO shield.

3.4.2 Add-back and suppression of the Compton background

The four crystals of a clover detector are packed in a cryostat very close to each other. Thus, there is high probability that the γ ray may hit a crystal and Compton scatter to one of its adjacent crystals, depositing its energy in both crystals. Using a technique called add-back, an energy deposited in the first crystal can be added to the energy deposited in the second crystal to recover the full energy of the γ ray. In some instances the γ ray may deposit part of its energy in the clover, and then escape outside of the detector. Thus, only part of the energy is detected. It therefore creates a count in the low-energy region of the spectrum instead of in the photopeak. This causes a large background in the spectrum, which makes it difficult to identify weak peaks. To avoid this, the clover detectors are normally used together with the Bismuth Germanate Oxide (BGO) detectors such that the γ-ray energy that is detected in both detectors within a defined short period of time is not considered as useful data. The inclusion of the BGO detectors significantly suppresses the Compton background and consequently improves the resolving power of the clover detectors. Figure 3.8 [44] shows how the inclusion of the BGO detectors reduces the background in the germanium detector spectra .

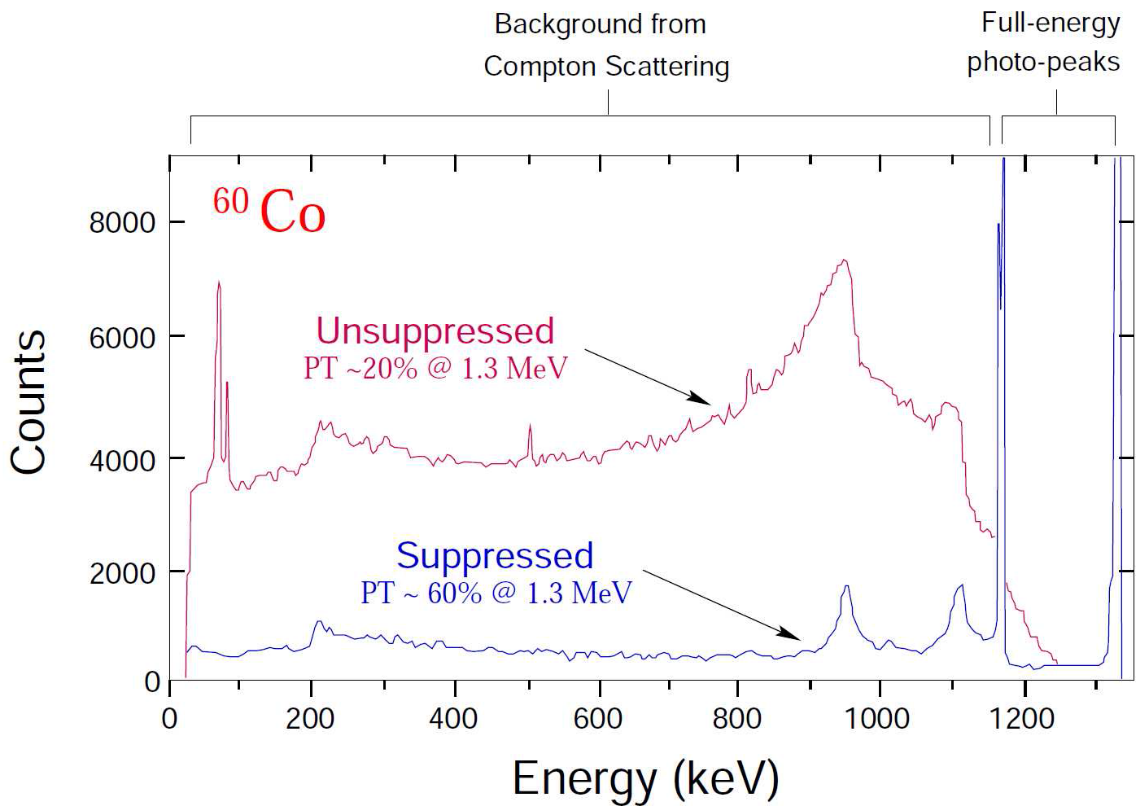

Figure 3.8: Spectra from a ^{60}Co source showing how the inclusion of BGO detectors reduces Compton background.

3.5 Data analysis method

The data analysis in this work is carried out using the Midas MTsort [39] and RadWare [40, 41] software packages. The data from the ^{152}Eu source collected before and after the experiment is respectively used to determine the energy and efficiency calibrations of the detectors. During the ^{152}Eu-data collection, the ^{152}Eu source is placed at the center of the AFRODITE array such that all the detectors can detect the emitted γ rays. The analysis of the data is carried out using gf3 program. During analysis of the ^{152}Eu source spectrum, the gf3.sto file containing the stored centroids and areas of the fitted peaks is created and used as input to generate a file (.sin) that is used by ENCAL and EFFIT programs for energy and efficiency calibrations, respectively. The (.sin) file is generated by running the SOURCE program. It takes the gf3.sto and ^{152}Eu.sou files as input. The ^{152}Eu.sou file contains the energies and relative intensities of the source γ rays.

3.5.1 Energy calibration

The Radware ENCAL program does a polynomial fit to deduce the energy calibration, taking input data from the (.sin) file which is generated by running a SOURCE program. The order of the polynomial may be chosen from one to five. In the present study, an order of one was used. Thus, the program fits an energy calibration to each detector in the form

$$E = a_0 + a_1 x, \tag{3.2}$$

where x is a channel number, a_0 is the intercept on the energy axis and gives information about the amount of offset present in the data channel and a_1 gives information about the rate of change of energy with the change in channel number called gain. The channels are mapped to calibration of $E = 0.5x'$, x' in this equation represents new channels as shown in Fig. 3.9. The ENCAL program stores the parameters in a (.aca) file, which is used as input file for the ESCL8TOR program. The ESCL8TOR is a RadWare program that is used to construct a decay scheme.

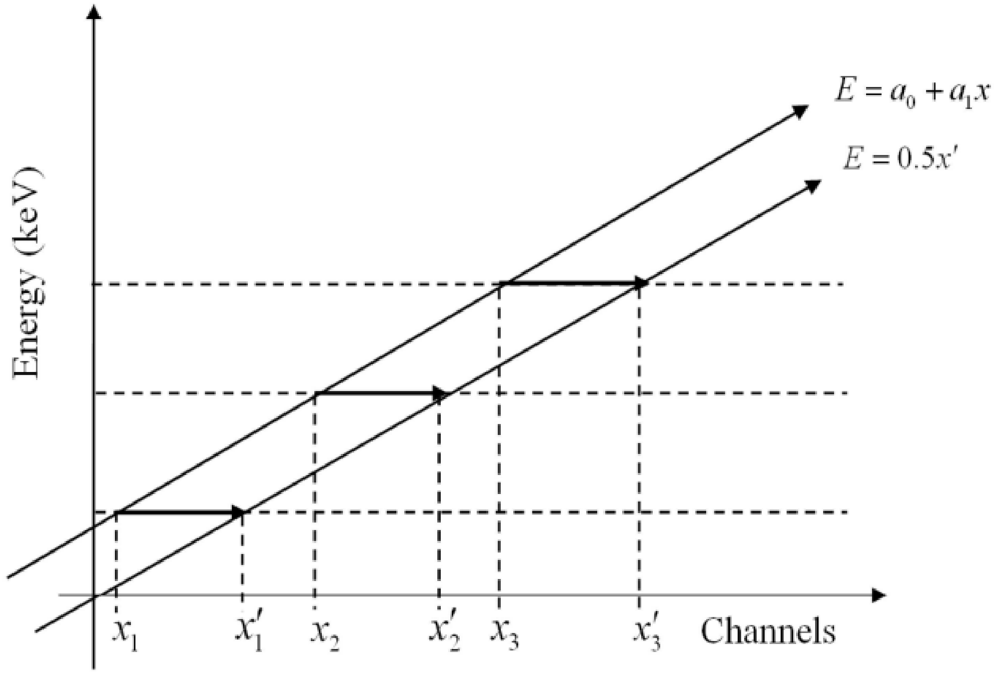

FIGURE 3.9: A diagram showing how the energy calibration is performed.

3.5.2 Efficiency calibration

The EFFIT program is used to fit the germanium detector efficiency curves. The program fits the efficiency calibration to each detector in the form

$$eff = e^{[(A+Bx+Cx^2)^{(-G)}+(D+Ey+Fy^2)^{(-G)}]^{(1/G)}}, \tag{3.3}$$

where $x = \ln(EG/E1)$, and $y = \ln(EG/E2)$. The fitted parameters A, B, and C: $\ln(Eff) = A + B\ln(EG/E1) + C\log(EG/E1)^2$ describe the efficiency at low energies, and the parameters D, E, and F: $\ln(Eff) = D+E\ln(EG/E2)+F\ln(EG/E2)^2$ describe the efficiency at high energies. In these equations, EG represents the γ-ray energy in keV, $E1$ and $E2$ are constants and have the values 100 keV and 1000 keV, respectively. The parameter G describes the interaction between the two regions. This parameter determines the efficiency in the turnover region; the larger G is, the sharper the turnover. The efficiency curve obtained by running the EFFIT program is shown in Fig. 3.10. One can see from this figure that the efficiency of the clover detectors is high at low energies, and decreases smoothly as the energy increases.

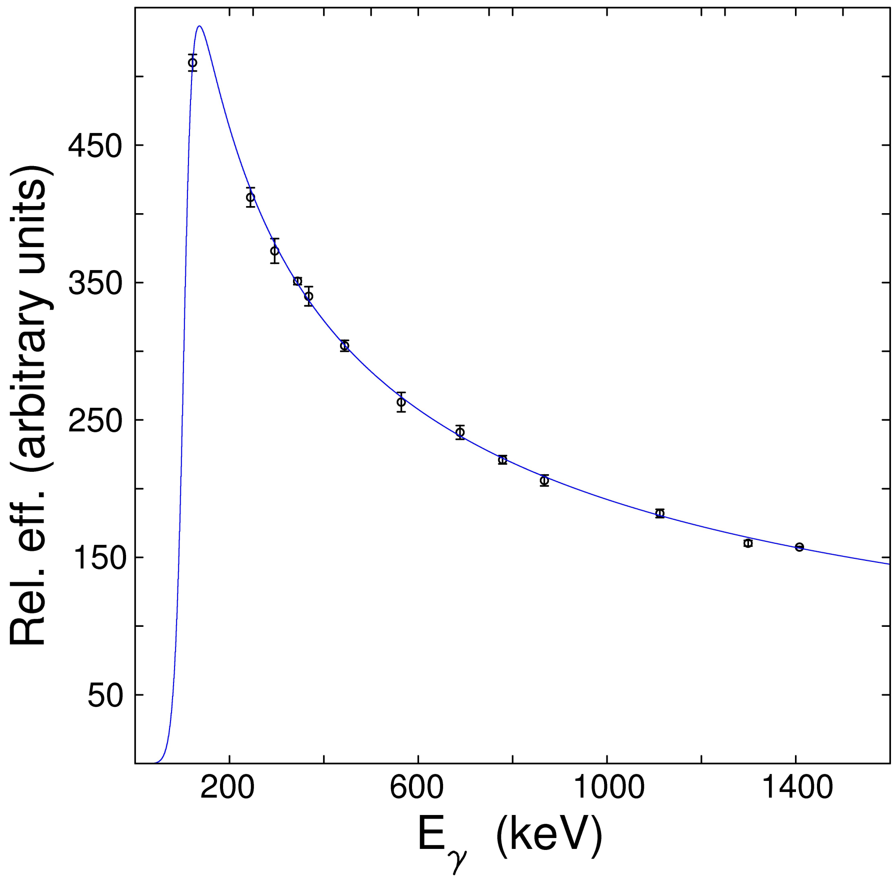

FIGURE 3.10: The efficiency curve of the clover detectors.

3.5.3 Gain drift correction

During the experiment, the temperature variation in the germanium clover detectors of the AFRODITE spectrometer may lead to gain drift [46]. This drift causes the shifts in the values of the gain and offset parameters, producing drifts in the measured spectrum. Thus, it is essential to correct the gain drifts before the analysis can be carried out. To correct the gain drift, we adjust the energy of the spectrum by applying a linear transformation to the position of each peak centroid. The transformation applied is:

$$E_{new} = AE_{old} + B, \tag{3.4}$$

where E_{new} and E_{old} are the new and old γ-ray energies, respectively, $A = (PH - PL)/(CH - CL)$ and $B = [PL(CH - PH) - PH(CL - PL)]/(CH - CL)$. In these equations, PL and PH represent reference peaks at low and high energy region of a spectrum, respectively, and CL and CP are the extracted centroids of the peaks, at low and high energies, from the spectra of each crystal. The gain and offset of the spectrum will be adjusted so that if there had been peaks with the centroids CL and CP, those peaks will now be shifted to new positions PL and PH, respectively. It should be noted from the above equations that if $PH = CH$ and $PL = CL$, A and B in Eq.3.4 become 1 and 0, respectively, and therefore no adjustment will be made to the spectrum.

3.5.4 γ-γ matrices

After gain drift correction is completed, the data is then sorted into E_γ-E_γ matrices using MTsort program [39]. In order for the matrices to be able to be analysed with Radware software [40, 41], they are converted into a (.m4b) format using the eg2rad program. A E_γ-E_γ matrix is a two dimensional energy histogram with the energy of one γ ray on one axis and the energy of the coincident γ ray on the other axis. Events of coincident γ rays are recorded if detection of two or more γ rays occurs within a specified short period of time which is called coincidence window. The γ-ray energies detected within this window belong to the same decay path. The E_γ-E_γ matrices are used to construct the level scheme. In the present work a coincidence window of 200 ns is used.

3.5.5 Nuclear state transition intensities

The intensity of a γ ray decaying from one state to another can be measured. It depends on the area under the γ-ray peak (A) and the efficiency of the detector (ϵ). Mathematically it is given by,

$$I_\gamma = \frac{A}{\epsilon}. \tag{3.5}$$

The total decay intensity is calculated using the expression,

$$I_{Tot} = I_\gamma(1+\alpha), \tag{3.6}$$

where α is the internal conversion coefficient, which is a measure of the importance of the internal conversion compared to the γ-ray emission. It is calculated using the expression,

$$\alpha = \frac{\lambda_e}{\lambda_\gamma}, \tag{3.7}$$

where λ_e and λ_γ are respectively the probabilities of the internal conversion and the γ-ray emission.

3.6 Selection rules

As discussed earlier, the emission of γ radiation de-excites a nucleus into a lower energy state. Such emission occurs when there are changes in the electric and magnetic fields of the nucleus, caused by oscillating charges or currents. The types of γ radiation a nucleus emits depend on the distribution of charges. Charge distributions can be classified as dipole, quadrupole, octupole, etc. A nucleus emits radiation that is associated with multipole moments. Radiation carries angular momentum which can be determined by selection rule. The selection rules, for a γ transition between states of initial spin I_i^π and final spin I_f^π, are that the decay can proceed by a photon of multipole order L where,

$$|I_i - I_f| \leq L \leq I_i + I_f. \tag{3.8}$$

The general rule is that the lowest multipole order L dominates the decays. The electric and magnetic nature of the γ transitions is decided by the parity conservation law, which is given by,

$$\pi_i = \pi_f \pi_L. \tag{3.9}$$

The parity of an electric transition of multipole order L is given by $(-1)^L$, implying that the parity is positive for even multipole order L and negative for odd multipole order L. On the other hand, the parity of a magnetic transition of multipole order L is given by $(-1)^{L+1}$. Unlike the electric transition, the parity for a magnetic transition is positive for odd values of L and negative for even values of L. Figure 3.11 shows how the γ-ray selection rule works.

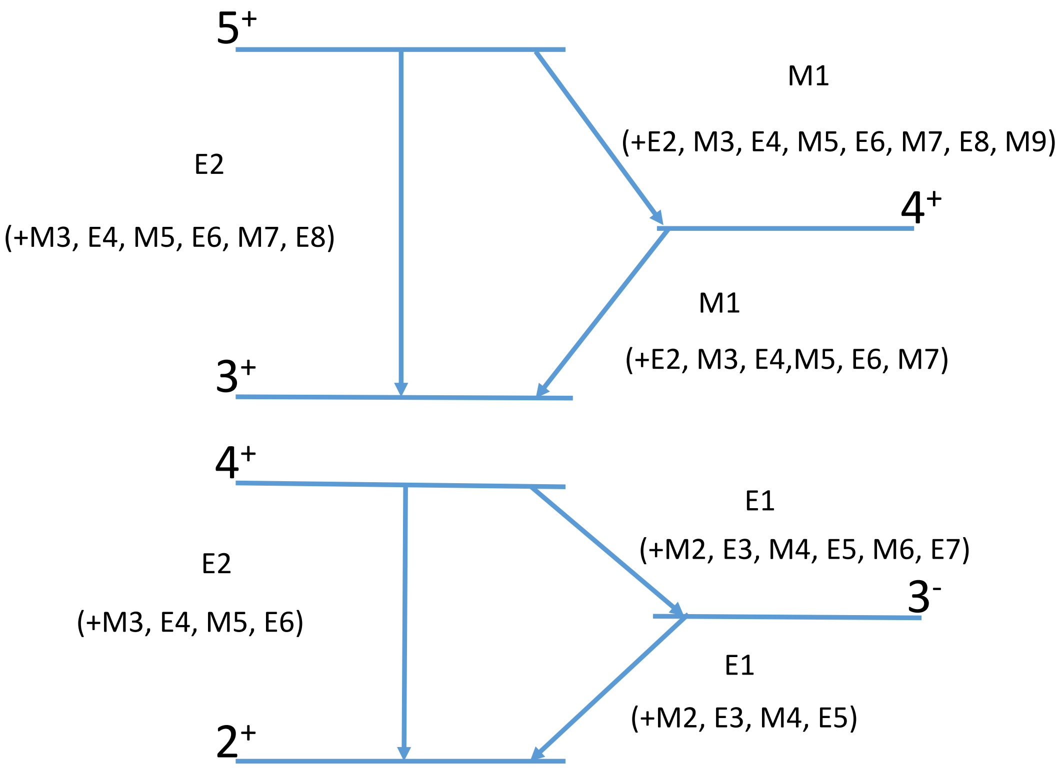

FIGURE 3.11: Schematic level scheme showing the allowed multipolarities for the decay transitions. The allowed higher-order multipolarities are shown in brackets. Usually they are negligible except in some cases where mixed M1+E2 transitions are observed and where the E2 component can be significant.

3.7 Angular distribution ratios and linear polarization measurements

An excited nucleus can decay into its lower state by releasing energy in a form of electromagnetic γ radiation. Such excited nucleus decays by a transition of multipole order L, which could be either electric or magnetic. The γ-ray transitions can be classified by their multipolarities, electric dipole ($E1$), magnetic dipole ($M1$), electric quadrupole ($E2$), etc. These transitions could be stretched or unstretched. The γ ray for a stretched transition carries away angular momentum that is exactly equal to the difference between the spins of the initial and final nuclear levels (L=$|I_i - I_f|$). Such transitions do not change nuclear spin orientation, they only reduce the angular momentum. In contrast, the γ ray for an unstretched transition carries away $L > |I_i - I_f|$ angular momentum, and slightly changes the spin orientation of a nucleus. Experimentally, the multipolarities of the γ-ray transitions can be determined by measuring angular distribution ratios and linear polarization asymmetries. These two techniques of determining spins and parities of excited nuclear levels are described below.

3.7.1 Angular distribution ratios

In order to determine whether the γ-ray transition is a stretched dipole or quadrupole, one needs to measure the angular distribution ratios (R_{AD}). For R_{AD} measurements, the coincidence data were sorted into two asymmetric matrices whose one axis corresponded to γ-ray energies deposited in the clover detectors positioned at 90^0 and 135^0, while the γ-ray energies deposited in all detectors were placed on the second axis. The R_{AD} were measured using

$$R_{AD} = \frac{I_{\gamma_1}^{135^\circ}(Gated_{\gamma_2}^{All})}{I_{\gamma_1}^{90^\circ}(Gated_{\gamma_2}^{All})}, \tag{3.10}$$

where $I_{\gamma_1}^{135^\circ}(Gated_{\gamma_2}^{All})$ represents the coincidence intensity of γ_1 detected at 135°, gated with γ_2 deposited in all detectors. Similarly, $I_{\gamma_1}^{90^\circ}(Gated_{\gamma_2}^{All})$ denotes the coincidence intensity of γ_1 detected at 90°, gated with γ_2 registered in all detectors. When a gate was made on a quadrupole transition, values of $R_{AD} \sim 0.8$ and ~ 1.2 were found for stretched dipole and quadrupole, respectively.

3.7.2 Linear polarization

The R_{AD} measurements can only give information about the transition multipole order. In other words, the information given by R_{AD} is necessary but not sufficient for accurate determination of the transition's electromagnetic nature. Thus, the linear polarization measurements were performed to distinguish the possible electric and magnetic nature of the γ-ray transition. We perform linear polarization measurements using the clover detectors as Compton polarimeters. An angular distribution of a linearly polarized γ rays depend on their outgoing direction with respect to beam axis, and also on their electric-field direction with respect to the reaction plane, which is defined by an outgoing γ ray and the beam axis, see Fig. 3.12 [49].

For such measurements, two polarization matrices were constructed from the data corresponding to the energy detected in any detector on one axis, while the other axis corresponded to the energy of a Compton scattered γ ray in a perpendicular or parallel direction inside a clover detector with respect to the beam direction. The polarization asymmetries (A_P) were calculated using

$$A_P = \frac{aN_V - N_H}{aN_V + N_H}, \tag{3.11}$$

where N_V and N_H are the number of γ rays scattered between the crystals of a clover detector at 90° perpendicular and parallel to the beam direction, respectively, and a is the relative efficiency parameter, given by N_H/N_V for the γ rays of the ^{152}Eu source. For pure stretched transitions, positive and negative A_P values indicate electric and magnetic transitions, respectively. It is opposite for the pure unstretched dipole transitions.

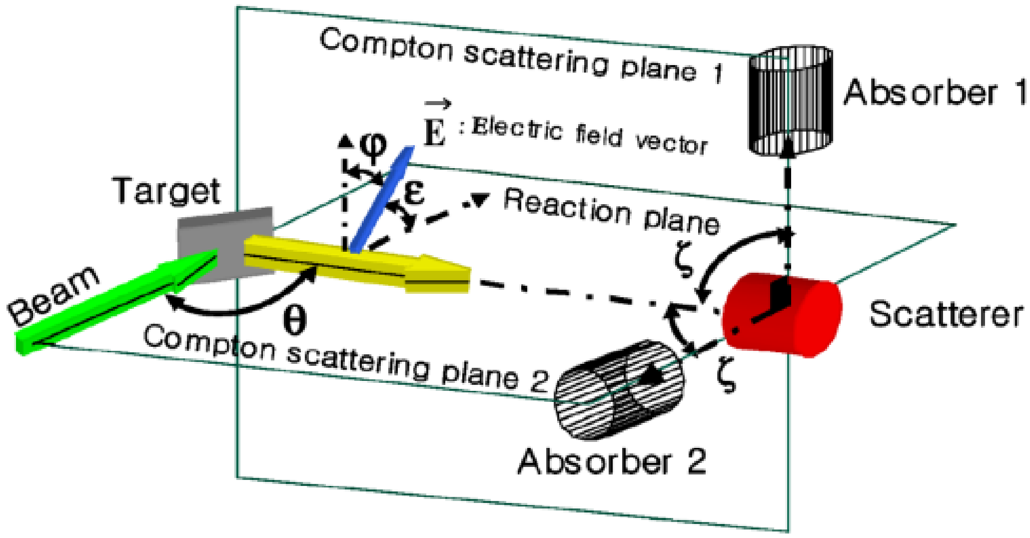

FIGURE 3.12: A diagram showing an example of a Compton polarimeter with one scatterer and two absorbers at adjacent angles.

Chapter 4

Experimental results

The decay scheme of ^{186}Os established in the present work is shown in Fig.4.1. We confirm the placements of the γ-ray transitions observed in the previous studies [50, 51] and report 21 new transitions. The newly observed transitions are shown in red in the decay scheme. Most of the new transitions belong to the positive-parity bands, particularly the bands built on the low-lying 0_2^+, 2_2^+, and 4_3^+ states. New transitions linking the positive- and negative-parity bands were also identified.
A total of about 5×10^9 γ-γ coincident events were recorded during the experiment. The ungated spectrum showing all the prominent γ-ray energies of ^{186}Os is shown in Fig. 4.2. The ungated spectrum is the total projection of the γ-γ matrix that is formed by the projection of all the counts onto one energy axis which results in a one-dimensional γ–ray spectrum. When a gate is made on a particular peak seen in the total projection, a coincidence spectrum comprised of all the γ rays in coincidence with it is observed. Observed coincidence spectra obtained by placing gates on the known and new transitions in ^{186}Os are discussed below.

The band heads of Bands 7 and 8 are isomeric states with half-lives of 8.36(24) and 5.7(4) ns, respectively [52]. In our experiment thin target was used, thus the residual nuclei recoiled out of the target. While prompt transitions are emitted at the center of the array, transitions that are positioned below an isomeric state are emitted when the nuclei have recoiled out of the target. The detector efficiency for such delayed transitions is affected by the shading of their collimators. We observed a mismatch between the measured feeding and depopulating intensities for the two isomeric levels and also for some levels that are strongly populated by isomeric decays, such as the 5^- level at 1628.6 keV and the 4^+ level at 1351.9 keV. To avoid possible impact on the measured R_{AD} ratios and A_P asymmetry for transitions at low spins, gates that bypass the isomeric feeding were selected.

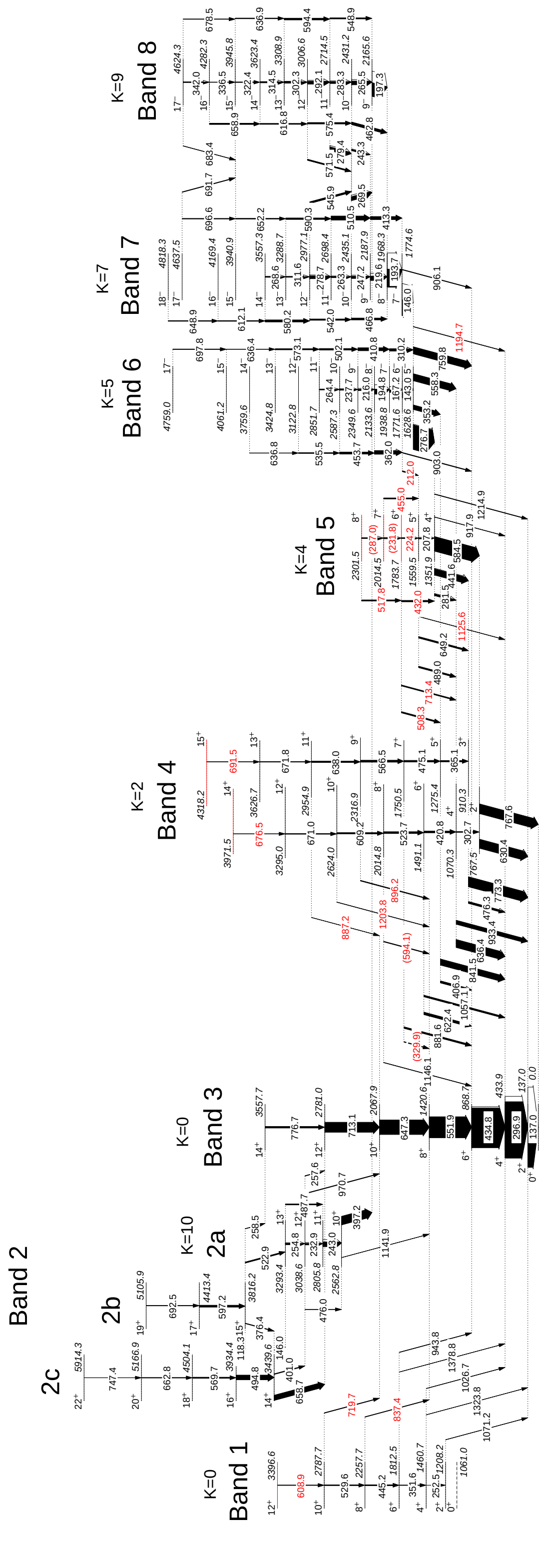

FIGURE 4.1: Decay scheme of ^{186}Os deduced from the present work. The previously known transitions are shown in black and the new ones are in red. The arrow widths are proportional to the intensity of the γ-ray transitions. The energies are given in keV. Tentative γ-ray transitions are shown in parenthesis.

The spins and parities of the previously and newly reported levels were assigned using angular distribution and linear polarization measurements. Measured angular distribution ratios (R_{AD}) plotted as a function of γ-ray energy are illustrated in Fig. 4.3. As can be seen in this figure, the majority of the measured R_{AD} lie at about 1.2 indicating a stretched quadrupole character. The γ-ray transitions with R_{AD} values of ~ 0.8 seen in the figure indicate a stretched dipole character. Linear polarization measurements for a number of transitions in ^{186}Os could not be performed due to low statistics. Experimental details of the observed bands in ^{186}Os are presented in Tabs. 4.1, 4.2, 4.3, 4.4, 4.5 and 4.6.

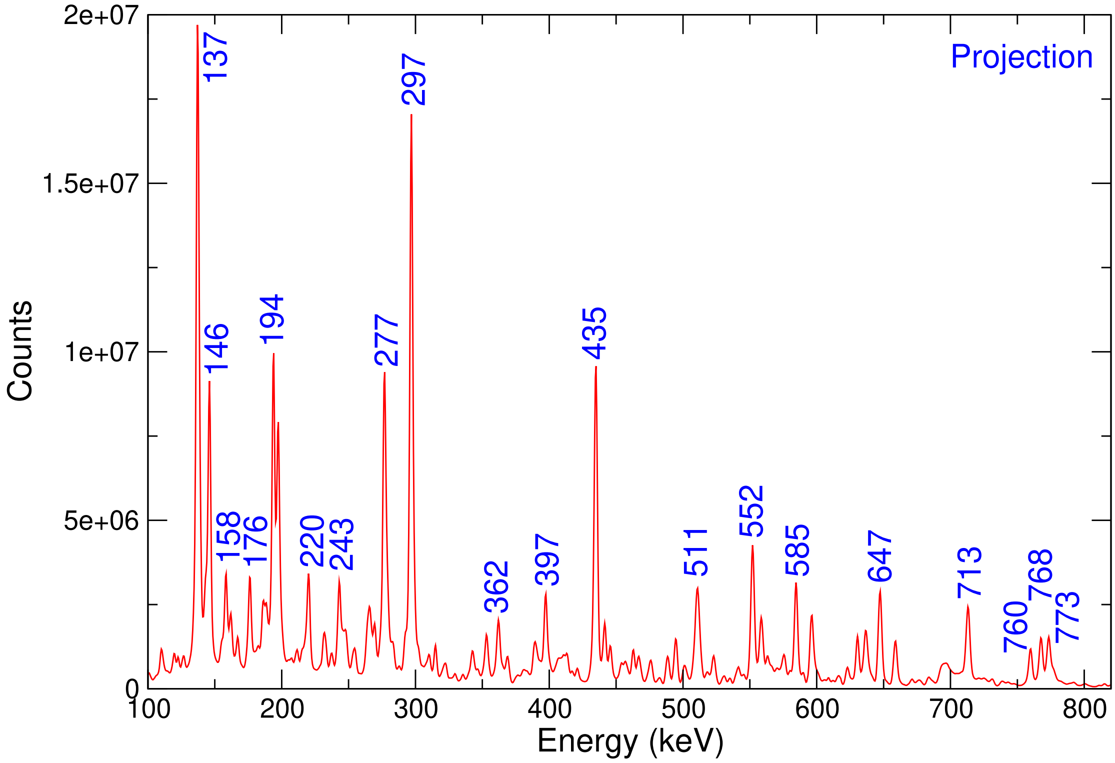

FIGURE 4.2: Ungated spectrum showing the γ-ray transitions in ^{186}Os emitted during the experiment.

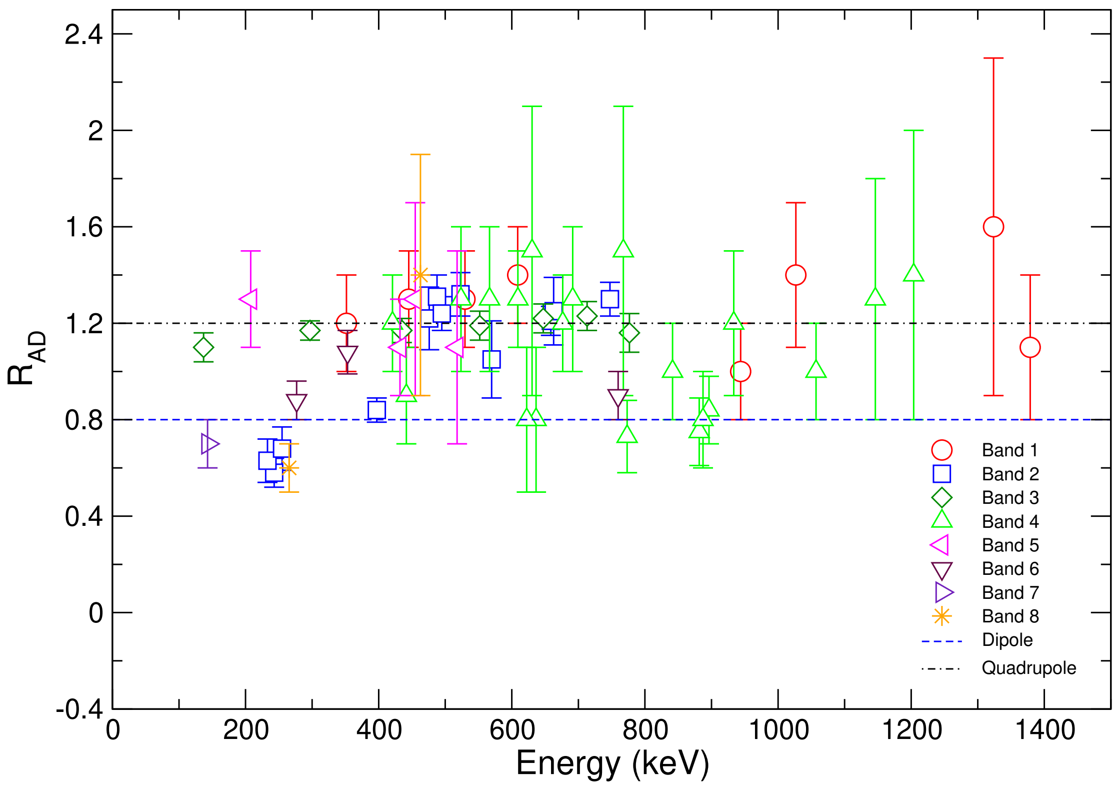

FIGURE 4.3: The measured angular distribution ratios R_{AD} plotted as function of γ-ray energy.

4.1 Band 1 (0_2^+ band)

Band 1 is the band built on the first excited 0_2^+ state. It has been reported in previous studies [50, 51, 53] . The first excited 0^+ level at 1061 keV was first identified in the transfer ^{188}Os(p, t)^{186}Os reaction experiment [53] carried out in the 1970s. R. Spanhoff *et al.*, confirmed the existence of this $K = 0$ band and extended it up to spin $I = 6^+$ in an experiment studying the decay of the 5.8-h ^{186}Ir 5^+ isomeric state [51]. The levels at 2258 (8^+) and 2788 (10^+) keV were observed in the fusion evaporation ^{176}Yb(^{14}C, 4n)^{186}Os reaction experiment [50], and their spins and parities could not be measured due to weak population of the band. The present study observed this band up to spin $I = 12^+$, extending it by one level at 3397 keV as shown in Fig. 4.4 and established the spins and parities of all of its levels. In addition, two more γ-ray transitions depopulating the 8^+ and 10^+ levels have been observed for the first time in this work. These levels decay via the 837- and 720-keV γ rays to the 8^+ and 10^+ levels of the ground-state band, respectively. Two gated spectra showing these new transitions are displayed in Fig. 4.5. As in the previous studies [50, 51], the intra-band transition linking the 2^+ and 0^+ states could not be observed in this work. Thus, the level at 1061 keV is tentatively associated with Band 1. The R_{AD} ratios measured for the observed intra-band transitions of Band 1 suggest stretched quadrupole nature. The R_{AD} ratios for the inter-band transitions are consistent with the stretched quadrupole ($\Delta I = 2$) or unstretched dipole ($\Delta I = 0$) nature, see Tab. 4.1.

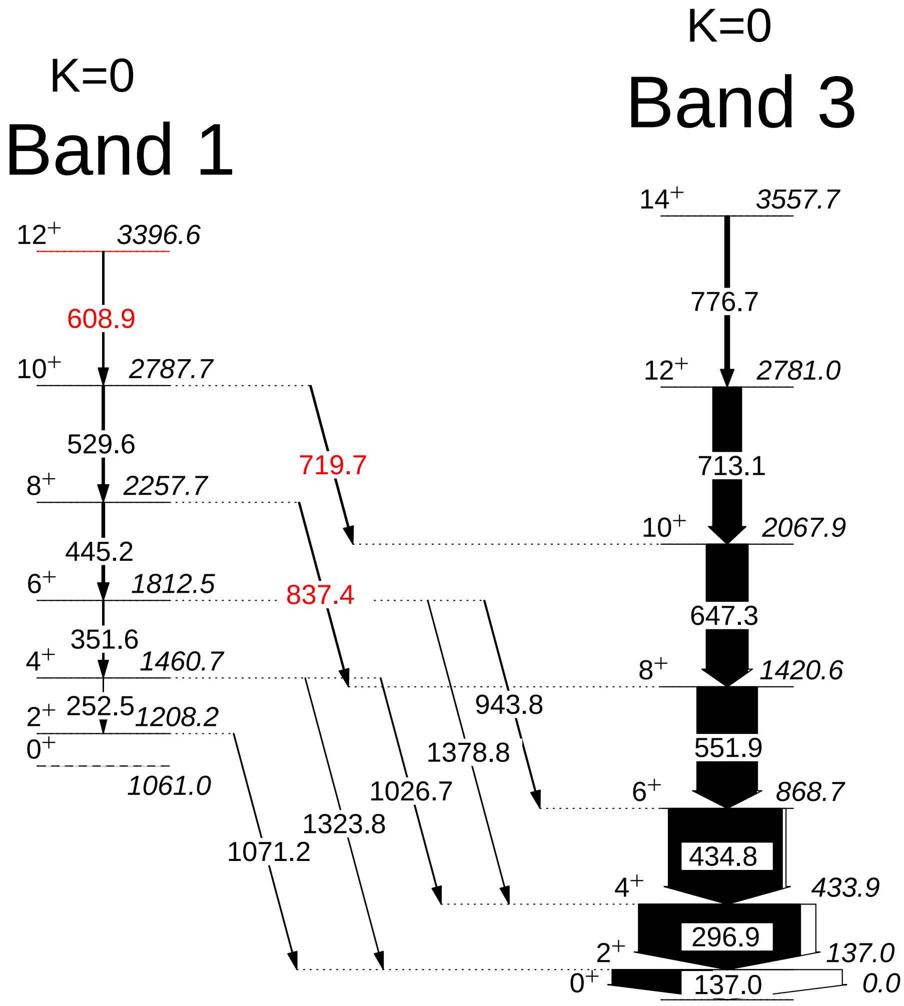

FIGURE 4.4: Partial decay scheme of ^{186}Os. The previously and newly observed transitions are respectively shown in black and red. The arrow widths are proportional to the intensity of the γ-ray transitions. The energies are given in keV.

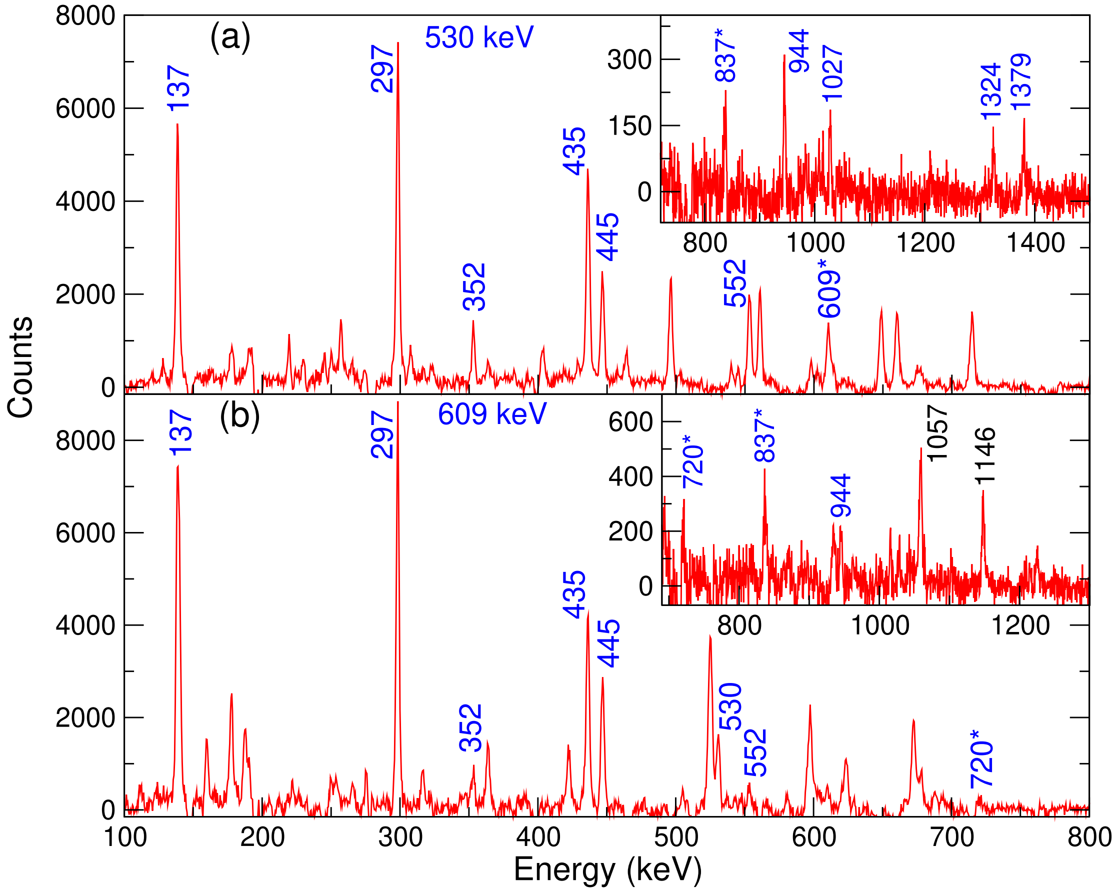

FIGURE 4.5: Gated spectra showing the transitions of Band 1, obtained by placing gates on the (a) 530- and (b) 609-keV transitions. The transitions in blue are coincidence members of Bands 1 and 2. The ones in black belong to the 2^+ γ band. The new transitions are marked with an asterisk. The insets show the high-energy parts of these gated spectra.

4.2 Band 2

We observe Band 2 up to spin $I = 22^+$. All the observed transitions for this band have been reported previously [50], and were assigned as members of a K=10 tilted-axis-cranking band associated with the $\nu i^2_{13/2}$ configuration. In the present study, Band 2 is divided into Bands 2a, 2b, and 2c, as shown in Fig. 4.6, based on the observation that this band seems to be changing its nature around spin $I = 14^+$. The states above this spin (Bands 2b and 2c) are most probably associated with $\nu i_{13/2}$ nature, a band resulting from rotation alignments of a pair of $i_{13/2}$ neutrons. The states below $I = 14^+$ show the characteristic features of a high-K band. These states are linked by strong intra-band dipole transitions, and the 10^+ state decays strongly toward the $K = 9$ band and very weakly towards the ground-state band. It is worth noting that the decay pattern changes at $I = 14$, decaying strongly towards the ground-state band. It should also be noted that the odd- and even-spin sequences, above this spin, show a significant energy staggering

TABLE 4.1: The γ-ray energies (E_γ) and the corresponding γ-ray intensities (I_γ), angular distribution ratios (R_{AD}), and linear polarization asymmetries (A_P) for the transitions of Band 1, shown in Fig. 4.4. The energies of the initial states (E_i) and the band where the transitions feed into ($Band\#$), as well as the spin assignment for the initial (I_i^π) and final (I_f^π) states are also listed. The measured γ-ray energies have uncertainties of 0.3 keV and up to 0.5 keV for the weaker and doublet transitions. Information that could not be obtained is indicated with a dash symbol.

			Band 1			
E_i	E_γ	I_γ	$I_i^\pi \rightarrow I_f^\pi$	R_{AD}	A_P	$Band\#$
1208.2	1071.2	0.41(15)	$2^+ \rightarrow 2^+$	-	-	3
1460.7	252.5	0.08(4)	$4^+ \rightarrow 2^+$	-	-	1
1460.7	1026.7	0.5(2)	$4^+ \rightarrow 4^+$	1.4(3)	-	3
1460.7	1323.8	0.4(1)	$4^+ \rightarrow 2^+$	1.6(7)	-	3
1812.5	351.6	0.8(1)	$6^+ \rightarrow 4^+$	1.2(2)	-	1
1812.5	943.8	0.7(1)	$6^+ \rightarrow 6^+$	1.0(2)	-	3
1812.5	1378.8	0.3(1)	$6^+ \rightarrow 4^+$	1.1(3)	-	3
2257.7	445.2	1.6(2)	$8^+ \rightarrow 6^+$	1.3(2)	-	1
2257.7	837.4	0.3(1)	$8^+ \rightarrow 8^+$	-	-	3
2787.7	529.6	1.4(2)	$10^+ \rightarrow 8^+$	1.3(2)	-	1
2787.7	719.7	0.3(1)	$10^+ \rightarrow 10^+$	-	-	3
3396.6	608.9	0.8(2)	$12^+ \rightarrow 10^+$	1.4(2)	-	1

and undetected intra-band dipole transitions, which is not expected for a high-K band. Based on these considerations, we propose that Bands 2b and 2c are most probably associated with $\nu i_{13/2}$ nature with low K, where the $\nu i_{13/2}$ are approximately aligned along the rotational axis , while the low-spin part of the band, Band 2a, corresponds to the $K = 10$ $\nu i_{13/2}$ configuration, as previously proposed [50].

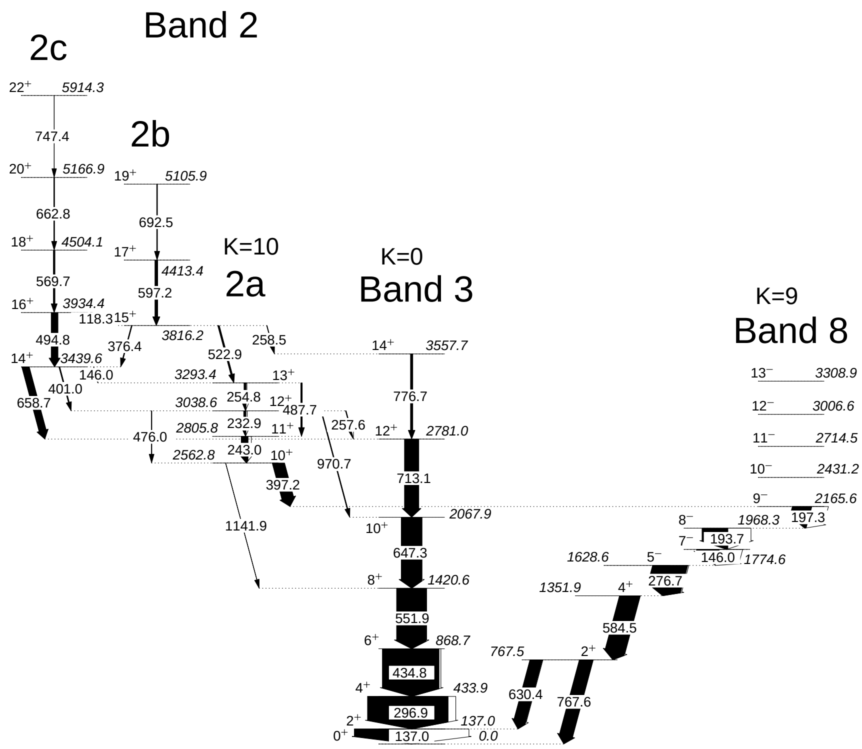

FIGURE 4.6: Partial decay scheme of ^{186}Os. The arrow widths are proportional to the intensity of the γ-ray transitions. The energies are given in keV.

4.3 Band 3 (ground-state band)

The transitions of Band 3 (ground-state band) have been reported previously in many studies [1, 50, 51, 53]. This band has been observed up to spin of $I = 14^+$. The present study also observed all the previously reported states and confirm the spin-parity assignment that have been previously made. The measured angular distribution ratios for this band, indicating a stretched quadrupole nature, are listed in Tab. 4.3. It should be noted that the states of this band are yrast band members (lowest energy per given spin) up to spin $I = 12^+$. Thus, nuclear properties interchange occur around the $I = 12^+ - 14^+$ spins, and the spin members of Band 2c become the yrast band from the $I = 14^+$ to $I = 22^+$ states. A coincidence spectrum obtained by placing a gate on 713-keV transition of Band 3 is displayed in Fig. 4.7, illustrating the observed coincidence γ-ray energies.

TABLE 4.2: The γ-ray energies (E_γ) and the corresponding γ-ray intensities (I_γ), angular distribution ratios (R_{AD}), and linear polarization asymmetries (A_P) for the transitions of Band 2, shown in Fig. 4.6. The energies of the initial states (E_i) and the band where the transitions feed into ($Band\#$), as well as the spin assignment for the initial (I_i^π) and final (I_f^π) states are also listed. The measured γ-ray energies have uncertainties of 0.3 keV and up to 0.5 keV for the weaker and doublet transitions. Information that could not be obtained is indicated with a dash symbol.

E_i	E_γ	I_γ	$I_i^\pi \rightarrow I_f^\pi$	R_{AD}	A_P	$Band\#$
			Band 2a			
2562.8	397.2	14.5(5)	$10^+ \rightarrow 9^-$	0.84(5)	0.05(2)	8
2562.8	1141.9	0.30(5)	$10^+ \rightarrow 8^+$	-		3
2805.8	243.0	9.4(3)	$11^+ \rightarrow 10^+$	0.58(6)		$2a$
3038.6	232.9	2.9(3)	$12^+ \rightarrow 11^+$	0.63(9)	-	$2a$
3038.6	257.6	0.6(1)	$12^+ \rightarrow 12^+$	-	-	3
3038.6	476.0	0.7(1)	$12^+ \rightarrow 10^+$	1.22(13)	-	$2a$
3038.6	970.7	1.0(1)	$12^+ \rightarrow 10^+$	-	-	3
3293.4	254.8	2.6(2)	$13^+ \rightarrow 12^+$	0.68(9)	-	$2a$
3293.4	487.7	1.7(2)	$13^+ \rightarrow 11^+$	1.31(9)	0.03(3)	$2a$
			Band 2b			
3816.2	258.5	0.4(1)	$15^+ \rightarrow 14^+$	-	-	3
3816.2	376.4	0.9(1)	$15^+ \rightarrow 14^+$	-	-	$2c$
3816.2	522.9	2.0(2)	$15^+ \rightarrow 13^+$	1.32(9)	-	$2a$
4413.4	597.2	2.5(5)	$17^+ \rightarrow 15^+$	-	-	$2b$
5105.9	692.5	2.0(5)	$19^+ \rightarrow 17^+$	-	-	$2b$
			Band 2C			
3439.6	146.0	0.05(4)	$14^+ \rightarrow 13^+$	-	-	$2a$
3439.6	401.0	1.1(2)	$14^+ \rightarrow 12^+$	-	-	$2a$
3439.6	658.7	9.1(8)	$14^+ \rightarrow 12^+$	1.21(6)	0.04(2)	3
3934.4	118.3	0.4(1)	$16^+ \rightarrow 15^+$	-	-	$2b$
3934.4	494.8	8.1(5)	$16^+ \rightarrow 14^+$	1.24(7)	0.07(3)	$2c$
4504.1	569.7	3.4(5)	$18^+ \rightarrow 16^+$	1.05(16)	-	$2c$
5166.9	662.8	1.7(4)	$20^+ \rightarrow 18^+$	1.25(14)	-	$2c$
5914.3	747.4	0.5(2)	$22^+ \rightarrow 20^+$	1.3(7)	-	$2c$

4.4 Band 4 ($2_2^+ \gamma$ band)

The previous work [50] observed the even- and odd-spin sequences of the 2_2^+ band up to spins of 10^+ and 13^+, respectively. The current work confirms the placements of these states, and extends the band by two new levels at 3971.5 and 4318.2 keV, as shown in Fig. 4.8. Five new linking transitions of Band 4 decaying out of spins 7^+, 8^+, 9^+, 10^+, and 11^+ to the states of Band 3 have been identified. The new transitions are shown in the coincidence spectra of 4.9 and 4.10, obtained by placing gates on the previously and newly observed 671 and 677-keV transitions, respectively. Transitions linking the odd- and even-spin members of Band 4 could not be observed in this current work. The three previously reported ones, namely 143 keV ($3^+ \rightarrow 2^+$), 161 keV ($4^+ \rightarrow 3^+$), and

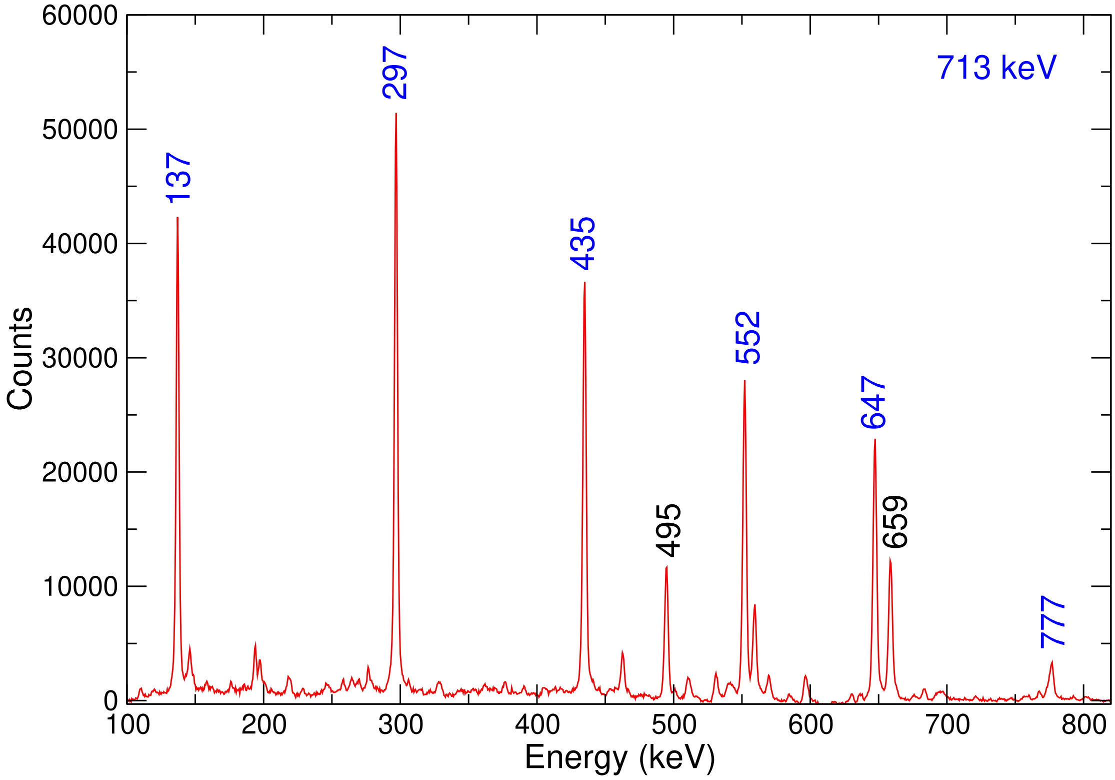

FIGURE 4.7: Gated spectrum showing the transitions of the ground-state band (Band 3) shown in blue. Transitions in black belong to other bands in ^{186}Os.

TABLE 4.3: The γ-ray energies (E_γ) and the corresponding γ-ray intensities (I_γ), angular distribution ratios (R_{AD}), and linear polarization asymmetries (A_P) for the transitions of Band 3. The energies of the initial states (E_i) and the band where the transitions feed into ($Band\#$), as well as the spin assignment for the initial (I_i^π) and final (I_f^π) states are also listed. The measured γ-ray energies have uncertainties of 0.3 keV and up to 0.5 keV for the weaker and doublet transitions. Information that could not be obtained is indicated with a dash symbol.

E_i	E_γ	I_γ	$I_i^\pi \to I_f^\pi$	R_{AD}	A_P	$Band\#$
			Band 3			
137.0	137.0	62(3)	$2^+ \to 0^+$	1.10(6)	-	3
433.9	296.9	100(3)	$4^+ \to 2^+$	1.17(4)	0.05(2)	3
868.7	434.8	70(3)	$6^+ \to 4^+$	1.17(5)	0.03(2)	3
1420.6	551.9	37(2)	$8^+ \to 6^+$	1.19(6)	0.07(3)	3
2067.9	647.3	26(1)	$10^+ \to 8^+$	1.22(6)	0.04(2)	3
2781.0	713.1	18(1)	$12^+ \to 10^+$	1.23(6)	0.04(2)	3
3557.7	776.7	2.9(2)	$14^+ \to 12^+$	1.16(8)	0.06(4)	3

216 keV ($6^+ \to 5^+$) have the γ-ray branching intensities of 3.3, 1.0 and 3.2, respectively [52]. Our data suggest that if these transitions exist their branchings are less than 1%.

The measured R_{AD} ratios for the intra-band $E2$ transitions of Band 4 are consistent with stretched quadrupole nature, see Tab. 4.4. The measured R_{AD} ratios for the inter-band $\Delta I = 0$, 1 and 2 transitions are consistent with the present spin assignments. The previously observed $\Delta I = 1$ transitions decaying from the γ band to the ground-state band were assigned almost pure (more than 99%) unstretched $E2$ nature [52]. The values, measured in this work, of R_{AD} of ~ 0.8 for these transitions and for the newly observed $\Delta I = 1$ transitions are in agreement with both, (i) almost pure unstretched $E2$ nature, and (ii) almost pure $M1$ multipolarity. Our linear polarization results, where available, did not have the needed precision to distinguish between these two options. It can be noted that the measured R_{AD} values of 0.8(3) for the $6^+ \rightarrow 6^+$ and $4^+ \rightarrow 4^+$ transitions linking the γ and the ground-state bands, are too low for pure unstretched dipole nature and suggest considerable $E2$ admixture, in line with previous results where dominating $E2$ components were assigned [52].

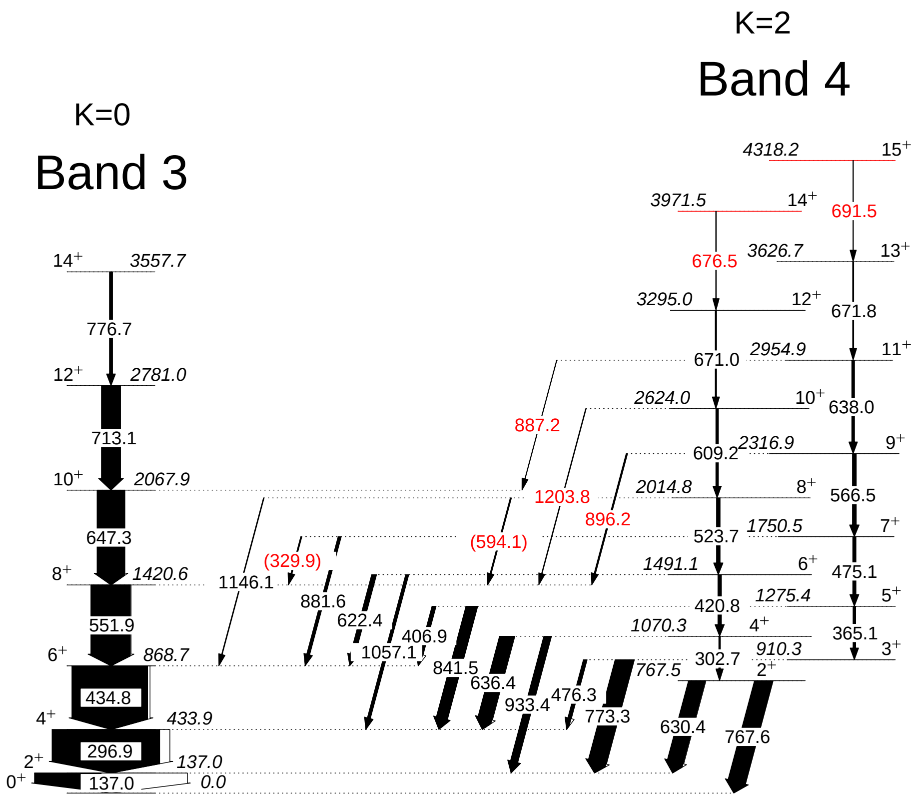

FIGURE 4.8: Partial decay scheme of ^{186}Os. The previously and newly observed transitions are respectively shown in black and red. The arrow widths are proportional to the intensity of the γ-ray transitions. The energies are given in keV.

TABLE 4.4: The γ-ray energies (E_γ) and the corresponding γ-ray intensities (I_γ), angular distribution ratios (R_{AD}), and linear polarization asymmetries (A_P) for the transitions of Band 4, shown in Fig. 4.8. The energies of the initial states (E_i) and the band where the transitions feed into ($Band\#$), as well as the spin assignment for the initial (I_i^π) and final (I_f^π) states are also listed. The measured γ-ray energies have uncertainties of 0.3 keV and up to 0.5 keV for the weaker and doublet transitions. Information that could not be obtained is indicated with a dash symbol.

E_i	E_γ	I_γ	$I_i^\pi \rightarrow I_f^\pi$	R_{AD}	A_P	$Band\#$
			Band 4			
767.5	630.4	15(1)	$2^+ \rightarrow 2^+$	1.5(6)	-	3
767.5	767.6	17(1)	$2^+ \rightarrow 0^+$	1.5(6)	-	3
910.3	476.3	1.9(2)	$3^+ \rightarrow 4^+$	-	-	3
910.3	773.3	17(1)	$3^+ \rightarrow 2^+$	0.73(15)	-	3
1070.3	302.7	2.2(4)	$4^+ \rightarrow 2^+$	-	-	4
1070.3	636.4	14.2(5)	$4^+ \rightarrow 4^+$	0.8(3)	-	3
1070.3	933.4	11.9(6)	$4^+ \rightarrow 2^+$	1.2(3)	-	3
1275.4	365.1	2.4(2)	$5^+ \rightarrow 3^+$	-	-	4
1275.4	406.9	1.4(2)	$5^+ \rightarrow 6^+$	-	-	3
1275.4	841.5	10.6(4)	$5^+ \rightarrow 4^+$	1.0(2)	-	3
1491.1	420.8	4.3(2)	$6^+ \rightarrow 4^+$	1.2(2)	-	4
1491.1	622.4	4.3(3)	$6^+ \rightarrow 6^+$	0.8(3)	-	3
1491.1	1057.1	3.9(3)	$6^+ \rightarrow 4^+$	1.0(2)	-	3
1750.5	(329.9)	0.3(1)	$7^+ \rightarrow 8^+$	-	-	3
1750.5	475.1	2.7(2)	$7^+ \rightarrow 5^+$	-	-	4
1750.5	881.6	2.8(2)	$7^+ \rightarrow 6^+$	0.75(14)	-0.08(6)	3
2014.8	523.7	3.3(2)	$8^+ \rightarrow 6^+$	1.3(3)	0.05(3)	4
2014.8	(594.1)	-	$8^+ \rightarrow 8^+$	-	-	3
2014.8	1146.1	0.4(1)	$8^+ \rightarrow 6^+$	1.3(5)	-	3
2316.9	566.5	3.5(2)	$9^+ \rightarrow 7^+$	1.3(3)	-	4
2316.9	896.2	1.3(2)	$9^+ \rightarrow 8^+$	0.84(14)	-0.14(8)	3
2624.0	609.2	2.4(2)	$10^+ \rightarrow 8^+$	1.3(2)	-	4
2624.0	1203.8	0.24(7)	$10^+ \rightarrow 8^+$	1.4(6)	-	3
2954.9	638.0	2.6(2)	$11^+ \rightarrow 9^+$	-	-	4
2954.9	887.2	0.41(6)	$11^+ \rightarrow 10^+$	0.8(2)	-	3
3295.0	671.0	1.24(9)	$12^+ \rightarrow 10^+$	-	-	4
3626.7	671.8	0.98(8)	$13^+ \rightarrow 11^+$	-	-	4
3971.5	676.5	0.51(5)	$14^+ \rightarrow 12^+$	1.2(2)	-	4
4318.2	691.5	0.50(5)	$15^+ \rightarrow 13^+$	1.3(3)	-	4

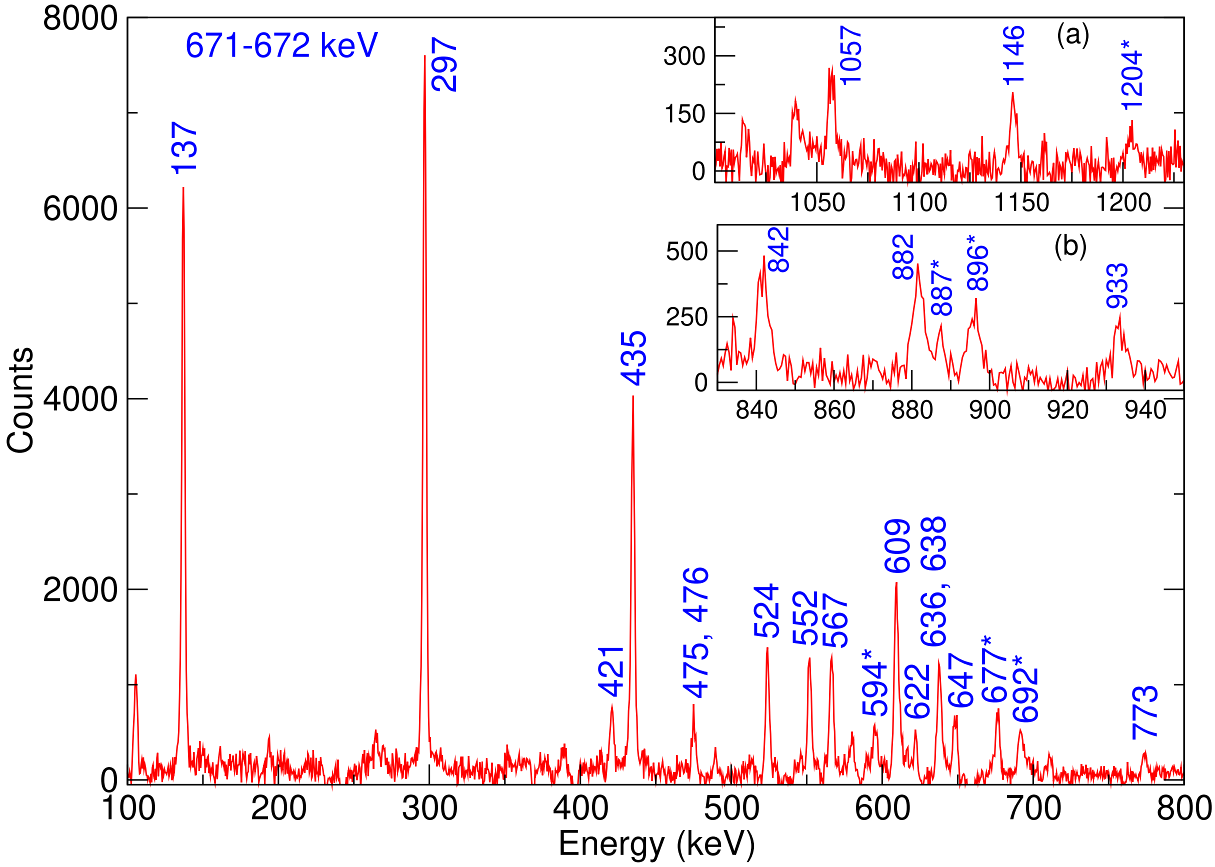

FIGURE 4.9: A coincidence spectrum showing the transitions of Band 4, obtained by placing a gate on the 671-keV transition. The transitions in blue are coincidence members of Bands 3 and 4. The new transitions are marked with an asterisk. The insets show the high-energy parts of this gated spectrum.

4.5 Band 5 ($4_3^+ \gamma$ band)

Previously [50], two levels of Band 5 were known. The current study has extended this band by three new levels at 1783.7, 2014.5, and 2301.5 keV, and nine new intra-band and inter-band transitions, see Fig. 4.11. As seen in this figure, Band 5 decays strongly to Band 4. Seven out of the ten observed inter-band transitions of Band 5 decay to Band 4, the 2_2^+ band. The other three transitions which have weak intensities decay toward the ground-state band. Contrary to the 2_2^+ γ band the intra-band $\Delta I = 1$ transitions are relatively strong with relative intensity of $\sim 30\%$ of the corresponding intra-band $E2$ transitions. Shown in Fig. 4.12 are gated spectra illustrating the transitions of Band 5. The spectra were obtained by placing gates on the two previously reported γ rays of 208 and 585 keV, and on the newly observed 518-keV γ ray. A spectrum gated on the 842-keV transition of Band 4 is shown in Fig. 4.13, also illustrating the new members of Band 5. The R_{AD} values for the intra-band 432-, 455- and 518-keV transitions suggest quadrupole nature, see Tab. 4.5.

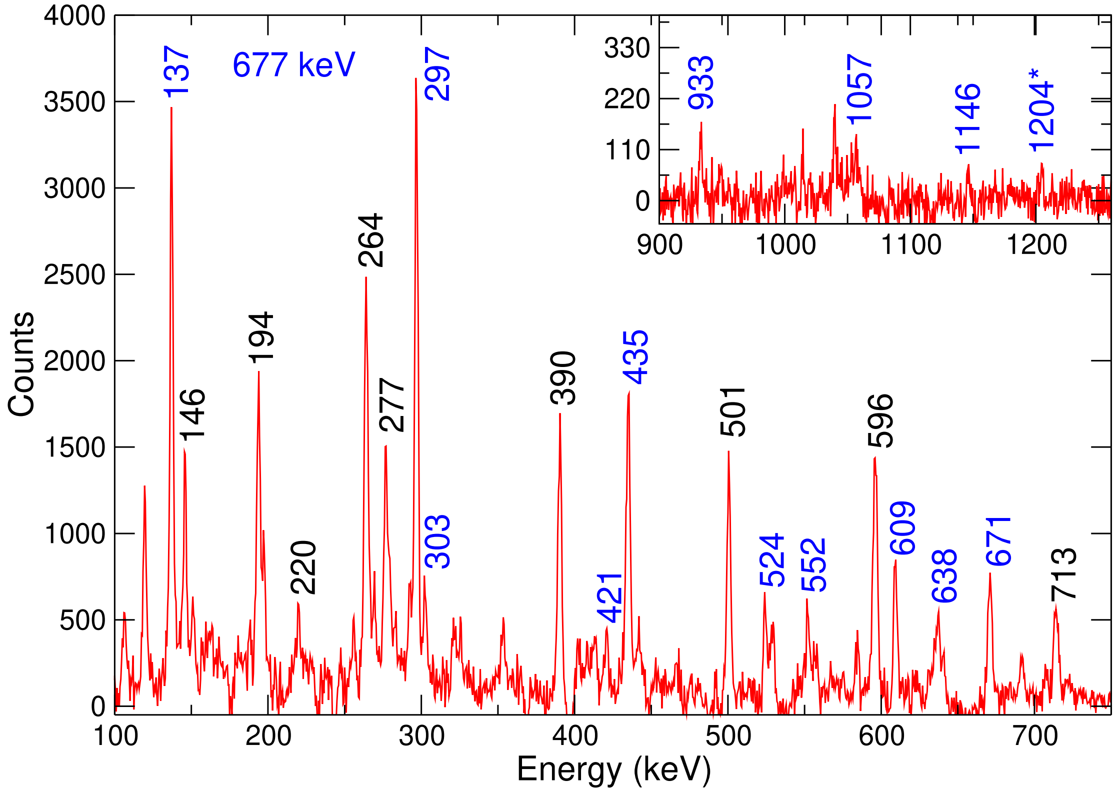

FIGURE 4.10: Gated spectrum showing the γ rays in coincidence with the newly observed 677-keV transition. The transitions in blue are coincidence members of Bands 3 and 4, and those in black are other transitions in ^{186}Os not associated with Band 4. The new transitions are marked with an asterisk. The inset show the high-energy part of this gated spectrum.

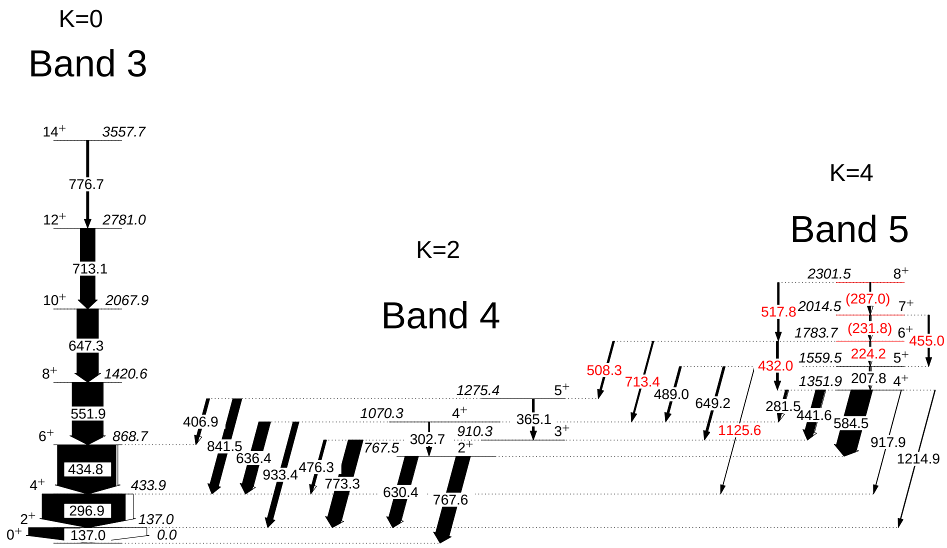

FIGURE 4.11: Partial decay scheme of ^{186}Os showing Band 5 and its decays. The previously and newly observed transitions are respectively shown in black and red. The arrow widths are proportional to the intensity of the γ-ray transitions. The energies are given in keV. Tentative γ-ray energies are given in parenthesis.

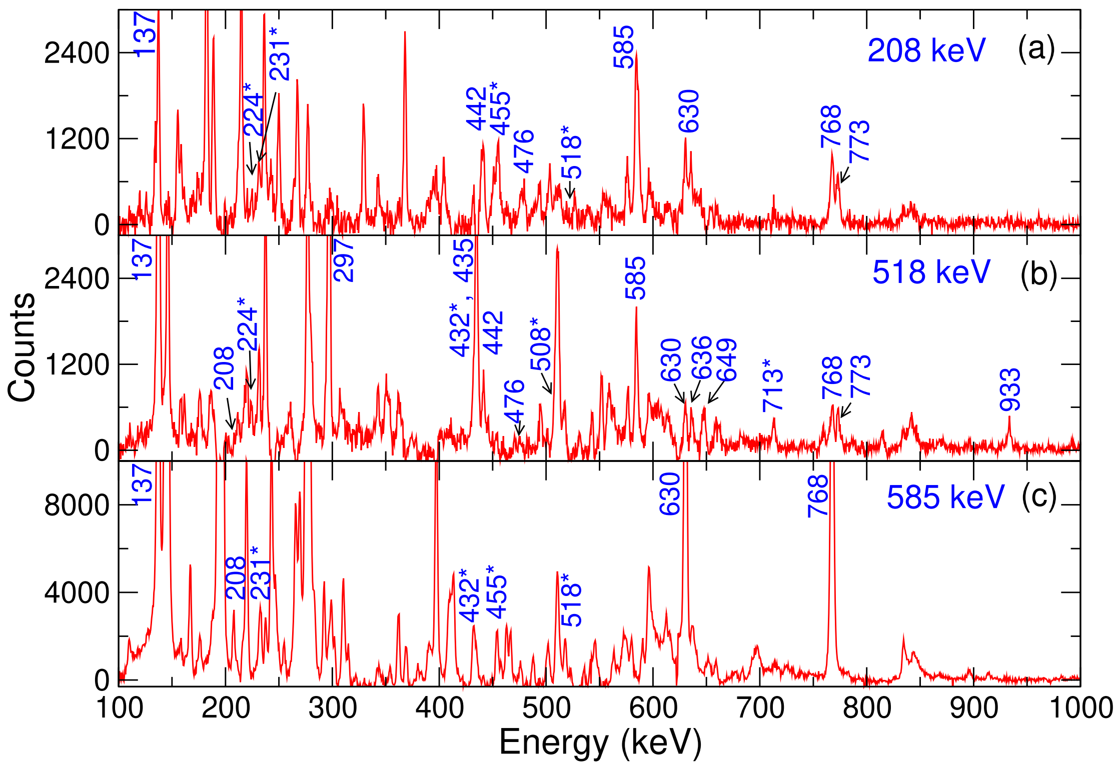

FIGURE 4.12: Spectra, gated on (a) 208-keV, (b) 518-keV, (c) and 585-keV γ-ray transitions, showing the coincidence γ-ray transitions of Bands 3, 4, and 5. The new transitions of Band 5 are marked with an asterisk.

4.6 Bands 6, 7, and 8 (Negative-parity bands)

Bands 6, 7, and 8 are negative-parity bands built on the $K = 5^-$, $K = 7^-$, and $K = 9^-$ isomeric states. They have been previously reported [50, 51]. The present study observes bands 6, 7 and 8 up to spins of 17^-, 18^-, and 17^-, respectively, and report two new linking transitions, as shown in Fig. 4.14. The two linking 212- and 1195-keV transitions decay out of the 6^- state of Band 6 to the 5^+ of Band 5, and from the 5^- state of Band 6 to the 4^+ state of Band 3, respectively. The previous work [50] made the comparisons of the alignment curves of these negative-parity bands and those of bands observed in the odd-A neighboring nucleus, ^{185}Os, and found that the alignment curves for Bands 6, 7, and 8 are similar to those of the $11/2^+$ band in ^{185}Os, suggesting that the same $i_{13/2}$ neutron is involved. Based on this, the bands bulit on the $K = 5^-$, $K = 7^-$, and $K = 9^-$ states were respectively assigned the $\nu\{11/2^+[615], -1/2^-[510]\}$, $\nu\{11/2^+[615], 3/2^-[512]\}$, and $\nu\{11/2^+[615], 7/2^-[503]\}$ configurations, resulting from the 2-quasineutron coupling. It should be noted that a number of transitions (marked with asterisks) linking the excited bands in Fig. 4.14 are not allowed by the K-selection rule. Thus, the validity of the K-selection rule will be examined in the discussion section.

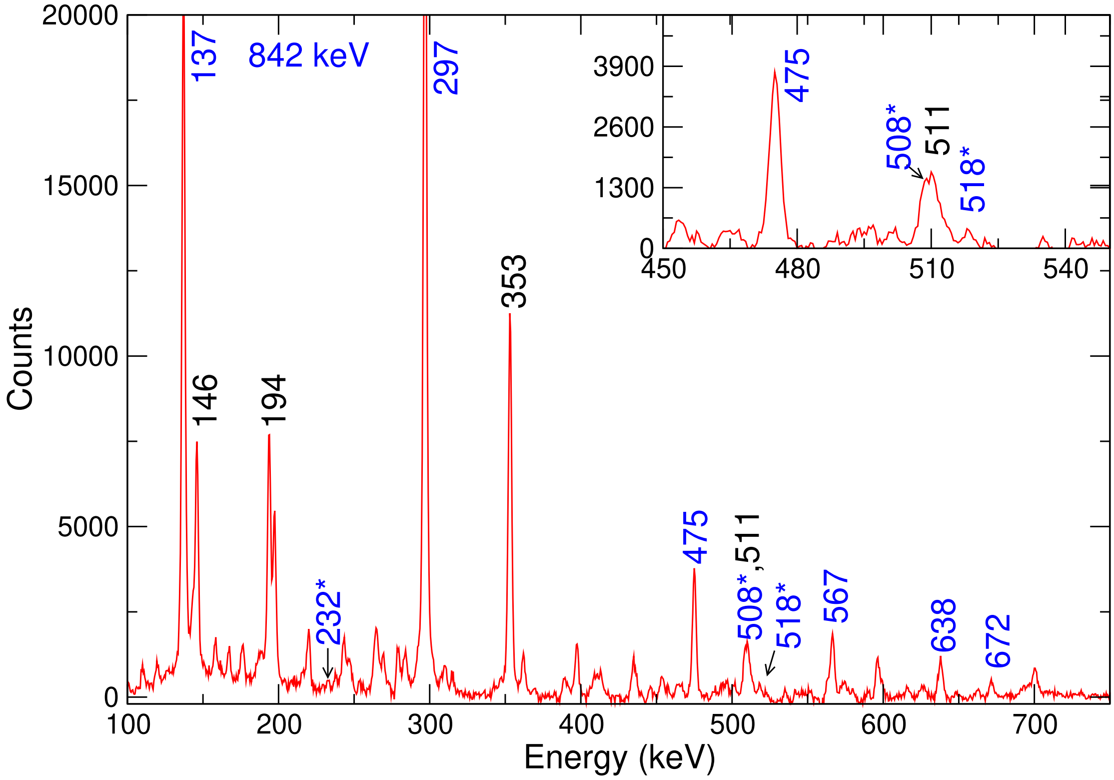

FIGURE 4.13: Coincidence spectrum showing the γ rays in coincidence with 842 keV. The transitions in blue are coincidence members of Bands 3, 4, and 5. The transitions in black are other transitions in ^{186}Os not associated with Band 5. The new transitions are marked with an asterisk. The inset shows the 450-560 keV energy part of this gated spectrum.

TABLE 4.5: The γ-ray energies (E_γ) and the corresponding γ-ray intensities (I_γ), angular distribution ratios (R_{AD}), and linear polarization asymmetries (A_P) for the transitions of Band 5, shown in Fig. 4.11. The energies of the initial states (E_i) and the band where the transitions feed into (*Band#*), as well as the spin assignment for the initial (I_i^π) and final (I_f^π) states are also listed. The measured γ-ray energies have uncertainties of 0.3 keV and up to 0.5 keV for the weaker and doublet transitions. Information that could not be obtained is indicated with a dash symbol.

E_i	E_γ	I_γ	$I_i^\pi \rightarrow I_f^\pi$	R_{AD}	A_P	*Band#*
			Band 5			
1351.9	281.5	3.5(8)	$4^+ \rightarrow 4^+$	-	-	4
1351.9	441.6	10.8(4)	$4^+ \rightarrow 3^+$	0.9(2)	-	4
1351.9	584.5	24.8(8)	$4^+ \rightarrow 2^+$	1.1(1)	-	4
1351.9	917.9	0.5(1)	$4^+ \rightarrow 4^+$	-	-	3
1351.9	1214.9	0.8(1)	$4^+ \rightarrow 2^+$	-	-	3
1559.5	207.8	1.7(2)	$5^+ \rightarrow 4^+$	1.3(2)	-	5
1559.5	489.0	2.5(2)	$5^+ \rightarrow 4^+$	-	-	4
1559.5	649.2	2.9(2)	$5^+ \rightarrow 3^+$	-	-	4
1559.5	1125.6	0.4(1)	$5^+ \rightarrow 4^+$	-	-	3
1783.7	224.2	0.9(2)	$6^+ \rightarrow 5^+$	-	-	5
1783.7	432.0	2.7(2)	$6^+ \rightarrow 4^+$	1.1(2)	-	5
1783.7	508.3	0.6(3)	$6^+ \rightarrow 5^+$	-	-	4
1783.7	713.4	0.7(4)	$6^+ \rightarrow 4^+$	-	-	4
2014.5	(231.8)	1.3(6)	$7^+ \rightarrow 6^+$	-	-	5
2014.5	455.0	2.8(2)	$7^+ \rightarrow 5^+$	1.3(4)	-	5
2301.5	(287.0)	1.22(10)	$8^+ \rightarrow 7^+$	-	-	5
2301.5	517.8	2.1(2)	$8^+ \rightarrow 6^+$	1.1(4)	-	5

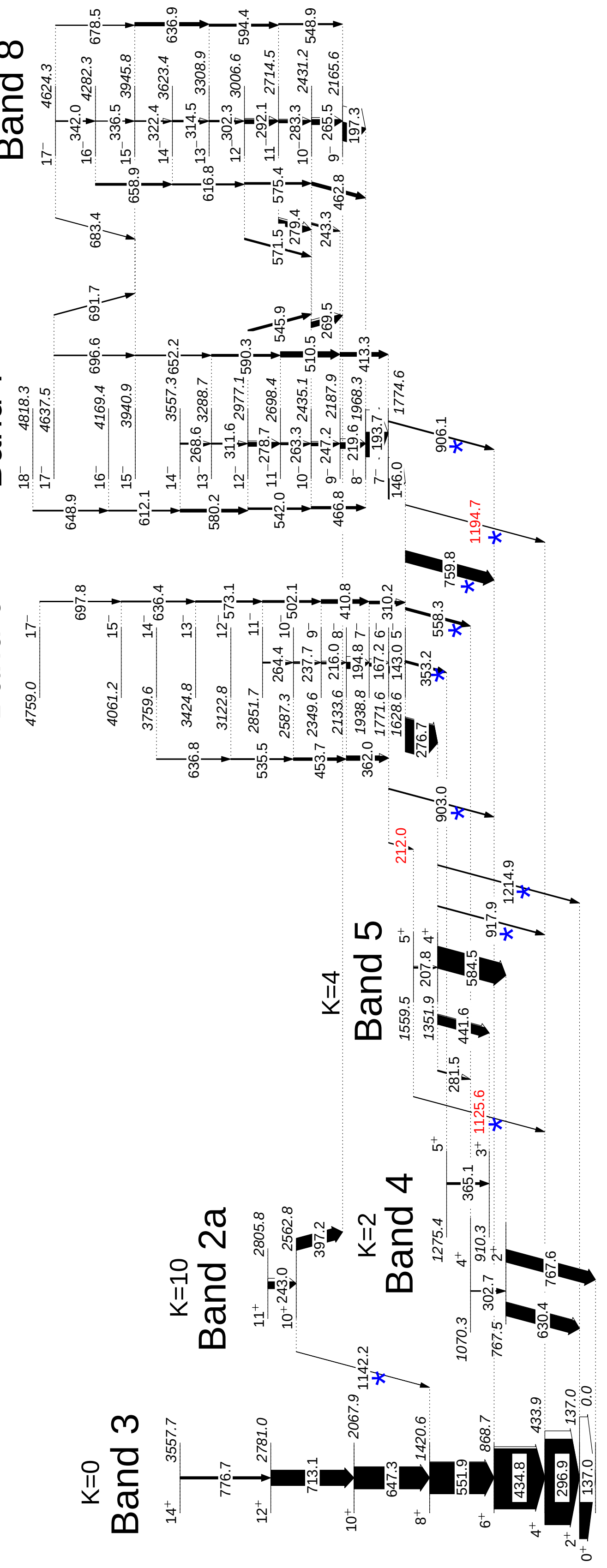

FIGURE 4.14: Partial decay scheme of ^{186}Os established in the present work. Transitions shown in red are new. The transitions marked with blue asterisks are forbidden by the K-selection rule. The arrow widths are proportional to the intensity of the γ-ray transitions, and the energies are given in keV.

TABLE 4.6: The γ-ray energies (E_γ) and the corresponding γ-ray intensities (I_γ), angular distribution ratios (R_{AD}), and linear polarization asymmetries (A_P) for the transitions of Bands 6, 7, and 8, shown in Fig. 4.14. The energies of the initial states (E_i) and the band where the transitions feed into ($Band\#$), as well as the spin assignment for the initial (I_i^π) and final (I_f^π) states are also listed. The measured γ-ray energies have uncertainties of 0.3 keV and up to 0.5 keV for the weaker and doublet transitions. Information that could not be obtained is indicated with a dash symbol.

E_i	E_γ	I_γ	$I_i^\pi \to I_f^\pi$	R_{AD}	A_P	$Band\#$
			Band6			
1628.6	276.7	43.5(13)	$5^- \to 4^+$	0.88(8)	-	5
1628.6	353.2	7.4(3)	$5^- \to 5^+$	1.08(9)	-	4
1628.6	558.3	11.7(4)	$5^- \to 4^+$	-	-	4
1628.6	759.8	12.3(4)	$5^- \to 6^+$	0.9(1)	-	3
1628.6	1194.7	0.16(7)	$5^- \to 4^+$	-	-	3
1771.6	143.0	9.7(3)	$6^- \to 5^-$	0.7(1)	-	6
1771.6	212.0	0.9(2)	$6^- \to 5^+$	-	-	5
1771.6	903.0	1.3(2)	$6^- \to 6^+$	-	-	3
1938.8	167.2	4.41(17)	$7^- \to 6^-$	-	-	6
1938.8	310.2	4.02(17)	$7^- \to 5^-$	-	-	6
2133.6	194.8	8.9(3)	$8^- \to 7^-$	-	-	6
2133.6	362.0	6.33(24)	$8^- \to 6^-$	-	-	6
2349.6	216.0	2.38(11)	$9^- \to 8^-$	-	-	6
2349.6	410.8	5.13(19)	$9^- \to 7^-$	-	-	6
2587.3	237.7	1.79(9)	$10^- \to 9^-$	-	-	6
2587.3	453.7	3.55(15)	$10^- \to 8^-$	-	-	6
2851.7	264.4	1.21(9)	$11^- \to 10^-$	-	-	6
2851.7	502.1	2.73(12)	$11^- \to 9-$	-	-	6
3122.8	535.5	1.42(9)	$12^- \to 10^-$	-	-	6
3424.8	573.1	2.01(10)	$13^- \to 11^-$	-	-	6
3759.6	638.8	0.48(8)	$14^- \to 12^-$	-	-	6
4061.2	636.4	0.54(8)	$15^- \to 13^-$	-	-	6
4759.0	697.8	0.89(5)	$17^- \to 15^-$	-	-	6
			Band 7			
1774.6	146.0	27.4(9)	$7^- \to 5^-$	0.86(1)	-	6
1774.6	906.1	0.5(1)	$7^- \to 6^+$	-	-	3
1968.3	193.7	35.6(11)	$8^- \to 7^-$	0.71(1)	-	7
2187.9	219.6	7.9(3)	$9^- \to 8^-$	0.57(2)	-	7
2187.9	413.3	5.32(20)	$9^- \to 7^-$	1.11(2)	-	7
2435.1	247.2	4.04(15)	$10^- \to 9^-$	0.54(5)	-	7
2435.1	269.5	6.99(24)	$10^- \to 9^-$	-	-	8
2435.1	466.8	3.33(14)	$10^- \to 8^-$	1.11(7)	-	7
2698.4	263.3	2.25(11)	$11^- \to 10-$	-	-	7
2698.4	510.5	7.1(3)	$11^- \to 9^-$	1.17(2)	-	7
2977.1	278.7	5.06(21)	$12^- \to 11^-$	-	-	7
2977.1	542.0	2.36(11)	$12^- \to 10^-$	1.28(10)	-	7
2977.1	545.9	3.00(13)	$12^- \to 10^-$	-	-	8
3288.7	311.6	1.36(9)	$13^- \to 12^-$	-	-	7
3288.7	590.3	2.69(12)	$13^- \to 11^-$	-	-	7
3557.3	268.6	1.35(9)	$14^- \to 13^-$	-	-	7
3557.3	580.2	3.68(14)	$14^- \to 12^-$	1.39(14)	-	7
3940.9	652.2	1.28(8)	$15^- \to 13^-$	0.81(14)	-	7
4169.4	612.1	1.38(9)	$16^- \to 14^-$	-	-	7
4637.5	691.7	0.90(6)	$17^- \to 15^-$	-	-	8
4637.5	696.6	1.07(6)	$17^- \to 15^-$	-	-	7
4818.3	648.9	1.35(8)	$18^- \to 16^-$	-	-	7

E_i	E_γ	I_γ	$I_i^\pi \rightarrow I_f^\pi$	R_{AD}	A_P	$Band\#$
			Band8			
2165.6	197.3	23.6(7)	$9^- \rightarrow 8^-$	1.12(1)	-	7
2431.2	243.3	1.3(6)	$10^- \rightarrow 9^-$	0.56(11)	-	7
2431.2	265.5	7.5(3)	$10^- \rightarrow 9^-$	0.60(2)	-	8
2431.2	462.8	4.3(3)	$10^- \rightarrow 8^-$	1.41(8)	-	7
2714.5	279.4	6.60(24)	$11^- \rightarrow 10^-$	-	-	7
2714.5	283.3	3.58(14)	$11^- \rightarrow 10^-$	0.64(6)	-	8
2714.5	548.9	1.97(11)	$11^- \rightarrow 19^-$	-	-	8
3006.6	292.1	5.25(18)	$12^- \rightarrow 11^-$	0.74(10)	-	8
3006.6	571.5	2.09(11)	$12^- \rightarrow 10^-$	-	-	7
3006.6	575.4	2.61(12)	$12^- \rightarrow 10^-$	1.23(10)	-	8
3308.9	302.3	2.74(12)	$13^- \rightarrow 12^-$	-	-	8
3308.9	594.4	3.14(14)	$13^- \rightarrow 11^-$	-	-	8
3623.4	314.5	1.89(9)	$14^- \rightarrow 13^-$	1.14(10)	-	8
3623.4	616.8	1.74(10)	$14^- \rightarrow 12^-$	-	-	8
3945.8	322.4	0.87(7)	$15^- \rightarrow 14^-$	-	-	8
3945.8	636.9	1.27(11)	$15^- \rightarrow 13^-$	-	-	8
4282.3	336.5	0.53(6)	$16^- \rightarrow 15^-$	-	-	8
4282.3	658.9	2.24(10)	$16^- \rightarrow 14^-$	1.34(3)	-	8
4624.3	342.0	1.10(7)	$17^- \rightarrow 16^-$	-	-	8
4624.3	678.5	0.72(5)	$17^- \rightarrow 15^-$	-	-	8
4624.3	683.4	0.51(4)	$17^- \rightarrow 15^-$	-	-	7

Chapter 5

Discussion

In this section, the experimental characteristic features of the observed excited bands in ^{186}Os are presented. The focus is mainly on the collective structures built on the 0_1^+, 0_2^+, 2_2^+ and 4_3^+ states. Experimental information on these bands is discussed in the context of a systematic comparison with the neighboring even-even $^{182-192}$Os isotopes and in terms of γ vibrations around an axially symmetric shape, rigid triaxial rotation, and within the framework of the 5DCH-CDFT model. The 5DCH-CDFT calculations were successfully applied in the A=160 mass region, [3, 10, 54–66] and for the nuclei in the Er - Pt region [11].

5.1 Excitation energies, Routhians, and alignments of the low-energy positive-parity bands in ^{186}Os

Plots of excitation energy minus the energy of a rigid rotor, Routhians, and alignments, for the observed bands in ^{186}Os are presented in Figs 5.1 and 5.2 to show the characteristic features of the bands. A trend that is normally observed when the level energies of the excited bands are plotted as a function of spin is that the γ bands appear to have similar slope to that of their intrinsic configuration [67]. Similar slopes imply similar moments of inertia. Thus, the γ bands are expected to have moments of inertia that are similar to those of their ground-state bands. From the plots of excitation energy minus a rigid rotor shown in Fig.5.1, one can see that the observed 2^+ γ band (Band 4) appears to have a similar (although a bit smaller) slope to that of the ground-state band (Band 3). The observed 4^+ γ band (Band 5) appears to have nearly the same slope to that of the 2_2^+ band. This suggests that Bands 3, 4, and 5 of ^{186}Os have similar moments of inertia.

It should be noted that the band built on the 0_2^+ state (Band 1) has a clearly different moment of inertia compared to the moments of inertia of Bands 3, 4, and 5. The band head of Band 1 lies at a relatively high excitation energy. Its slope is less steep at low spins and becomes steeper towards high spins, and this behaviour causes it to cross Band 5.

Figures 5.2 (a) and (b) show the Routhians (energies in a rotating frame) and alignments for the observed bands in ^{186}Os. For Band 1 and yrast bands the K value of 0 is used, and for Bands 4, 5, 6, 7 and 8 the K values of 2, 4, 5, 7, and 9 are used, respectively. Harris parameters of $J_0 = 22.1\hbar^2\ MeV^{-1}$ and $J_1 = 67\hbar^4\ MeV^{-3}$ are used (obtained from Ref. [50]). These plots are helpful when studying band crossings that normally occur in many deformed nuclei as a result of an alignment of the angular momenta of the particles along the rotational axis. The band crossing that is typically observed in a number of deformed nuclei in this mass region is that of the ground-state band and the S-band. It usually occurs at around spins 10^+ - 14^+. This is where these bands interchange their nuclear properties, members of the S-band becoming the yrast states. The plots are also quite useful in assigning the configurations for the excited bands. For instance, bands involving the same j-orbital tend to have similar alignments.

The band crossing in ^{186}Os is observed. From Figs. 5.2 (a) and (b), it can be seen that the band crossing takes place at $\sim$ 310 keV, illustrated by the backbends in Fig. 5.2. This backbend is most probably due to rotation alignment involving a pair of $i_{13/2}$ neutrons.

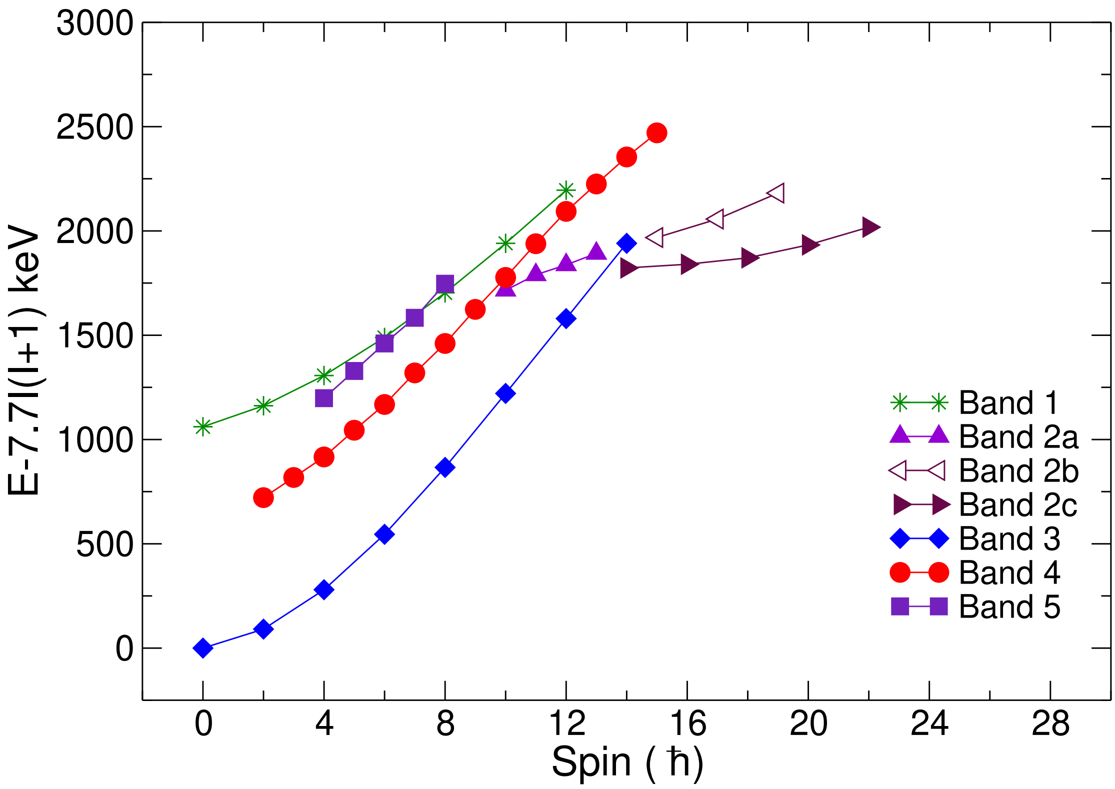

FIGURE 5.1: Plots of excitation energy minus the energy of a rigid rotor for the observed positive-parity bands in ^{186}Os.

5.2 Systematic comparison of the positive-parity bands in the $^{182-192}$Os nuclei

Focusing on the positive-parity bands built on the 0_1^+, 0_2^+, 2_2^+, and 4_3^+ states in ^{186}Os, we compare our results with those of the neighboring even-even ^{182,184,188,190,192}Os isotopes. In the $A \sim 160$ mass region, the first excited 0_2^+ and 2_2^+ bands have been extensively investigated. The experimental properties of these structures such as level energies and branching ratios have been interpreted using the 5DCH-CDFT calculations [8]. In the present work, the available experimental data in the $^{182-192}$Os isotopes are also interpreted using the 5DCH-CDFT calculations to see if the model would be successful in reproducing the experimental properties of the 0_2^+, 2_2^+, and 4_3^+ structures and reveal the underlying nature of these bands.

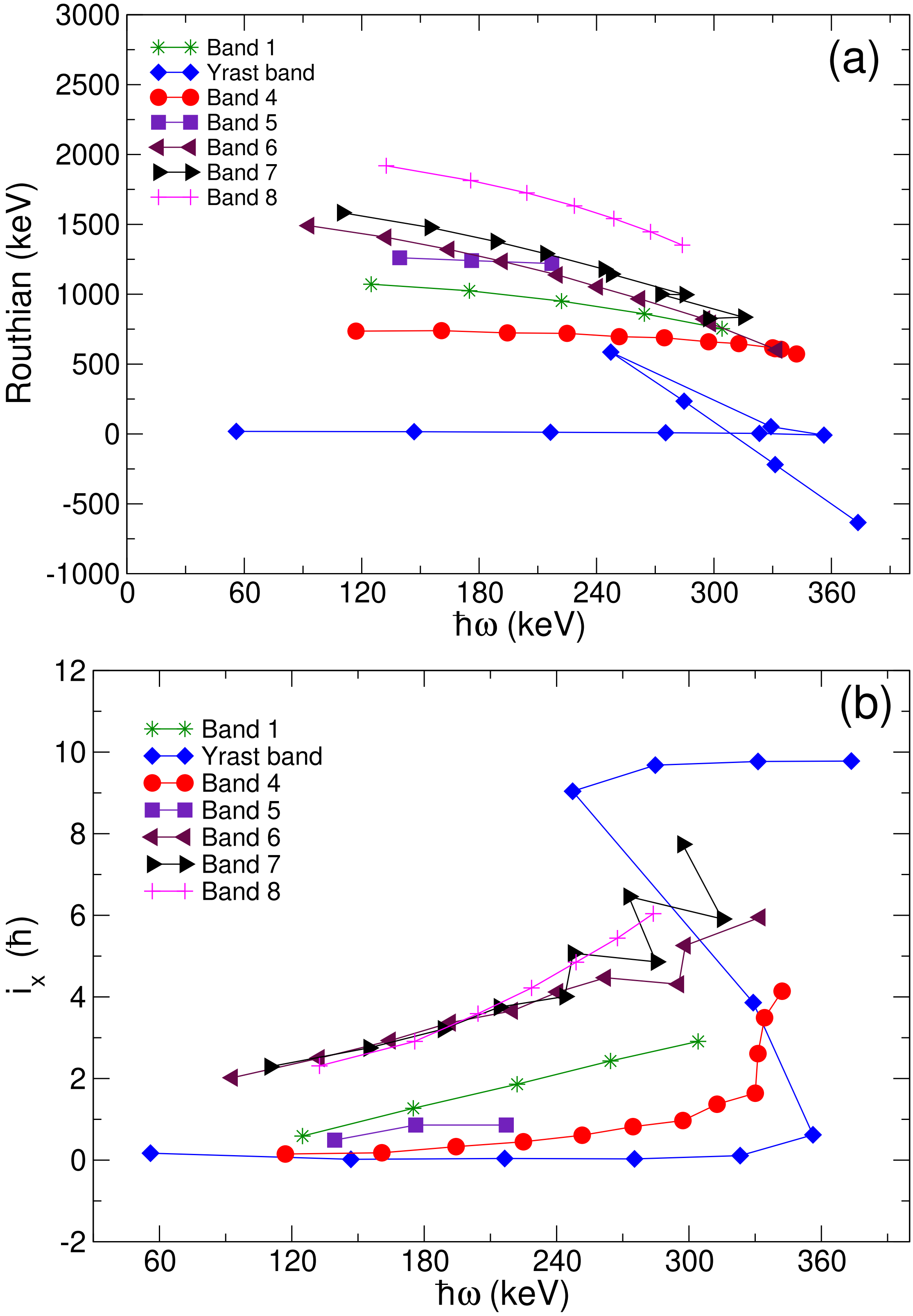

FIGURE 5.2: Experimental (a) Routhian and (b) alignment plots for the observed bands in ^{186}Os.

5.3 Excitation energies and alignments of the low-energy positive-parity bands in $^{182-192}$Os

Comprehensive systematic studies [3, 10, 57, 59, 64–66, 68–71] of the 2_2^+ bands showed that the 2_2^+ bands in the $A \sim 160$ mass region track the ground-state band up to high spin, suggesting similar moment of inertia. The studies also showed that, in some nuclei, the 0_2^+ bands mix with the even-spin members of the 2_2^+ γ band, resulting in a large energy staggering between the odd- and even-spin sequences of the 2_2^+ γ bands.

In the present work, systematic comparisons are performed for the 0_1^+, 0_2^+, 2_2^+, and 4_3^+ bands in the even-even $^{182-192}$Os isotopes. Experimental level energies for these bands are presented in Fig. 5.3. From this figure, it can be seen that the 2_2^+ bands appear to track the ground-state bands up to high spin in all the $^{182-192}$Os isotopes. The 4_3^+ bands appear to have similar slopes to those of the 2_2^+ bands, implying similar moments of inertia. From Fig. 5.3, it is worth noting that the experimental information on 4_3^+ bands in the Os nuclei is scarce. The new data in ^{186}Os is the largest extension of this band in these even-even Os isotopes.

There is also scarce experimental information for the 0_2^+ band in these nuclei, see Fig. 5.3. It is not known in the ^{182}Os and ^{188}Os nuclei, and little known in ^{184}Os, ^{190}Os and ^{192}Os. This band was established in ^{184,186}Os, and was extended in ^{186}Os in the present study.

The slopes of the excitation energy plots for the 0_2^+ bands in ^{186,190,192}Os are smaller than those of the other bands, indicating that their moments of inertia are somewhat higher, see Fig. 5.3(c), (e), and (f). The band-head energies of the 0_2^+ bands in the even-even Os isotopes appear at excitation energy of $\sim$ 900 keV, thus they lie higher than the band heads of the 2_2^+ bands.

Figure 5.4 shows the experimental alignments i_x, plotted as a function of the rotational frequency ($\hbar\omega$). They are calculated assuming $K = 0$ for the 0_1^+ and 0_2^+ bands; $K = 2$ for the 2_2^+ γ bands and $K = 4$ for the 4_3^+ bands. The alignment plots show that these bands have vanishing quasiparticle alignments. There is a little alignment gains for most bands particularly at low rotational frequency. In the region of $\hbar\omega \sim 200-350$ keV, ($I \sim$ 10), backbends develop for the ground-state bands of all even-even $^{182-192}$Os isotopes. They were interpreted as due to the rotation alignments of a pair of $i_{13/2}$ neutrons.

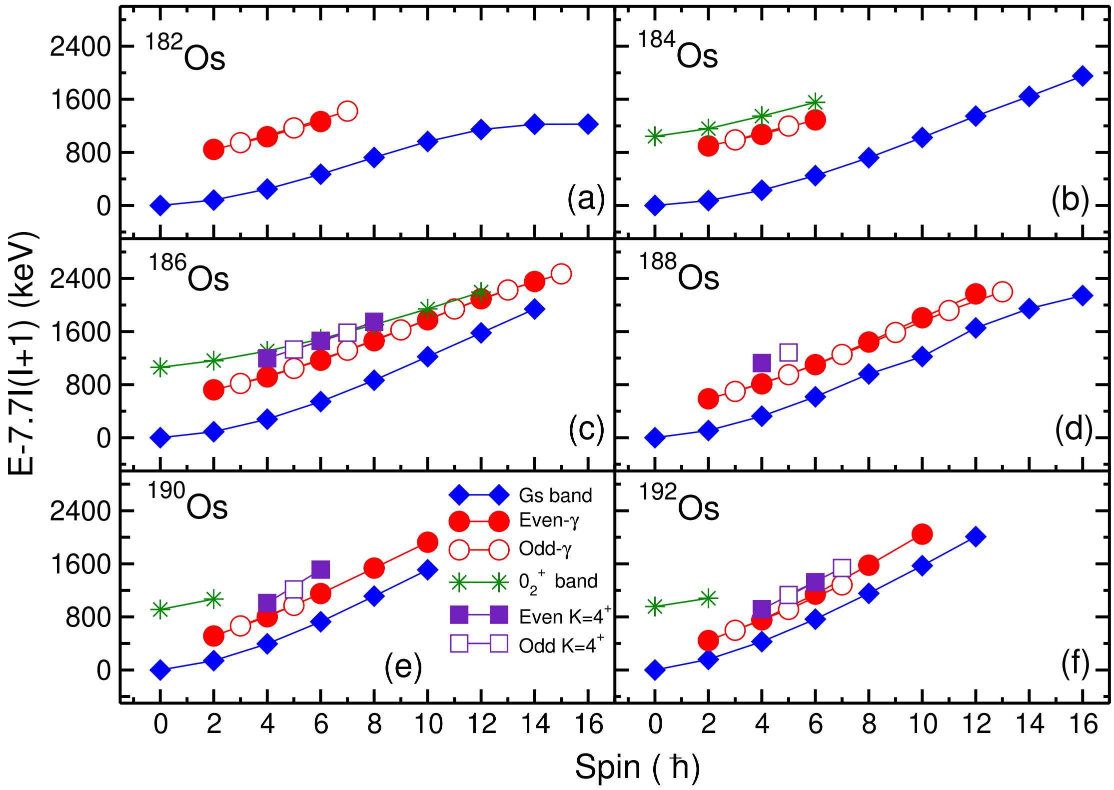

FIGURE 5.3: Experimental level energies minus the energy of a rigid rotor, plotted as a function of spin for the ground-state, 0_2^+, 2_2^+ and 4_3^+ bands in the even-even $^{182-192}$Os isotopes.

5.4 Linking transitions between the bands of ^{186}Os

Based on the observation that the deformed even-even $^{182-192}$Os isotopes have 2^+ γ bands at low excitation energies, these nuclei have been considered as one of the best regions where the γ degree of freedom plays a significant role generating low-lying positive-parity bands. A simple description based on a coupling of rotational and vibrational motions considers a deformed axially symmetric nucleus that can simultaneously rotate and vibrate. The vibrations are described by small harmonic oscillations with respect to the quadrupole deformation β and the triaxiality parameter γ. Within the adiabatic approach the rotational and vibrational degrees of freedom can be regarded as independent and the nuclear states have excitation energy of

$$E(n_\beta, n_\gamma, K, I) = A[I(I+1) - K^2] + (n_\beta + 1/2)E_\beta + (n_\gamma + 1/2)E_\gamma, \tag{5.1}$$

where n_β and n_γ are the number of excited β and γ vibrational phonons, A is the rotational parameter inversely proportional to the moment of inertia, K is the projection of the total angular momentum along the symmetry axis, and $E_\beta(E_\gamma)$ are excitation energies carried by one β (γ) phonon.

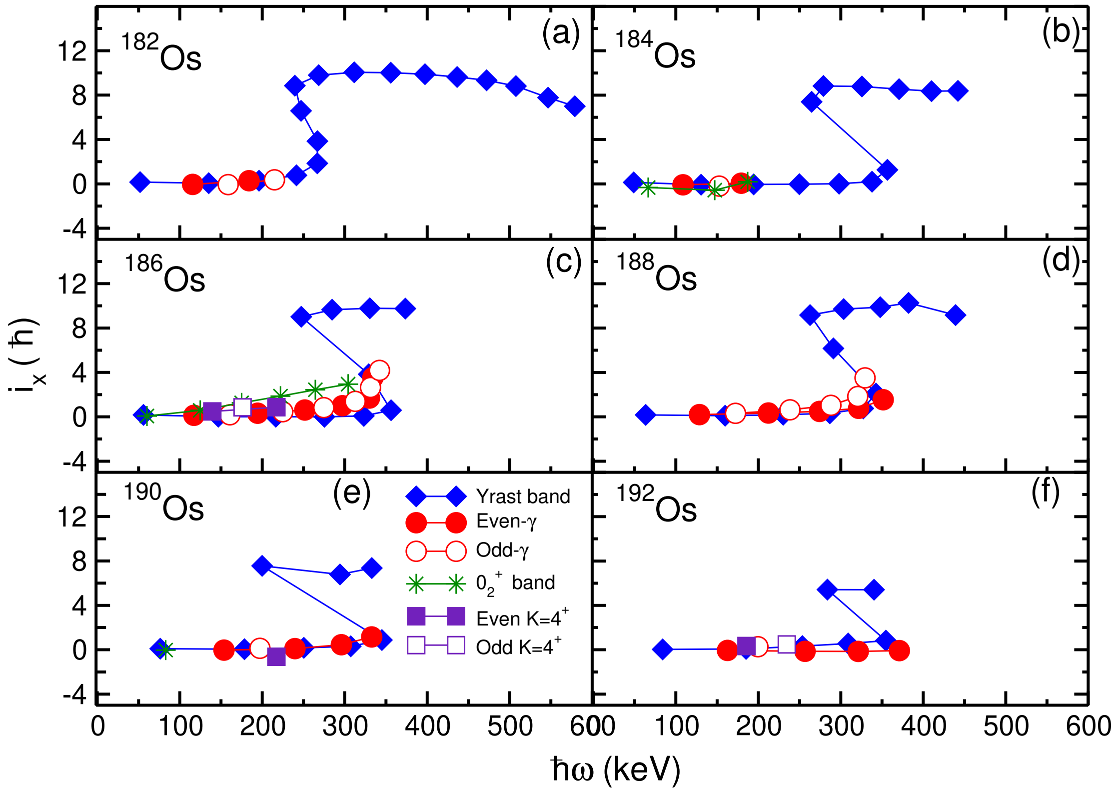

FIGURE 5.4: Experimental alignments i_x, for the ground-state, 0_2^+, 2_2^+ and 4_3^+ bands in the even-even $^{182-192}$Os isotopes.

In this interpretation the 2_2^+ γ band is produced when one γ phonon, $n_\gamma = 1$, couples with the rotation of the deformed nucleus. The 4_3^+ γ band is produced by a coupling of two γ-vibrational phonons, $n_\gamma = 2$, with the rotation of the nucleus. The energy of the 4_3^+ γ band head is twice the energy of the 2_2^+ γ band head. Each γ phonon carries angular momentum of $2\hbar$ that is aligned along the symmetry axis. Thus the projection of the total angular momentum along the symmetry axis is conserved and K = 2. The 2_2^+ and the 4_3^+ γ bands correspond to $K = 2$ and $K = 4$, respectively. For more details on this description, see Ref. [31] section 2.4.4.

This description implies several specific features of the rotational bands. For instance:
(a) The γ bands consist of even- and odd-spin sequences, and all $\Delta I = 1$ and $\Delta I = 2$ intra-band transitions in both the 2_2^+ and the 4_3^+ bands have strong $B(E2)$ reduced transition probabilities of similar magnitude to the $B(E2)$ probabilities of the intra-band transitions in the ground-state band.
(b) As K is conserved, the decays between different bands would follow the K-selection rule, that is they would be with multipole order of $L \geq \Delta K$. That implies that the ΔK = 2 decays between the 2_2^+ γ band and the ground-state band and between the 4_3^+ and the 2_2^+ γ bands can proceed through transitions with multipole order $L \geq 2$. Therefore, the $I \to I$ and the $I \to I-1$ linking transitions would be of pure unstretched $E2$ nature

(without $M1$ component). In addition the $\Delta K = 4$ decays from the 4_3^+ to the ground-state bands would be forbidden. Moreover the decays between the two-quasiparticle negative-parity bands and the two γ bands should obey the same rule, $L \geq \Delta K$.

In the present study, we examine the features of the decay scheme of ^{186}Os shown in Fig. 4.14 with respect to these expectations. The intra-band transitions in the 2_2^+ γ band are in general weak. In particular, the intra-band $\Delta I = 1$ transitions could not be observed in the present study. The branching intensities of the previously reported 143-, 161- and 216-keV transitions are restricted to below 1% [52]. Despite their very low intensity if these transitions have dominant $E2$ nature, the corresponding $B(E2)$ strength could still be of the same order of magnitude as the $B(E2)$ reduced transitions probabilities of the $\Delta I = 2$ intra-band transitions in this band.

Generally, the observed decays out of the excited bands suggest that the K-selection rule is obeyed. For instance the previously measured mixing ratios of the $\Delta I = 1$ and $\Delta I = 0$ transitions linking the 2_2^+ γ band towards the ground-state band (*e.g.* the 476-, 773-, 636-, 407-, 842-, and 622-keV transitions) correspond to almost pure unstretched $E2$ nature with an $E2$ component of more than 99% [52]. Our data revealed several new linking transitions at higher spins. The angular distribution ratio and linear polarization measurements for the $I \rightarrow I-1$ linking transitions support the assigned spins and parities, and are consistent with both almost pure stretched $M1$ or almost pure unstretched $E2$ multipolarities. Similarly the previously measured mixing ratios for the $\Delta I = 1$ and $\Delta I = 0$ transitions linking the 4_3^+ and the 2_2^+ bands of 282-, 442-, 489-keV support almost pure ($> 99\%$) unstretched $E2$ multipolarity [52]. The mixing ratios for the new higher-spin linking transitions could not be determined in this work due to low number of detectors and detection angles that were used in the experiment.

The almost pure $E2$ multipolarity for the linking transitions suggests that the K-selection rule is generally obeyed. However, some decays that are not allowed by the K-selection rule are also present. For instance (i) the decays from the 4_3^+ band head towards the ground-state band corresponding to $\Delta K = 4$; (ii) the $\Delta K = 10$ decay from the 10_2^+ band head of Band 2a toward the ground-state band. (iii) the $\Delta K = 3$ and $\Delta K = 5$ decays from the 5_1^- and 6_1^- states of Band 6 toward the 2_2^+ γ and the ground-state bands; (iv) the $\Delta K = 7$ decay from the 7_1^- band head of Band 7 to the ground-state band. These K-forbidden decays are marked with blue asterisks in the decay scheme of Fig. 4.14.

While the K-forbidden transitions are observed, their intensity is considerably reduced. For instance:
(i) The forbidden $\Delta K = 4$ decays from the 4_3^+ band head are very weak. The $B(E2)$ reduced transition probability measured in the present study for the $\Delta K = 4$ 1215-keV

transition is 8.79 $\times 10^{-4}$ times weaker than the $B(E2)$ probability for the allowed $\Delta K = 2$ 584-keV transition.
(ii) Among the $5^-_1 \rightarrow 4^+$ decays out of the $K = 5$ two-quasiparticle band, the reduced $B(E1)$ transition probability is largest for the decay to the 4^+_3 level with $K = 4$, which corresponds to $\Delta K = 1$ decay. The two other $5^-_1 \rightarrow 4^+$ decays are forbidden by the K-selection rule and their observed intensity is strongly reduced, with $B(E1, 558)/B(E1, 277) = 3.6 \times 10^{-2}$ for the $\Delta K = 3$ decay to the 2^+_2 γ band, and with $B(E1, 1195)/B(E1, 277) = 4.6 \times 10^{-5}$ for the $\Delta K = 5$ decay to the ground-state band.
(iii) The decays from the high-K bands, *e.g.* $K \geq 5$, toward the ground-state band are also generally weak. For instance the γ-ray intensities of the 903-, 906-, and 1142-keV transitions are approximately 18%, 2% and 3% of the intensities of the strongest transitions depopulating their corresponding initial levels.

To summarise, the observed features of the rotational bands provide evidence which support a description in terms of conservation of K, although it seems that allowing for some (small) K-admixtures will also be appropriate.

Nuclear states with the same spins and parities and with similar excitation energies can mix. If such states correspond to different K-values, where K is conserved, the mixing would generate admixtures in the corresponding K values. This mechanism can cause mixing in states from bands with the same parities, but it seems unclear whether it can explain all observed forbidden decays, particularly those involving states with different parities. For instance consider the $10^+_2 \rightarrow 8^+_1$ 1142-keV decay from the $K = 10$ two-quasiparticle band to the $K = 0$ ground-state band. In order to explain this $\Delta K = 10$ $E2$ forbidden decay one would assume that the 10^+ states from these two bands mix with each other. However the excitation energy gap between these two states is approximately 500 keV which seems quite large for such mixing. An alternative mechanism that generates K-admixtures can occur if the nuclear shape has non-axial deformation. Triaxial nuclei rotate and produce excited bands, for which K is only approximately conserved. Calculations in terms of triaxial rotor model (TRM) and Triaxial Project Shell Model (TPSM) have been carried out previously for the Os isotopes [2, 4]. In the following subsection we present our triaxial-rotor model calculations for ^{186}Os in order to illustrate the approximate conservation of the K-values within this model.

5.5 Triaxial-rotor model for ^{186}Os

The experimental results in ^{186}Os are interpreted using triaxial rotor model (TRM) [14, 72]. The TRM model describes the rotation of a triaxial nucleus and calculates excitation energies and wavefunctions for the states of its rotational bands. In our calculations, a nucleus was assumed to have a triaxial shape with quadrupole deformation $\epsilon_2 = 0.21$ and triaxiality $\gamma = 27°$. The moments of inertia followed an irrotational-flow trend as a function of the γ deformation, while their spin dependence was described using Harris parameters of $J_0 = 18.5\ \hbar^2 MeV^{-1}$ and $J_1 = 200\ \hbar^4 MeV^{-3}$.

In Fig. 5.5 we compare the experimental excitation energies for the ground-state and the 2_2^+ and 4_3^+ excited bands with the TRM calculations. There are two important disagreements with the experimental data, *e.g.*, the calculated relative excitation energies of the bands increase as a function of the spin, and the calculated 2_2^+ γ band shows a large energy staggering. Both of these predictions reflect general features of the triaxial rotor model. The former follows the model assumption that all rotational bands have the same moments of inertia, but the observed decrease in the experimental relative excitation energies (see Fig. 5.5 (a)) suggests that this assumption is not a good match for the ^{186}Os. A model that adopts slightly larger moments of inertia for the excited bands would be more suitable. The energy staggering in the 2_2^+ γ band is discussed in more detail in a following section.

The model describes nuclear states that correspond to approximate conservation of K where some mixture of K values is allowed. In general the triaxial rotor model interprets the rotational bands as a precession of the intermediate nuclear axis, in a similar way as a rotating top precesses around the vertical direction. The ground-state band corresponds to precession with smallest tilt with respect to the intermediate axis, because the projection of the rotational angular momentum is almost entirely along the intermediate axis, and the projection along the orthogonal axes (short or long axis) is $K = 0$, see Fig. 5.5 (c). The 2_2^+ and 4_3^+ γ bands correspond to gradual increase of the tilt of the precessing rotational angular momentum, labelled as $R_{K=2}$ and $R_{K=4}$, respectively. These bands correspond to projections of $K = 2$ and $K = 4$ on the orthogonal axes.

This schematic description of the $3D$ rotation of a triaxial nucleus is valid near the band heads of these bands, where K is approximately conserved, while at higher spins the mixing becomes important. To show this mixing we have examined the wave functions of the states of the three bands, see Fig. 5.6.

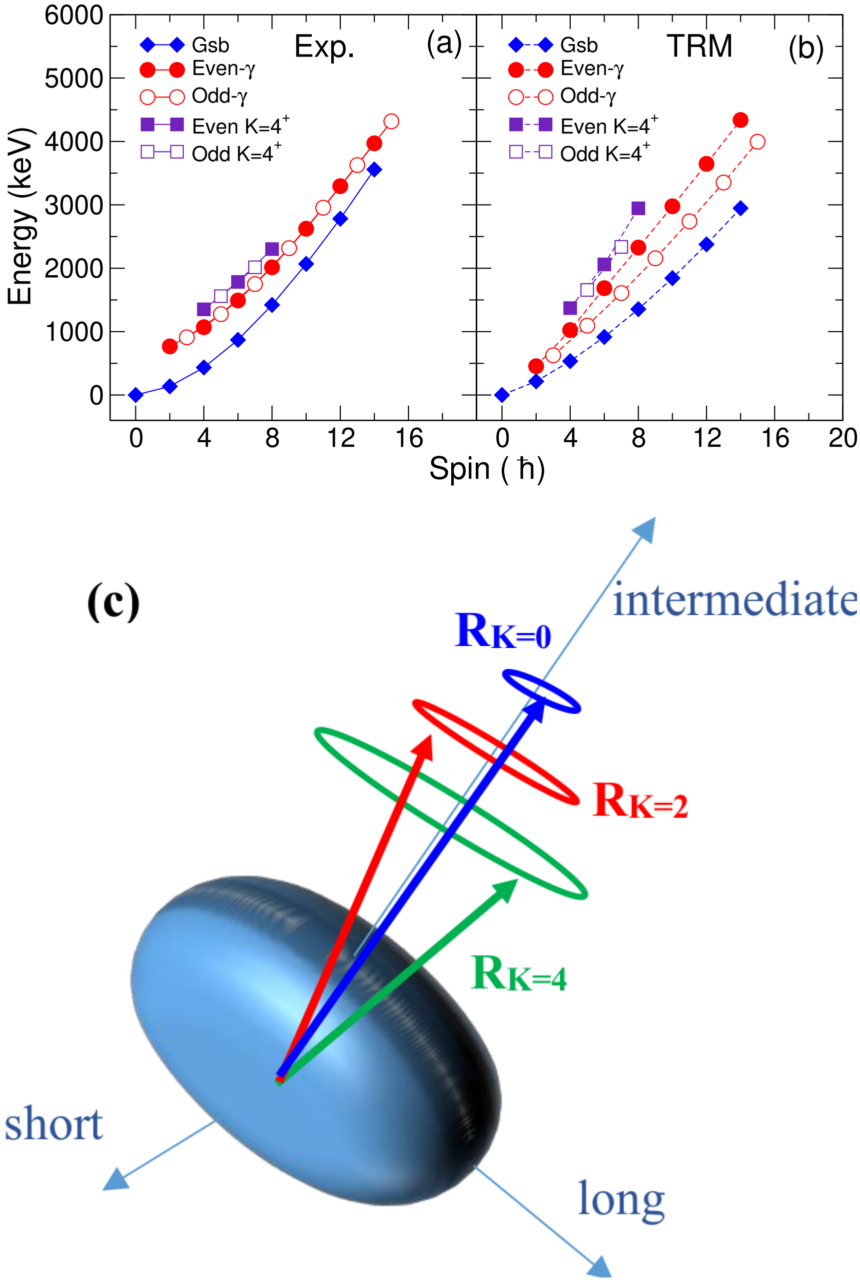

FIGURE 5.5: Excitation energies for the ground-state, 2_2^+ and 4_3^+ γ bands in ^{186}Os, obtained from (a) experimental data and (b) the TRM calculations. The rotation of a triaxial nucleus resembles the precession of a rotating top, with the rotational angular momentum R precessing around the intermediate nuclear axis, as illustrated in panel (c). The favoured rotation is around the intermediate axis, unfavored rotations around an orthogonal axis (long and short nuclear axes) generates a tilt of the total rotational angular momentum, i.e $R_{K=2}$, $R_{K=4}$.

The calculated wave functions of the states from the ground-state band are shown in Fig. 5.6(a). For each state with spin I the contributions of components with different values of K (where the rotational angular momentum is projected along the long axis) are represented by columns with different colors. For instance the wave function of the 2_1^+ state indicates that it is almost exclusively (more than 80%) associated with a component with $K = 0$, (see the blue column). Therefore the rotation is almost fully aligned along the intermediate axis. This component is dominant for the states of the ground-state band at low spins, supporting the approximate description of the ground-state states at low spins as $K = 0$ states. Similarly, the wave functions of the low-spin states of the 2_2^+ γ band correspond to dominant $K = 2$ contributions (the brown columns) in Fig. 5.6(b) and thus the precession around the intermediate axis with larger tilt than that for the ground-state band, (see the sketch in Fig. 5.5). Note the staggering pattern of this contribution for even- and odd-spin states, where the odd-spin members correspond to wave functions with larger $K = 2$ and $K = 4$ components, while the even-spin members have largest contributions with $K = 0$ and $K = 4$. This different nature is probably responsible for the predicted energy staggering. Similarly, the calculated low-spin states from the 4_3^+ band are associated with dominant $K = 4$ contributions (the grey columns) in Fig. 5.6(c) and thus correspond to precession around the intermediate axis at a larger angle, see Fig. 5.5.

Contrary to these well-defined dominant types of precession with $K = 0$, 2 and 4 for the ground-state, 2_2^+ and 4_3^+ bands, respectively, the high-spins states in these bands have large contributions from components with various K values.

This behaviour highlights an important difference between the interpretations of these bands in terms of (i) small vibrations around an axially symmetric shape, which preserves K, and assigns $K = 0$, $K = 2$, and $K = 4$ to the ground-state, 2_2^+ and 4_3^+ γ bands, respectively, and (ii) triaxial rotor, where K is approximately good near the band-heads and becomes strongly mixed at higher spins. Therefore within the former description the transitions linking bands with $\Delta K = 2$, (such as the 2_2^+ γ band and the ground-state band, or the 4_3^+ and 2_2^+ bands) should correspond to $L \geq \Delta K$ (therefore pure $E2$ character) both near the band heads and at high spins as K is conserved. In contrast to that the latter description allows for this requirement to be somewhat weaker near the band heads, due to the approximate nature of the K conservation at low spins, while at high spins, where the states correspond to a mixture of various K values, the K-selection rule might not be obeyed. Therefore it is interesting to study the experimental data and test whether the linking transitions between the positive-parity bands correspond to pure $E2$ nature including up to high spins, in line with a description within γ vibrations around an axially symmetric shape, or whether the linking transitions at high spins show a mixed $M1 + E2$ mulitpolarity, which would indicate that K is not well conserved and the nuclear shape might acquire some rigid triaxiality. Our measurements could not provide precise measurements of the mixing ratios of the linking transitions, but such study can be carried out in the future with the upgraded AFRODITE array at iThemba LABS. In the following section results from the 5DCH-CDFT calculations are discussed.

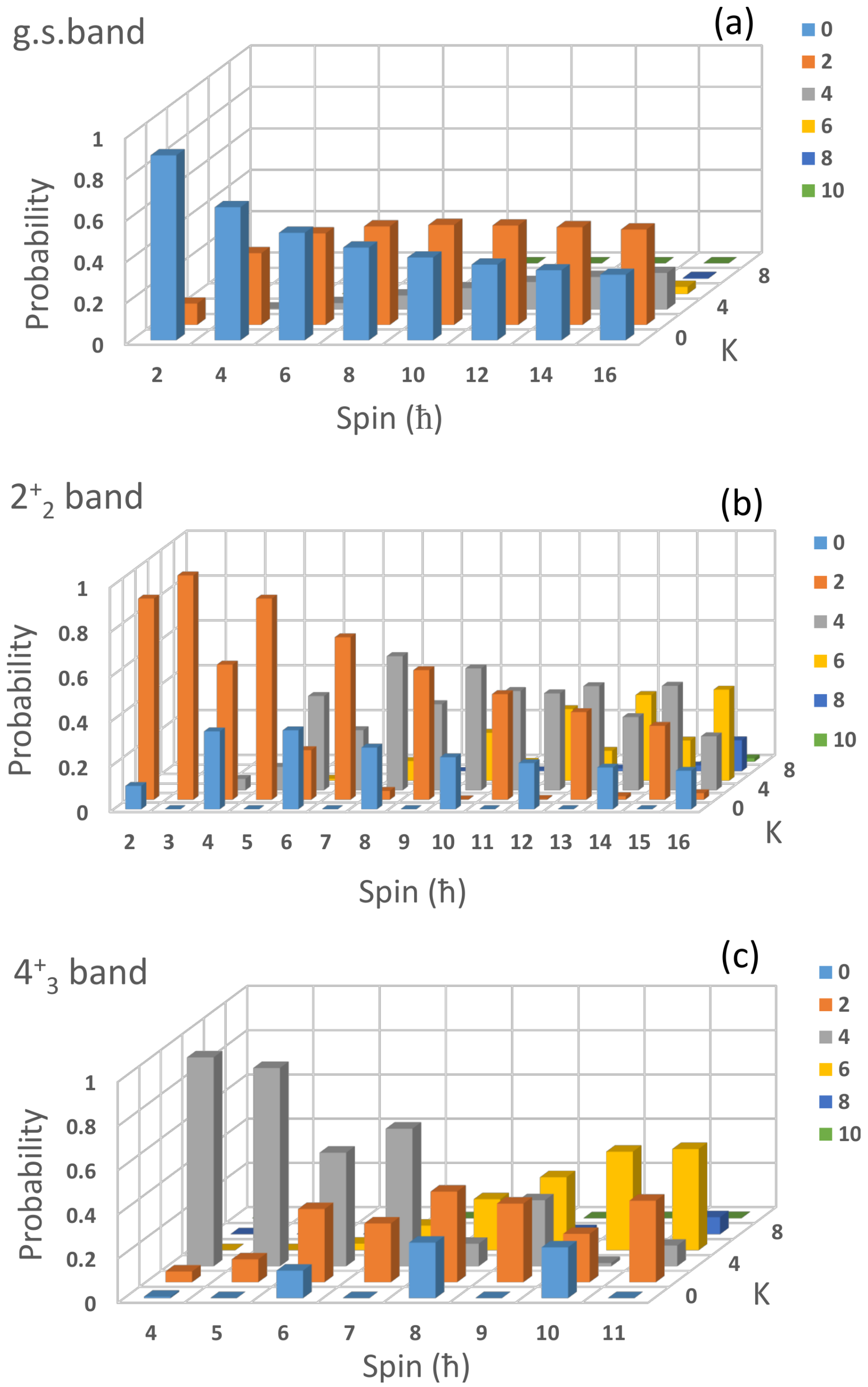

FIGURE 5.6: The probability distributions of the wave functions for the states with spin I of the (a) ground-state (b) 2_2^+, and (c) 4_3^+ bands. The wave functions are projected on the long axis. The values of K are shown on the y-axis, and are also illustrated with different colours as listed in the legends.

5.6 Comparison with the 5DCH-CDFT calculations

The Os isotopes lie in a transitional region where the nuclear shape changes from spherical to a well deformed shape. Thus, a model that has the potential to consider both

γ vibrations and rigid triaxial rotations would be most interesting for these isotopes. Recently, systematic calculations within the framework of the 5DCH-CDFT model were published for the nuclei in the Er - Pt region [11]. The 5DCH-CDFT model [8, 9] is a modern form of Bohr Hamiltonian, which has been extended to allow large magnitude vibrations both in terms of β and γ in combination with a rotation of a nucleus with a deformed shape. Therefore the model can simultaneously treat the vibrational and the rotational excitations of a triaxial or axially symmetric nucleus. The low-lying excitations of deformed nuclei can be described using a collective Hamiltonian with deformation-dependent parameters - β, γ, and three Euler angles $\Omega \equiv (\phi, \theta, \psi)$ defining the orientation of the intrinsic principal axes in the laboratory frame. The collective Hamiltonian is defined as follows:

$$\hat{H}_{coll}(\beta, \gamma) = \hat{T}_{vib}(\beta, \gamma) + \hat{T}_{rot}(\beta, \gamma, \Omega) + V_{coll}(\beta, \gamma), \tag{5.2}$$

where $\hat{T}_{vib}(\beta, \gamma)$ is the vibrational kinetic energy, $\hat{T}_{rot}(\beta, \gamma, \Omega)$ is the rotational kinetic energy and $V_{coll}(\beta, \gamma)$ is the collective potential. The diagonalization of this collective Hamiltonian produces the properties of the low-lying states in deformed nuclei. More details of the three terms of the equation can be found in Ref. [8, 9].

The collective parameters are self-consistently determined by the microscopic CDFT calculations. In these calculations, the relativistic point-coupling energy functional PC-PK1 and the separable pairing force are respectively adopted in the particle-hole particle-particle channels. Solving the Dirac equation is achieved by expanding the Dirac spinor in terms of the three-dimensional harmonic oscillator basis with 16 major shells. The triaxial mean-field states with deformation parameters $\beta \in [0.0, 0.8]$ and $\gamma \in [0°, 60°]$ and steps $\beta = 0.05$, $\gamma = 6°$ are generated by imposing the parity D2 symmetry and time-reversal invariance in the quadrupole deformation constrained relativistic mean-field plus BCS calculation.

5.6.1 Potential energy surfaces

Potential energy surfaces (PESs), calculated using the 5DCH-CDFT, of the even-even $^{182-192}$Os isotopes in the (β, γ) plane are shown in Fig. 5.7. The PESs are plotted for quadrupole, β, and γ deformation parameters. In this figure, nuclei have the lowest energy in the bluest part of the plots, global minima being indicated by red dots. From these plots one can see that the global minima for the ground states of the ^{182,184,186}Os isotopes are located at $\beta \sim 0.3$ and $\gamma \sim 0°$. The ^{182,184}Os isotopes have axially symmetric shapes, with a very small softness with respect to γ deformation. The PES minimum for ^{186}Os corresponds to a less-deformed prolate symmetric shape, consistent with the experimentally observed decrease of the moment of inertia of the ground state rotational band. The ^{188}Os isotope has an axially symmetric shape, with larger softness with respect to γ. The global minima for the ^{190,192}Os isotopes are at $\beta \sim 0.2$ and $\gamma \sim 25°$. Thus, the calculations predict that the ground states of the Os isotopes are evolving towards triaxiality as the neutron number increases.

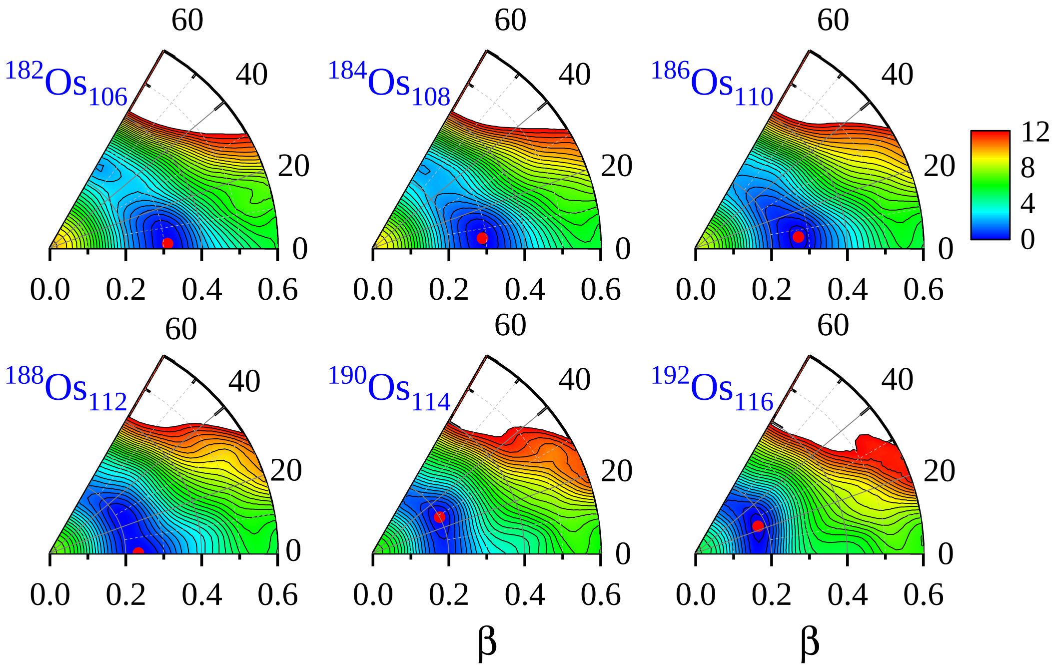

FIGURE 5.7: Potential energy surfaces (PESs) of the even-even $^{182-192}$Os isotopes in the (β, γ) plane. Minima are marked with red circles. The energy difference between neighboring contours is 0.5 MeV.

5.6.2 Probability density distributions

One of the advantages of the 5DCH-CDFT model is that it can calculate the probability density distribution for each state of the positive-parity bands. Thus, the PES were used to calculate the wave functions for the 0_1^+, 0_2^+ and 2_2^+ states, and the states of the 4_3^+ band in ^{186}Os. The calculations shown in Fig. 5.8 for the 0_1^+, 0_2^+ and 2_2^+ states indicate that the 0_1^+ and 0_2^+ states correspond to an axially symmetric shape, but the 0_1^+ state exhibits a larger softness with respect to β and γ. The band-head of the 0_2^+ band is associated with a very narrow distribution, which seems not compatible with β vibrations. It is worth noting that the predicted quadrupole deformation for this band head is slightly larger than the deformation for the ground state. This suggests that the excited 0_2^+ band is probably due to a shape co-existence. The predicted larger deformation is supported by the experimental data showing that the 0_2^+ band has a larger moment of inertia than the ground-state band, see Fig. 5.1. While the calculations favor axially-symmetric shape for the ground-state and the 0_2^+ bands, the prediction for the 2_2^+ band indicates a well-pronounced triaxiality with $\gamma \sim 15°$.

Calculations carried out for the 4_3^+, 5_2^+, 6_3^+, and 7_2^+ states of the 4_3^+ band are presented in Fig. 5.9. The wave functions of the 5_2^+ and 7_2^+ states predict a well-defined triaxial maximum at $\gamma \sim 25°$. The distributions indicate moderate softness with respect to β and γ. This softness is smaller than the predicted softness of the ground state. The probability distributions for the 4_3^+ and 6_3^+ states correspond to a maximum at near axially symmetric prolate shape, however the wave functions suggest considerable softness with respect to the γ degree of freedom. These predictions suggest that the even- and odd-spin members of the 4_3^+ band have different nature.

The predicted nature of the 4_3^+ state is, in particular, very similar to the γ-unstable Wilets-Jean model, where the potential is almost independent of γ and oscillations between prolate and oblate deformation occur. The even-spin states, therefore, can be associated with large-magnitude γ-vibrations coupled to rotation, while the odd-spin states, associated with well-defined triaxial shape seem more likely to exhibit a three-dimensional rigid rotation.

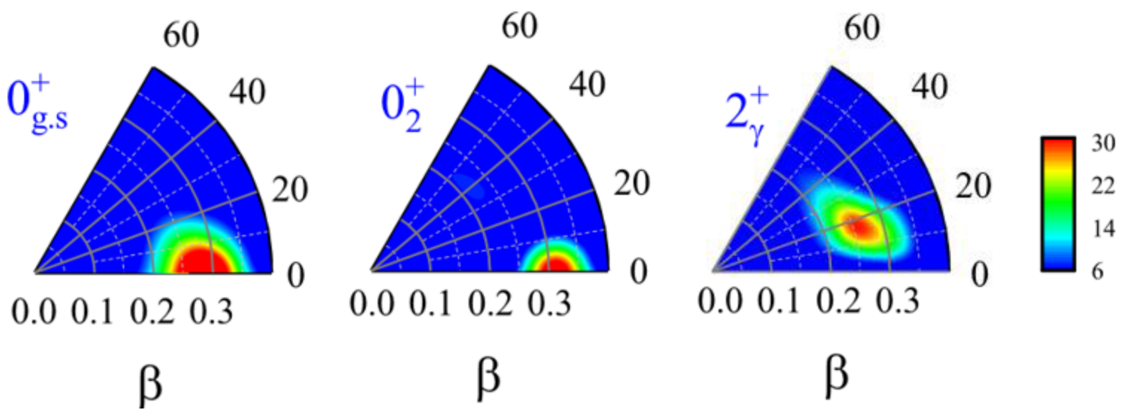

FIGURE 5.8: Probability density distributions calculated in the (β, γ) plane for the 0_1^+, 0_2^+, and 2_2^+ states of ^{186}Os.

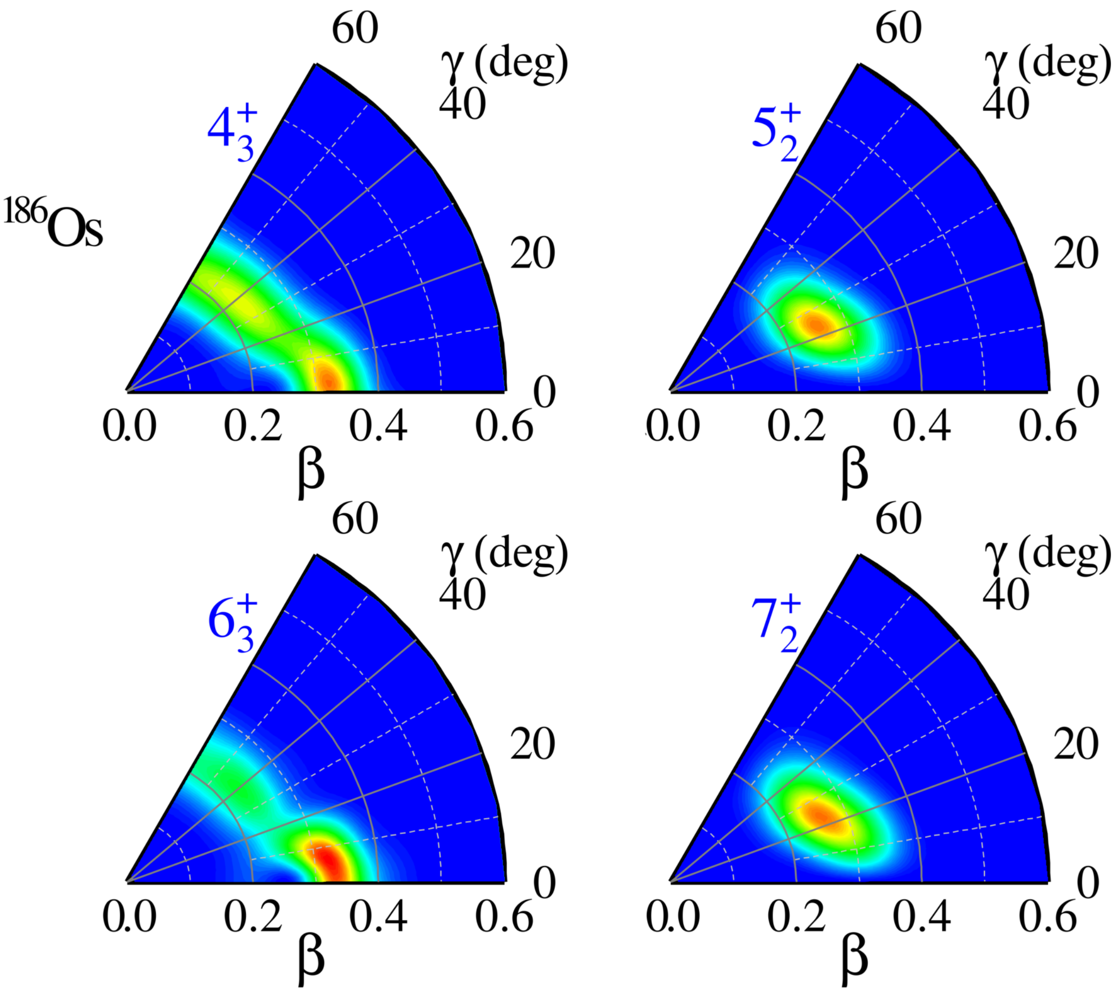

FIGURE 5.9: Probability density distributions in the (β, γ) plane for the 4_3^+, 5_2^+, 6_3^+, and 7_2^+ states of the 4_3^+ band in ^{186}Os.

5.6.3 Level energies

Figure 5.10 shows the experimental level energies for the 0_1^+, 0_2^+, 2_2^+ and excited 4_3^+ bands in the even-even $^{182-192}$Os isotopes in comparison with the 5DCH-CDFT calculations. There is in general an agreement between the calculations and the experimental data. In particular the relative excitation energies of the 2_2^+ γ band heads are very well reproduced. The general behavior of the 0_1^+, 2_2^+, and 4_3^+ bands observed in the $A \sim 160$ mass region was well reproduced by the 5DCH-CDFT model. The excitation energies of the 0_2^+ and the 4_3^+ band heads in the Os isotopes are a bit overestimated. However, the model correctly predicts that the band-head energies of the 0_2^+ bands lie higher than the band-head energies of the 2_2^+ bands. Generally, there is a good agreement between the calculations and the experimental data particularly at low spins. At high spins it seems the calculated energies overestimate the experimental data.

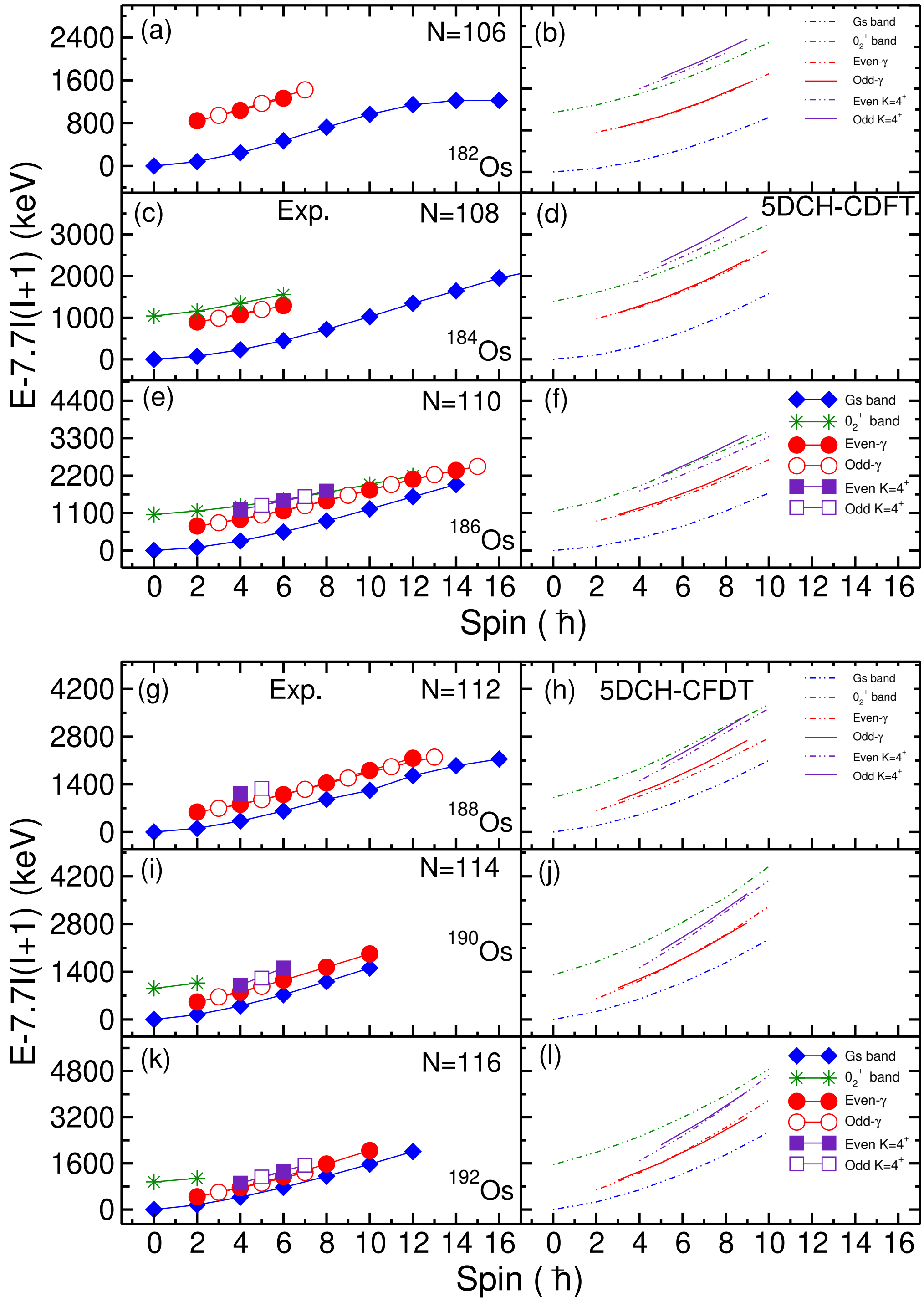

FIGURE 5.10: Experimental level energies for the ground-state, 0_2^+, 2_2^+ and 4_3^+ bands in the even-even $^{182-192}$Os isotopes, compared with the predictions by 5DCH-CDFT.

5.6.4 Energy staggering

Energy staggering 5DCH-CDFT calculations were carried out for the 2_2^+ γ bands in the even-even $^{182-192}$Os isotopes. The experimental and calculated staggering parameters $S(I)$ for the 2_2^+ γ bands are shown in Fig. 5.11. The model predicts the energy staggering well, particularly for the ^{182,184,190}Os isotopes, see Figs. 5.11 (a, b, e) but overestimates the staggering in ^{186,188}Os. The staggering for the 2_2^+ and 4_3^+ bands in ^{186}Os is discussed in more detail in a following section.

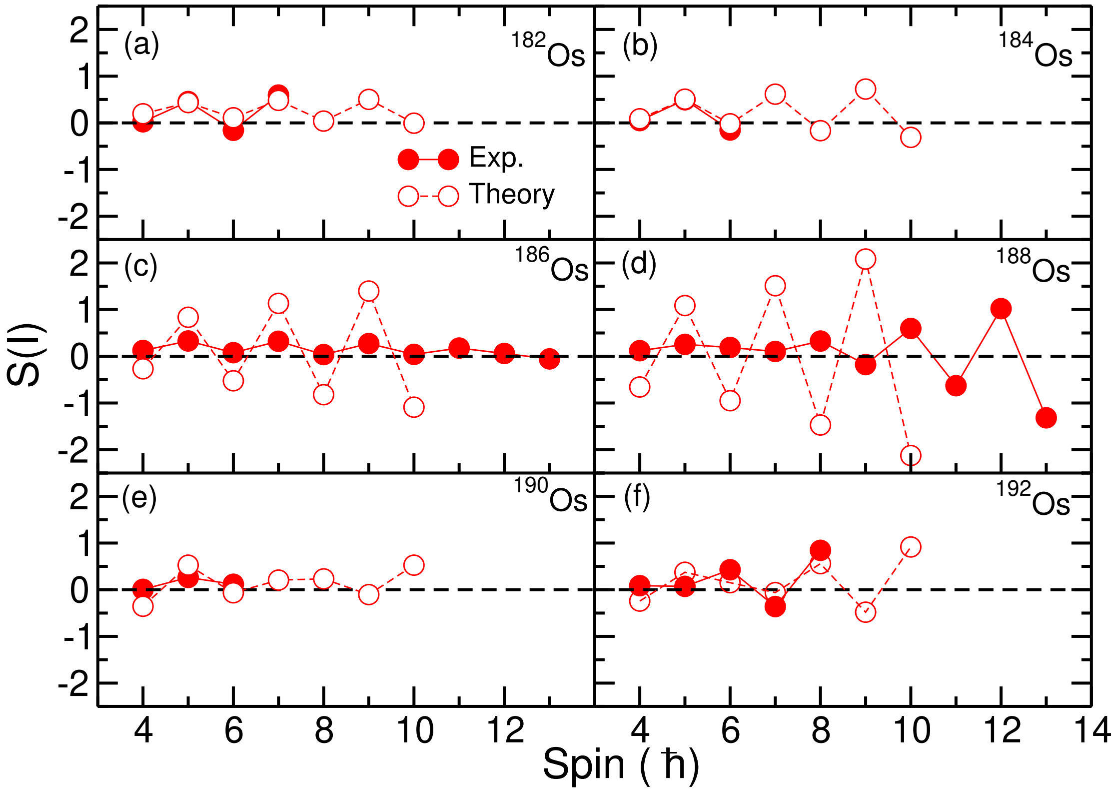

FIGURE 5.11: Experimental staggering parameter $S(I)$, plotted as a function of spin for the γ bands in the even-even $^{182-192}$Os isotopes, in comparison with the 5DCH-CDFT calculations.

5.6.5 Band-head energies and $R_{4^+/2^+}$ ratios

A systematic comparison of the energy ratios of the first excited 4_1^+ and 2_1^+ states, and the band-head energies of the 0_2^+, 2_2^+ and 4_3^+ bands in the $^{182-192}$Os isotopes were carried out. The calculated and experimental energy ratios $R_{4^+/2^+} = E(4_1^+)/E(2_1^+)$, plotted as a function of spin, are presented in Fig. 5.12 (a). From this figure one can see that both the experimental data and the 5DCH-CDFT calculations indicate that the ratios $R_{4^+/2^+}$ decrease for the $^{184-192}$Os isotopes. Decreasing energy ratios suggest that the quadrupole deformation is decreasing. The PES calculations discussed above also predict that the deformation decreases with increasing mass. It should be noted that the 5DCH-CFDT calculations overestimate the energy ratio for the lighter isotope (A=182), and underestimate it for the heavier ones (A=188, 190, and 192).

Figure 5.12 (b) shows the experimental data and the calculated band-head energies of the 0_2^+, 2_2^+ and 4_3^+ bands in the even-even $^{182-192}$Os isotopes. The experimental data

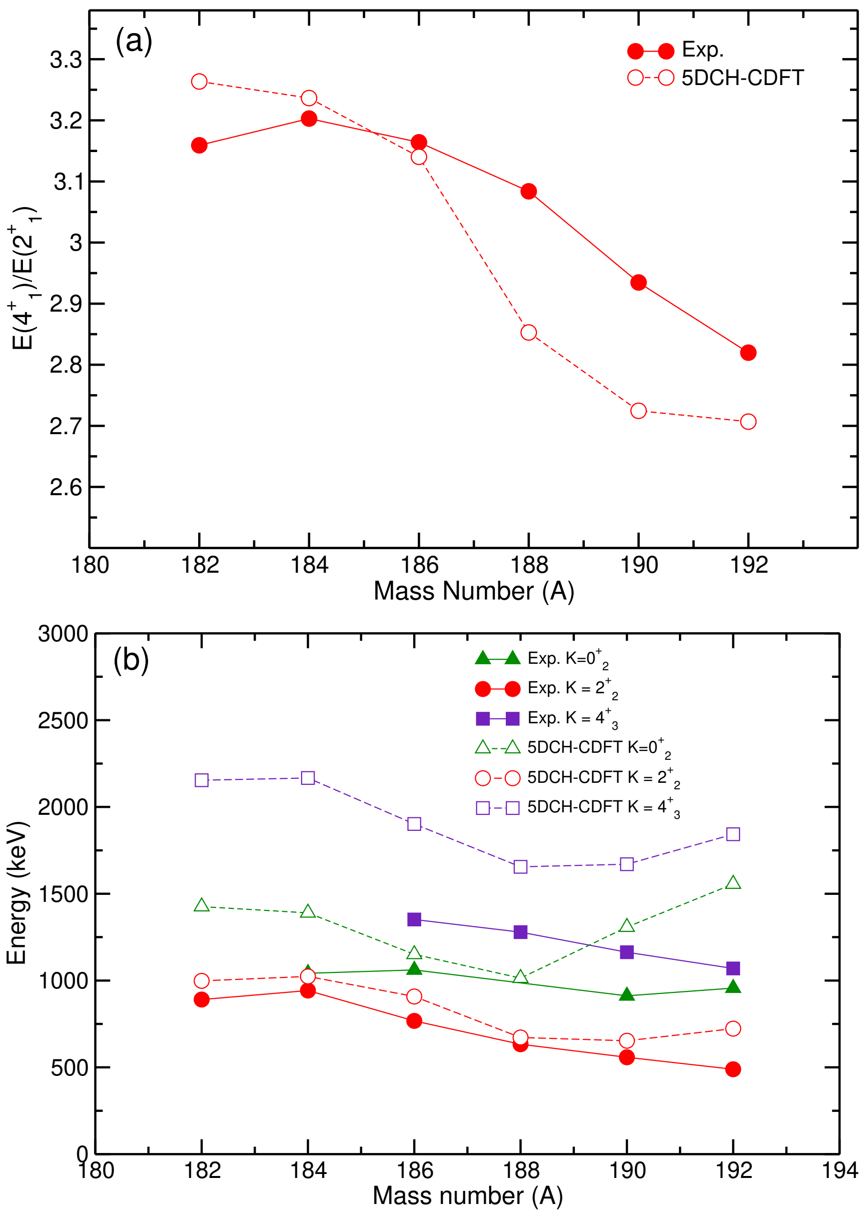

FIGURE 5.12: Shows the (a) experimental energy ratios (solid line) of the first excited 4_1^+ and 2_1^+ states and the (b) band-head energies (solid lines) of the 0_2^+ , 2_2^+ and 4_3^+ bands in the even-even $^{182-192}$Os isotopes, in comparison with the 5DCH-CDFT calculations (dotted line).

shows that the excitation energies for the 2_2^+ and 4_3^+ states decrease gradually with increasing mass number, while those of the 0_2^+ state are almost constant. The 5DCH-CDFT model gives a good description for the 2_2^+ band-heads energies. The 0_2^+ and 4_3^+ band-head energies are overestimated by the model.

5.6.6 $B(E2)$ reduced transition probability

Figures 5.13, 5.14, and 5.15 show a systematic comparison between the experimental and calculated $B(E2)$ reduced transition probability ratios for the first excited 0_2^+ and 2_2^+ bands in the even-even $^{182-192}$Os isotopes. The experimental $B(E2)$ ratios for the out-of-band (decaying to the ground-state bands) to the in-band transitions are compared with the 5DCH-CDFT calculations.

It can be seen in Fig. 5.13 that the $B(E2: I_{0_2^+} \rightarrow I_g)/B(E2: I_{0_2^+} \rightarrow (I-2)_{0_2^+})$ ratios have only been measured for three Os isotopes, see Figs. 5.13 (b), (c), and (e). An impressive agreement between the experiment and theory is observed in the ^{186}Os and ^{190}Os isotopes. In ^{184}Os, the experimental ratio at spin 6^+ does not agree well with the calculations.

In Fig. 5.14, the theory underestimates the $B(E2: I_\gamma \rightarrow I_g)/B(E2: I_\gamma \rightarrow (I-2)_\gamma)$ branching ratios for the even-spin members of the 2_2^+ bands in some Os isotopes, see Figs. 5.14 (c), (e), and (d). It is worth noting that in Fig. 5.14 (e) the measured ratios decrease with the increase in spin, as predicted by the 5DCH-CDFT.

The $B(E2: I_\gamma \rightarrow (I-2)_g)/B(E2: I_\gamma \rightarrow (I-2)_\gamma)$ branching ratios for both the even- and odd-spin members of the 2_2^+ bands in the even-even $^{182-192}$Os isotopes are presented in Fig. 5.15. It is seen that in Fig. 5.15 (c) both the experimental and theoretical branching ratios for the odd-spin members of the 2_2^+ band are higher than those of the even-spin members of the 2_2^+ band. In other isotopes presented in Fig. 5.15, the theory agrees well with the experimental data.

Generally, the agreement between the experimental data and calculated $B(E2)$ ratios in the even-even $^{182-192}$Os isotopes is good.

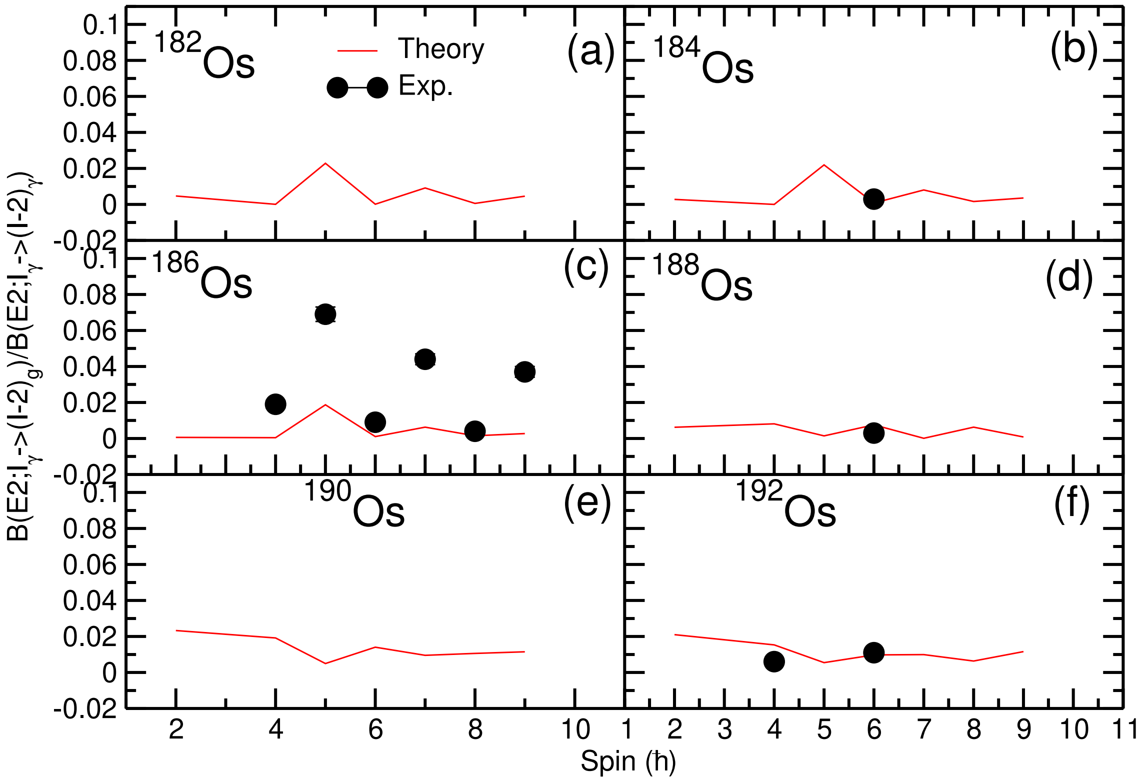

FIGURE 5.13: Experimental branching ratios for out-of-band to in-band transitions $B(E2 : I_{0_2^+} \to I_g)/B(E2 : I_{0_2^+} \to (I-2)_{0_2^+})$, for the first excited 0_2^+ bands in the even-even $^{182-192}$Os isotopes, in comparison with the 5DCH-CDFT calculations.

5.6.7 Energy staggering for the 2_2^+ and 4_3^+ γ bands in ^{186}Os

Energy staggering S(I) is considered as one of the important quantities that provides information on the nature of the bands [73, 74]. In an attempt to better understand the nature of the observed 2_2^+ and 4_3^+ bands in ^{186}Os, we examine the energy staggering and compare the results with the predictions by γ vibration, γ unstable, 5DCH-CDFT, and triaxial rotor models. The energy staggering $S(I)$ is defined as

$$S(I) = \frac{[E(I) - E(I-1)] - [E(I-1) - E(I-2)]}{E(2_1^+)}, \tag{5.3}$$

where $E(I), E(I-1)$, and $E(I-2)$ represent the energies of the states at spins $I, I-1$, and $I-2$, respectively, and $E(2_1^+)$ is the energy of the first excited 2^+ state.

In Fig. 5.16, the experimental levels for the ground-state and 2_2^+ bands in ^{186}Os, and the energy staggering $S(I)$ for the 2_2^+ band are presented. The experimental levels are compared with some simple theoretical calculations shown in Fig. 5.17 [74], and with 5DCH-CDFT. The experimental energy staggering compared with different calculations is shown in Fig. 5.18.

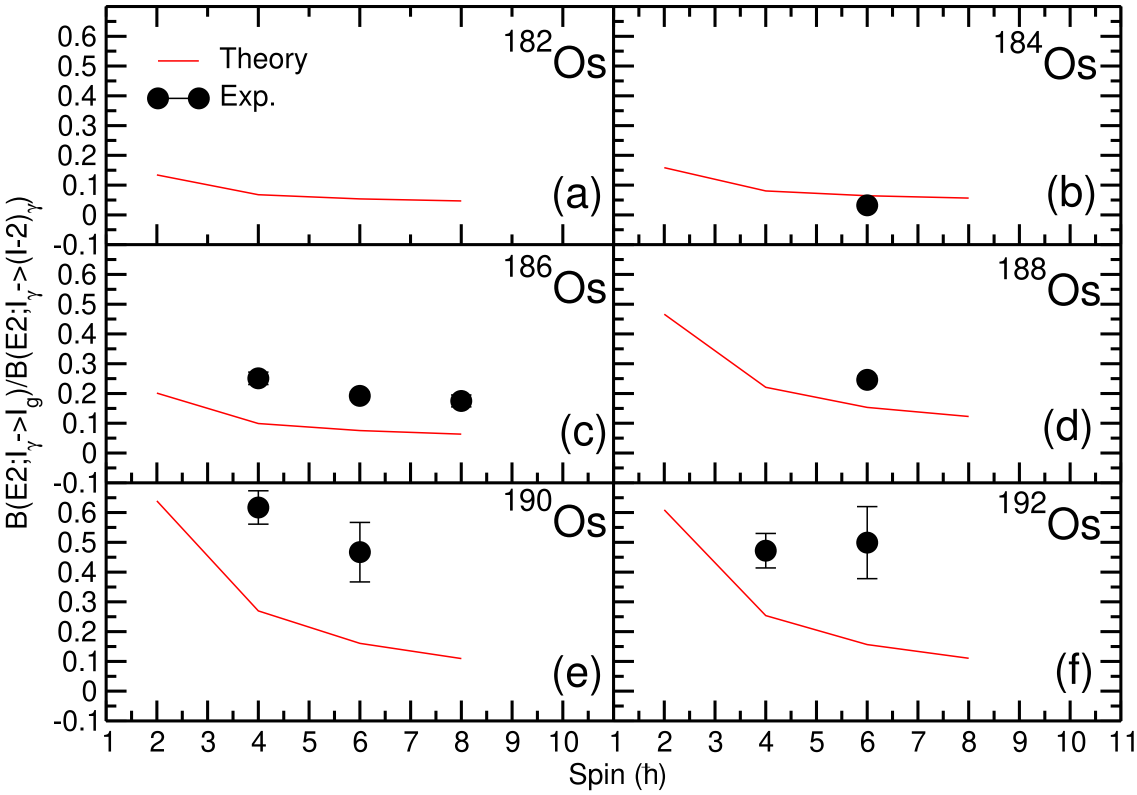

FIGURE 5.14: Experimental branching ratios for out-of-band to in-band transitions $B(E2 : I_\gamma \rightarrow I_g)/B(E2 : I_\gamma \rightarrow (I-2)_\gamma)$, for the even-spin members of the 2_2^+ bands in the even-even $^{182-192}$Os isotopes, in comparison with the 5DCH-CDFT calculations.

The staggering $S(I)$ has different behaviour and different magnitude depending on the nature of the γ band. For instance a γ band described as large-magnitude γ vibrations within the γ-unstable model of Wilets-Jean exhibits large staggering that increases with spin for both the 2_2^+ and 4_3^+ bands, see Fig. 5.18. The magnitudes of the staggering calculated within this model well exceed the experimental observations.

The triaxial rotor model also produces a 2_2^+ γ band with large and increasing staggering, in disagreement with the magnitude and phase of the experimental data. On the other hand the staggering predicted by the TRM model for the 4_3^+ band is in very good agreement with the experimental data. The 5DCH-CDFT model reproduces the phase of the staggering in the 2_2^+ band, although the magnitude is overestimated. The staggering predicted by this model for the 4_3^+ band is too large. The magnitude of the experimentally observed staggering in both bands is, in fact, best reproduced by a simple vibrational-rotational model, where the 2_2^+ and 4_3^+ bands are caused by one and two γ-vibrational phonons coupled to the rotation of an axially symmetric nucleus.

Generally, the vibrational description looks quite promising, because in addition to successfully describing the staggering $S(I)$, it necessitates a stringent K-selection rule, which (based on the available data), is generally obeyed. However, this simple model is not able to describe all features of the 2_2^+ and 4_3^+ bands. In fact the observation

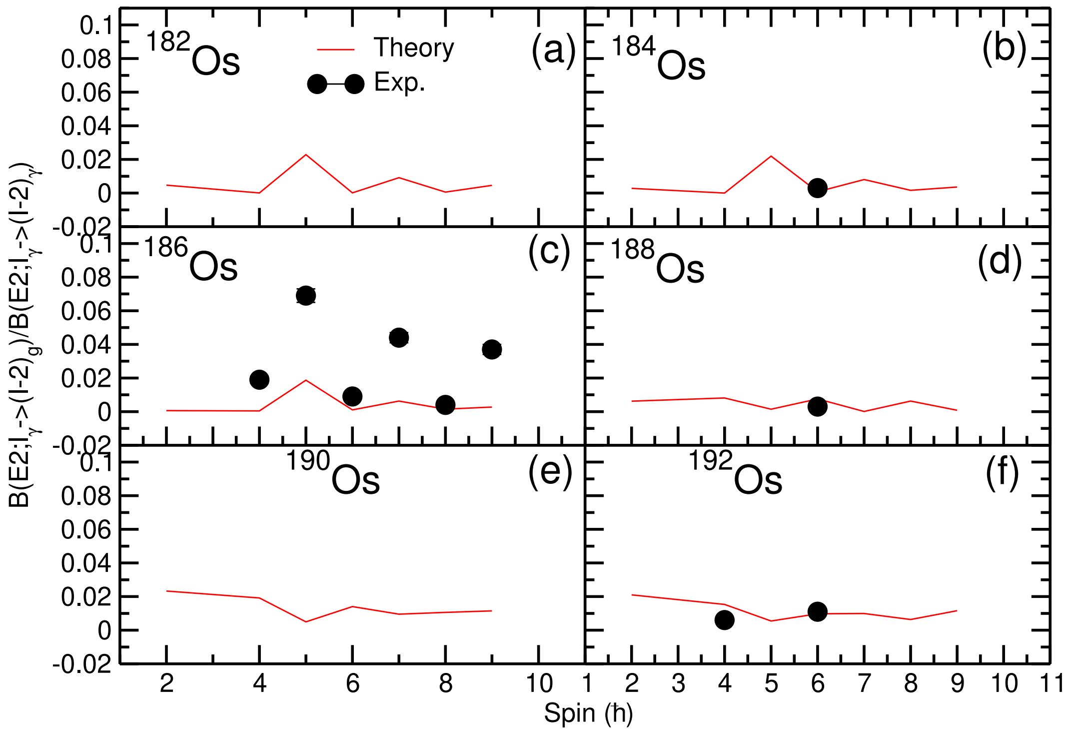

FIGURE 5.15: Experimental branching ratios for out-of-band to in-band transitions $B(E2 : I_\gamma \to (I-2)_g)/B(E2 : I_\gamma \to (I-2)_\gamma)$, for both the even- and odd-spin members of the 2_2^+ bands in the even-even $^{182-192}$Os isotopes, in comparison with the 5DCH-CDFT calculations.

of a number of K-forbidden transitions implies that a mechanism that generates K-admixtures (for instance triaxiality of the nuclear shape) is very probable. Furthermore, the 5DCH-CDFT model predicted well-defined triaxiality for the 2_2^+ band and for the odd-spin members of the 4_3^+ band, and γ-softness for the even-spin members of this band. In addition, the 4_3^+ band is probably not entirely due to a collective excitation but involves significant single-particle contributions, as suggested by experiments on transfer reactions [6, 7]. Further experimental and theoretical studies in the Os nuclei are needed to reveal more details on the nature of the low-spin positive-parity bands. It seems that examining further the K-selection rule through precise measurements of the mixing ratios of transitions related to the 2_2^+ and 4_3^+ bands can shed more light on the nature of these bands.

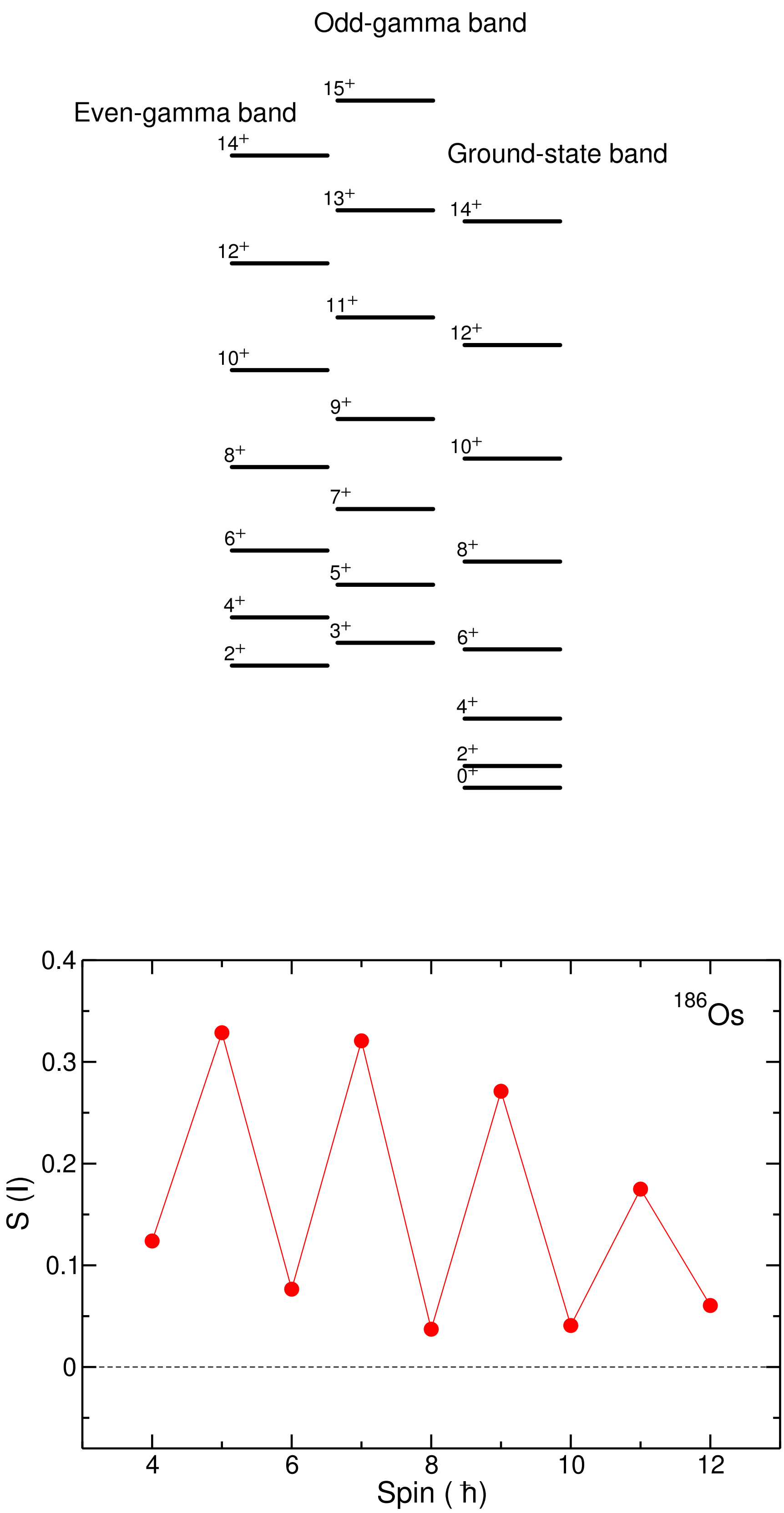

FIGURE 5.16: The experimental level energies for the ground-state and 2_2^+ bands in ^{186}Os (top), and experimental staggering parameters $S(I)$ plotted as a function of spins (bottom).

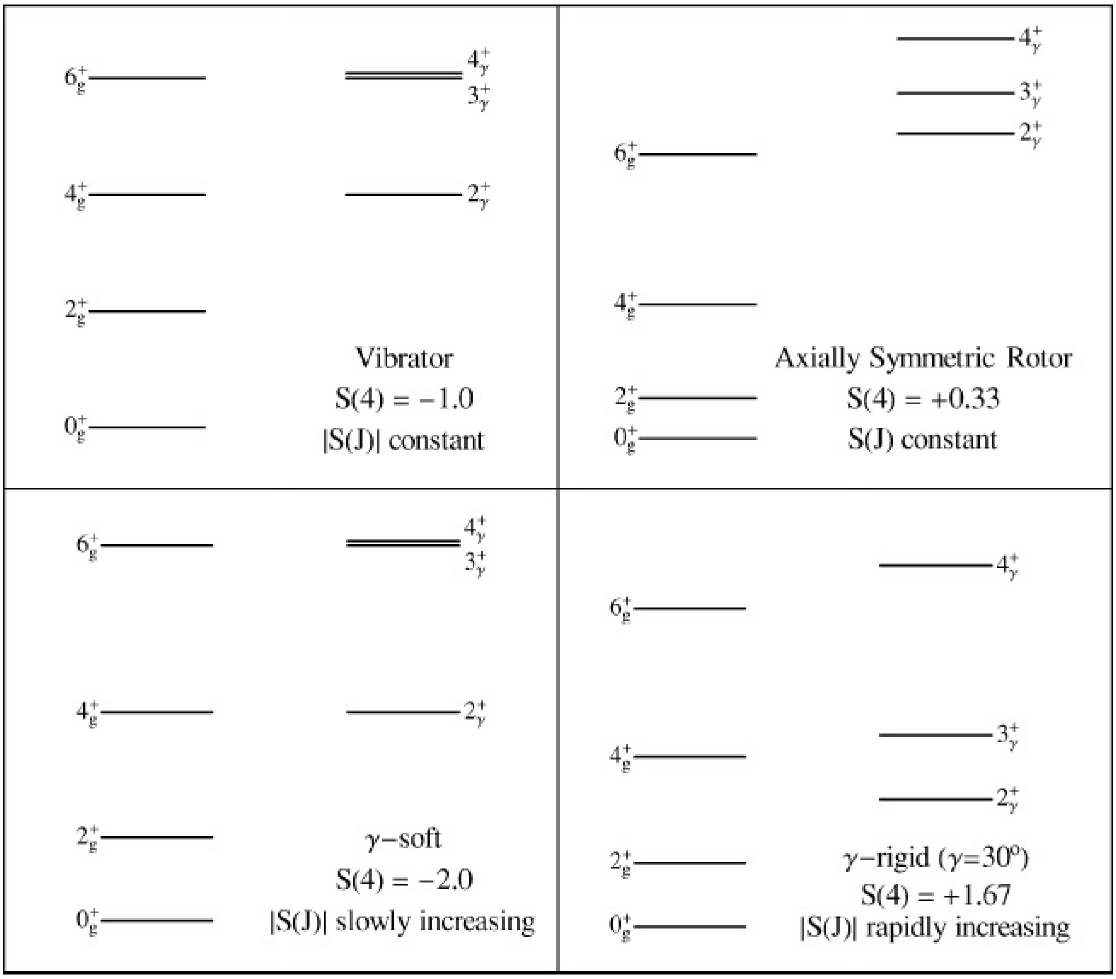

FIGURE 5.17: Comparison of the level spacings of the ground-state and 2_2^+ γ bands for a vibrator, axially symmetric rotor, γ-unstable and γ-rigid structures.

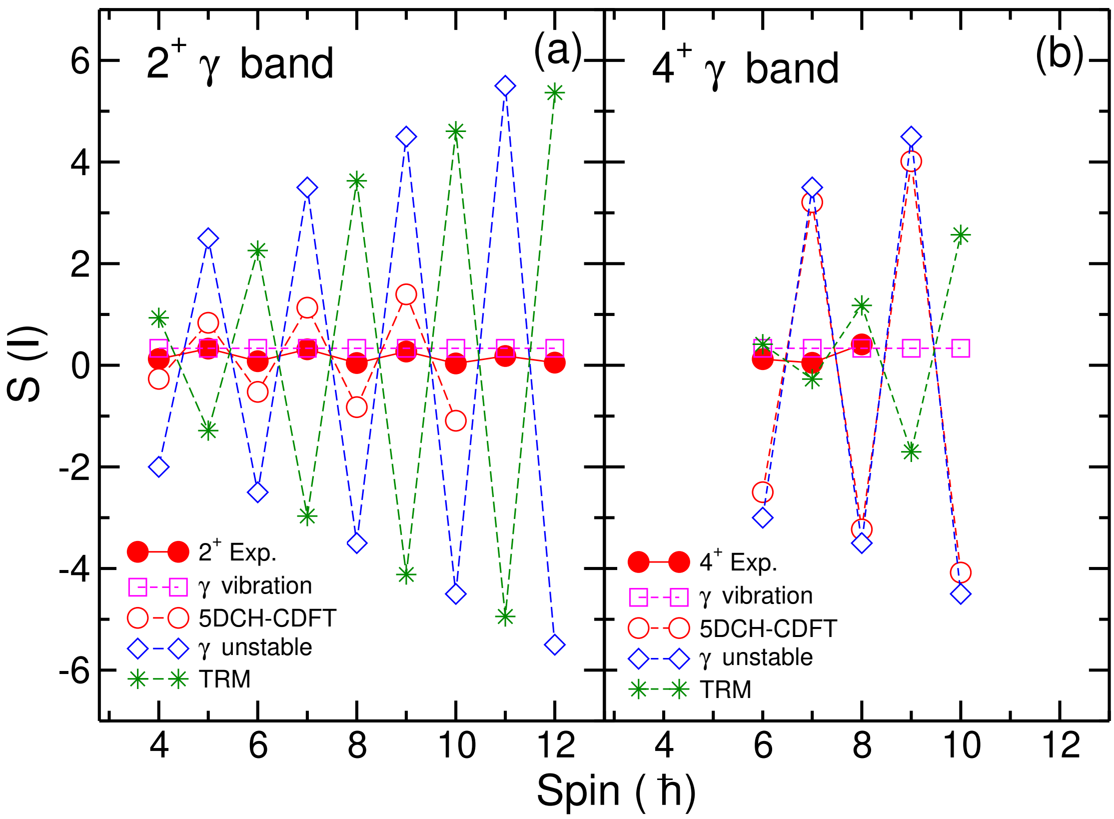

FIGURE 5.18: Experimental staggering parameter $S(I)$ for the (a) 2^+_2 and (b) 4^+_3 bands in ^{186}Os, in comparison with the γ-vibrational, 5DCH-CDFT, γ- unstable, and TRM calculations.

Chapter 6

Conclusion

The excited bands in ^{186}Os have been investigated at iThemba LABS through the ^{186}W(^{4}He, 4n)^{186}Os reaction. A decay scheme of this nucleus has been improved by adding 21 new γ-ray transitions. New experimental information on the 0_2^+, 2_2^+ and 4_3^+ structures was obtained. In particular, the 0_2^+, 2_2^+ and 4_3^+ bands have been extended up to spins of 12^+, 15^+, and 8^+, and several new linking transitions were identified. Spin-parity assignments were made on the new levels based on angular distribution and linear polarization measurements. The collective bands in ^{186}Os were interpreted in the context of a systematic comparison with the neighboring even-even $^{182-192}$Os isotopes and in terms of small harmonic γ vibrations around axially symmetric shape, three-dimensional rotation of a triaxial nucleus, and within the 5DCH-CDFT model. The validity of the K-selection rule was examined and it was found that the features of the observed bands support a compliance with the rule, although some K-forbidden decays were also observed implying small K admixtures. The 5DCH-CDFT calculations provide a detailed description of the positive-parity bands in ^{186}Os, in agreement with the experimental data. The calculations assign a variety of different shapes to these bands, including axially symmetric to the 0_1^+ and 0_2^+ bands, and triaxial to the 2_2^+ and 4_3^+ bands.

One of the main objectives of this research work was to try to understand the underlying nature of the collective 2_2^+ and 4_3^+ bands in the Os isotopes, that is, distinguishing between the possible rigid-triaxial shape and γ vibration. However, the present work could not distinguish between these possible interpretations. Further investigations carried out with a larger detector array allowing for more measuring angles and better linear polarization sensitivity would be very useful. In particular, mixing ratios of the transitions decaying out of the collective 2_2^+ and 4_3^+ bands can reveal information on their underlying nature. In the present study mixing ratios could not be determined due to the low number of detectors (11) and detection angles (2) of the AFRODITE array. However, with the upgraded AFRODITE array which now has 17 detectors and 7 detection angles, precise measurements of the mixing ratios can be determined.

Appendix A

Structures in ^{150}Gd

A.1 Background and motivation

While the investigations of the collective structures in ^{186}Os were the prime focus of this work a brief γ spectroscopy study of ^{150}Gd was also carried out. The ^{150}Gd nucleus has 64 protons and 86 neutrons. The neutron number represents only four neutrons above the $N = 82$ shell gap and this significantly affects the structure of the excited states in ^{150}Gd. While the $N = 82$ and $N = 84$ Gd isotopes of ^{146,148}Gd have spherical shape [75] and exhibit low-spin excitations with dominant single-particle nature, and the $N > 88$ Gd isotopes are deformed and exhibit rotational bands, the N= 86 ^{150}Gd is a transitional nucleus, where the observed low-spin states have a complex nature [76]. The low-spin states in the N = 86 − 90 Gd isotopes are shown in Fig. A.1. The ground-state bands in the heavier Gd isotopes represent typical rotation of a deformed nuclear shape, see Fig. A.1 (c) while the negative parity band for these nuclei is understood as a coupling of an octupole phonon with the rotation of the deformed nucleus, see Fig. A.1 (d). In addition the 0^+_2 and 2^+_2 bands are observed, see Fig. A.1 (b) and (a), respectively. They can be interpreted as possible β- and γ-vibrational bands, or alternatively they might be caused by shape coexistence and or triaxial deformation. Contrary to this the positive-parity sequence of states in the spherical ^{146,148}Gd nuclei, see Fig. A.1 (c), represent single-particle excitations within the $f_{7/2}$ sub-shell. They exhibit the typical for such excitations decrease in the γ-ray energy as a function of spin. The interpretation of the negative-parity states in Fig. A.1 (d) as coupling of an octupole phonon with the positive-parity states is confirmed by the observation of several collective $E3$ transitions with $B(E2) \sim 60$ W.u. linking the negative- and positive-parity states [75–77].

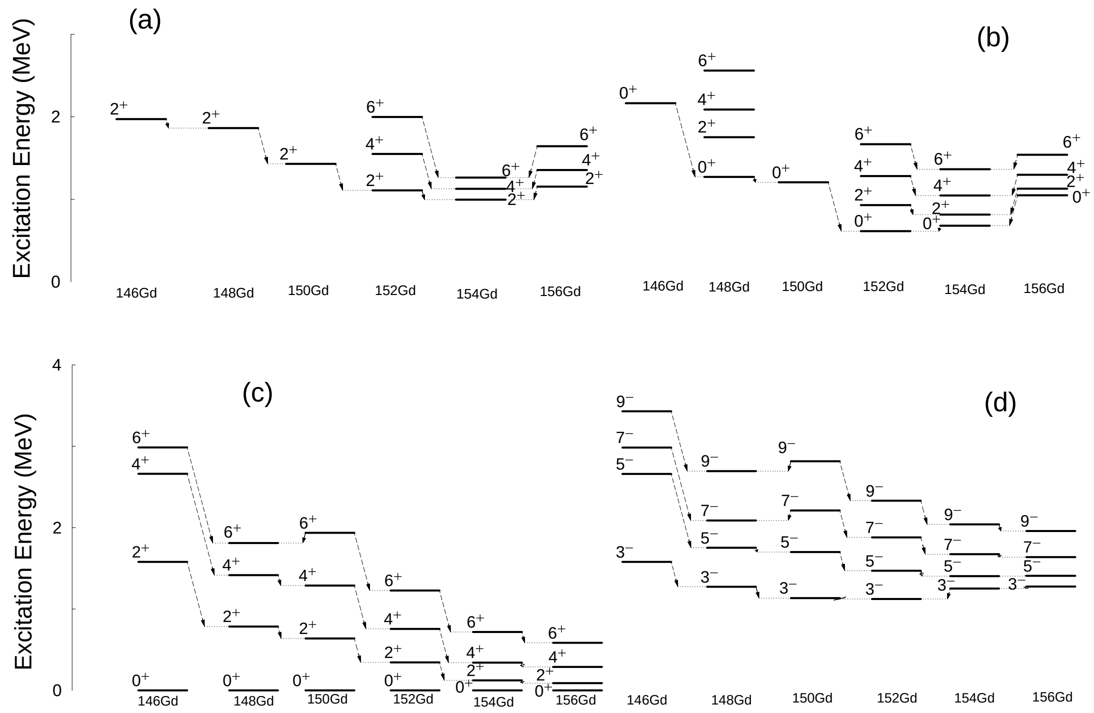

FIGURE A.1: The low-spin states in the even-even $^{146-156}$Gd isotopes.

The interpretation of ^{150}Gd is the most challenging because it represents a transition between spherical and deformed nuclear shapes. It shows irregular γ-ray energies linking the positive-parity states, see Fig. A.1 (c), but they are neither with constantly increasing γ-ray energy (as in a deformed nucleus) nor with a consistently decreasing γ-ray energy (as in spherical nucleus with single-particle excitations). The experimental information on the normal deformed states in ^{150}Gd is in general limited, as no studies have been carried out since 1985. A level scheme of the known states is shown in Fig. A.2.

To understand the observed states several different theoretical approaches were proposed. For instance the observed states can be considered as caused by single-particle excitations. In this case the states are associated typically with single-particle excitations in the neutron $f_{7/2}$, $h_{9/2}$ and $i_{13/2}$ shells, while the negative-parity states result from an additional coupling with an octupole phonon as shown in Fig. A.2. Alternatively, the low-spin states can be generated by excitations of quadrupole and octupole phonons. For instance Fig. A.3 (a) shows calculations where the positive-parity states are associated with excitations of quadrupole phonons [77]. A general feature of this interpretation is that the first 2^+ state corresponds to one-phonon vibration, while there is a triplet of states with spins of 2_2^+, 0_2^+ and 4_1^+ at very similar excitation energies associated with an excitation of two quadrupole phonons. This interpretation requires specific quantization in the excitation energies and $B(E2)$ transition probabilities for

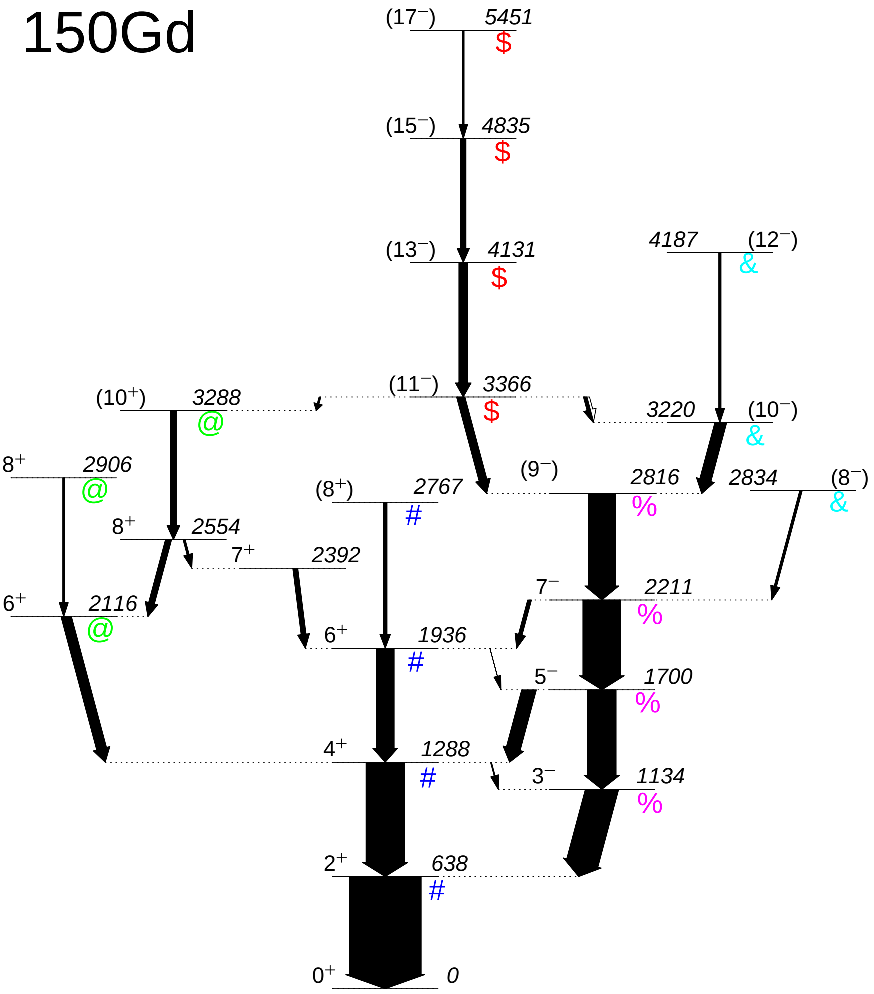

Figure A.2: A level scheme of the known states in ^{150}Gd within a simple-particle approach. States that correspond to single-particle excitations within the $(f_{7/2})^2$ or $(f_{7/2})^4$ shell are marked with the hash symbol (#). The states shown with percentage sign (%) are coupling of an octupole phonon with the $(f_{7/2})^2$ or $(f_{7/2})^4$ single-particle excitations of the positive-parity states. The single-particle excitations of $(h_{9/2}f_{7/2})$ or $(h_{9/2}{f_{7/2}}^3)$ type are shown with asperands (@). The single-particle excitations of $(h_{9/2}i_{13/2})$ type are marked with ampersands (&). The coupling of an octupole excitation with single-particle excitations of $(h_{9/2}{f_{7/2}}^3)$ states are indicated with the dollar sign $ [75].

instance the excitation energy of the triplet of states should be about twice the energy of the 2_1^+ state.

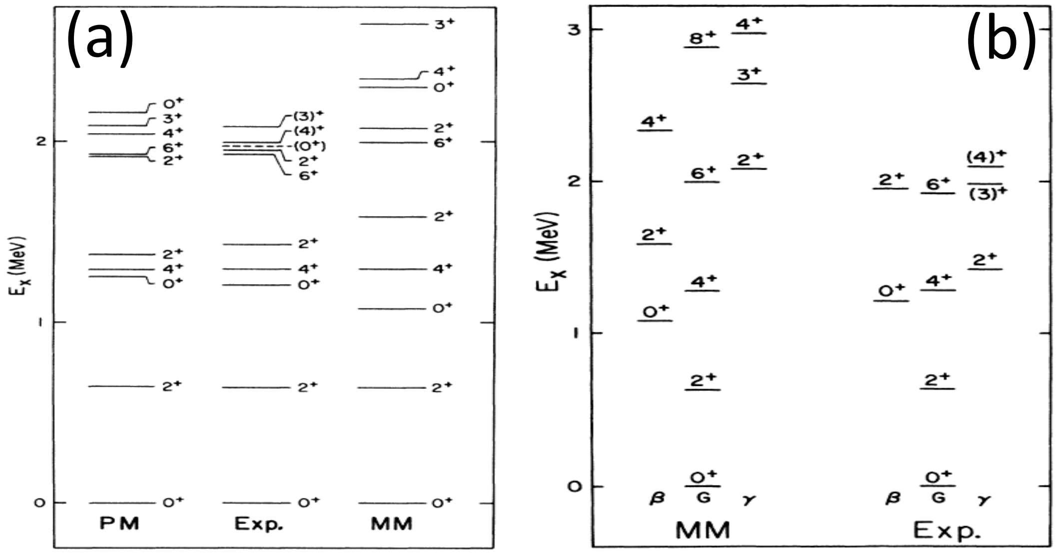

FIGURE A.3: Calculations for the positive-parity states in ^{150}Gd assuming that they are caused by (a) excitations of quadrupole phonons and (b) by nuclear rotations, generating quasi-ground-state band, 0_2^+ β band, and 2_2^+ γ band [77].

In an alternative approach the low-spin states in ^{150}Gd were associated with quasi-rotational behaviour. Within this interpretation the ground-state band would represent the rotation of a nucleus with small deformation. Excited β and γ bands are also expected resulting from the coupling of the rotation with β and γ vibrations. Such calculations for ^{150}Gd are shown in Fig. A.3 (b). These three theoretical interpretations are based on very different assumptions about the underlying excitation mechanism. In order to evaluate the nature of the low-spin excited states in ^{150}Gd more experimental information is needed. For instance a rotational behaviour can be confirmed by a clear observation of the excited β and γ bands, while the vibrational scenario can be proven by an observation of its characteristic quantization resulting from the excitation of a number of vibrational phonons with the same nature.

A.2 Experimental details

In order to study the low- and moderate-spin states in ^{150}Gd we carried out an experiment at iThemba LABS using the ^{150}Sm(^{4}He, 4n)^{150}Gd reaction. The 48 MeV beam of ^{4}He ions, delivered by the Separated-Sector Cyclotron (SSC) [37], was used to bombard a 2.2 mg/cm^2 target of ^{150}Sm. The emitted γ rays were detected using the AFRODITE γ-ray spectrometer [38], comprised of 9 HPGe clover detectors in BGO shields. Data sorting and analysis were carried out using Midas MTsort [39] and RadWare [40] software packages, as described in section 3.

A.3 Experimental results for ^{150}Gd from γ-coincidence analysis

The experimental information on the spectroscopy of ^{150}Gd has been improved. The decay scheme of this nucleus has been extended by about 31 new γ-ray transitions, as shown in Fig. A.4. The transitions do not form rotational bands, but they were tentatively grouped together in sequences. The majority of the new γ rays depopulate high-spin states. In this work only γ-coincidence analysis was carried out. The observed structures and coincidence spectra are presented below. The coincidence spectra were obtained by placing gates on the total projection spectrum shown in Fig. A.5.

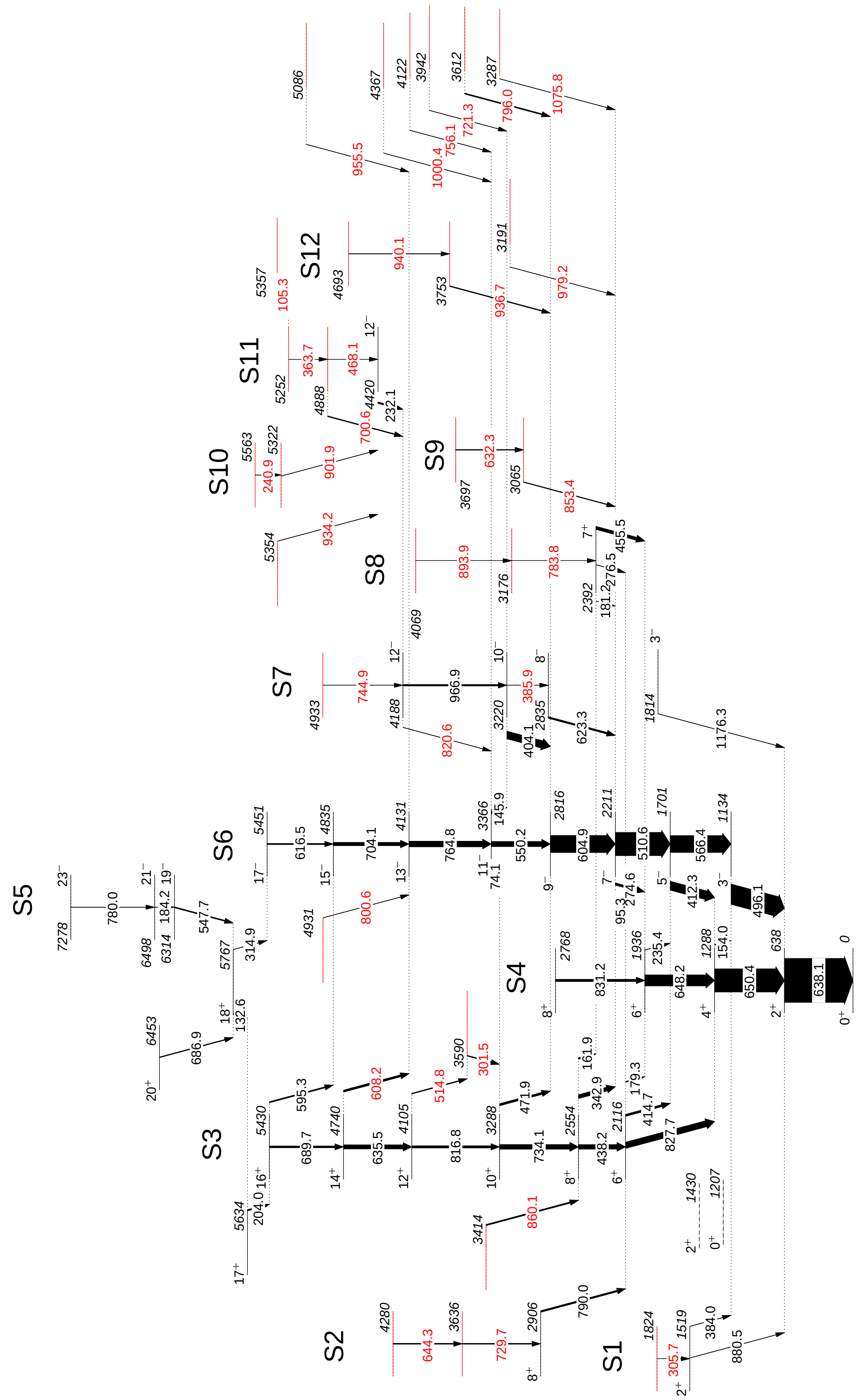

FIGURE A.4: Decay scheme of ^{150}Gd deduced in the present work. New γ-ray transitions and levels are shown in red. The previously reported ones are shown in black. The arrow widths are proportional to the intensity of the γ-ray transitions. The energies are given in keV. The previously reported levels that could not be observed in the current work are shown with dashed line.

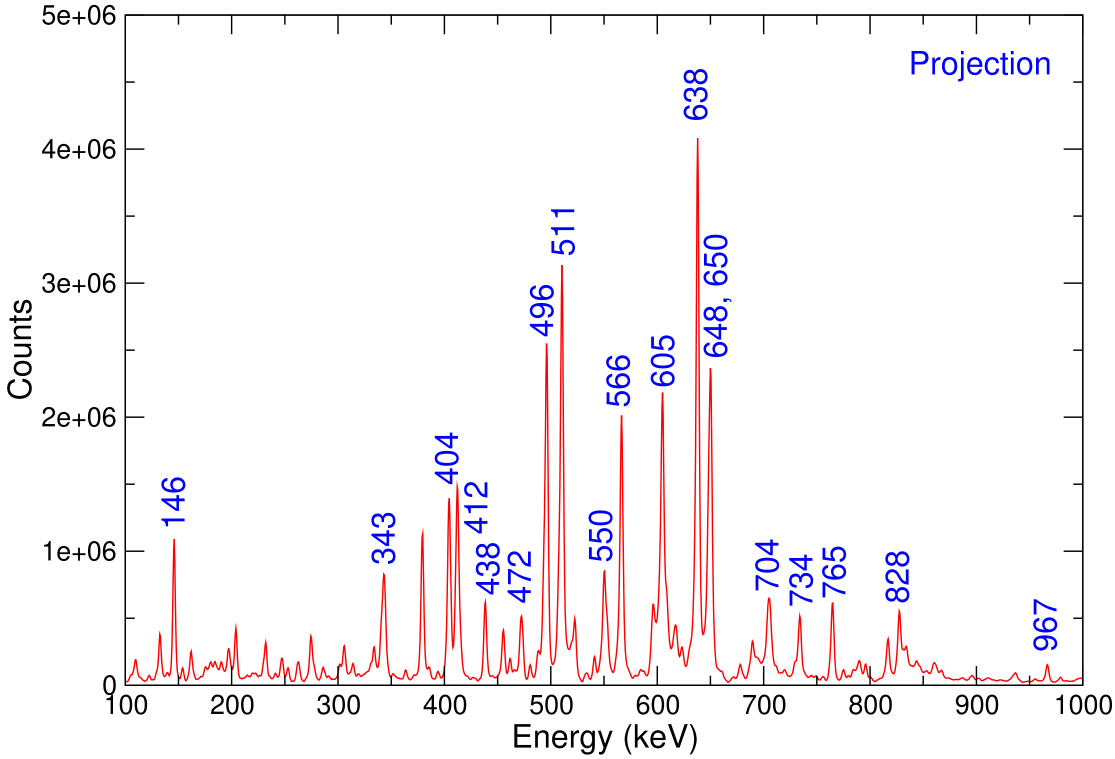

FIGURE A.5: The ungated spectrum from the total projection of the γ-γ matrix, showing the prominent γ-ray peaks of ^{150}Gd.

A.3.1 Previously reported sequences

Sequences 3, 4, 6, and 7 (S3, S4, S6, and S7) have been previously reported [76]. They were also observed in the current study. The present study observes S3 from spin of 6^+ up to spin 16^+. The 6^+ level decays predominantly towards S4 via the 828-keV transition. States above 6^+ decay strongly toward the negative parity levels of S6 through $E1$ transitions. It should be noted that the 12^+ level is the only state of S3 that does not decay to S6. This state instead decays to the newly observed level at 3590 keV via the 515-keV γ-ray transition. This new level also decays to the 10^+ level of S3 through the 302-keV γ-ray. In addition, a new 860-keV transition populating the 8^+ state of S3 was identified, see Fig. A.4.

Sequence 4 is the ground-state structure of ^{150}Gd which is known up to the 8^+ state. A gate made on a member of this structure is shown in Fig. A.6.

Sequence 5 has been previously reported [76]. It develops on top of a 19^- state, and in the current study we observe it up to spin 23^-.

The previously reported S6 is observed up to the 17^- level in the present study. It was interpreted as a structure associated with octupole vibration [77]. The intense transitions of S6 decay strongly towards the ground-state structure. A new transition of 801 keV, feeding the 13^- state of S6, was identified in this work. This new transition is illustrated in the spectrum of Fig. A.7, obtained by placing a gate on the 765-keV transition of S6.

Two new transitions belonging to the previously observed S7 were discovered [76]. This structure is extended by one level at 4933 keV, and by one new 821-keV transition linking this sequence with S6. Figure A.8 shows a spectrum gated on the 967-keV transition of S7, illustrating the newly observed 745-keV transition.

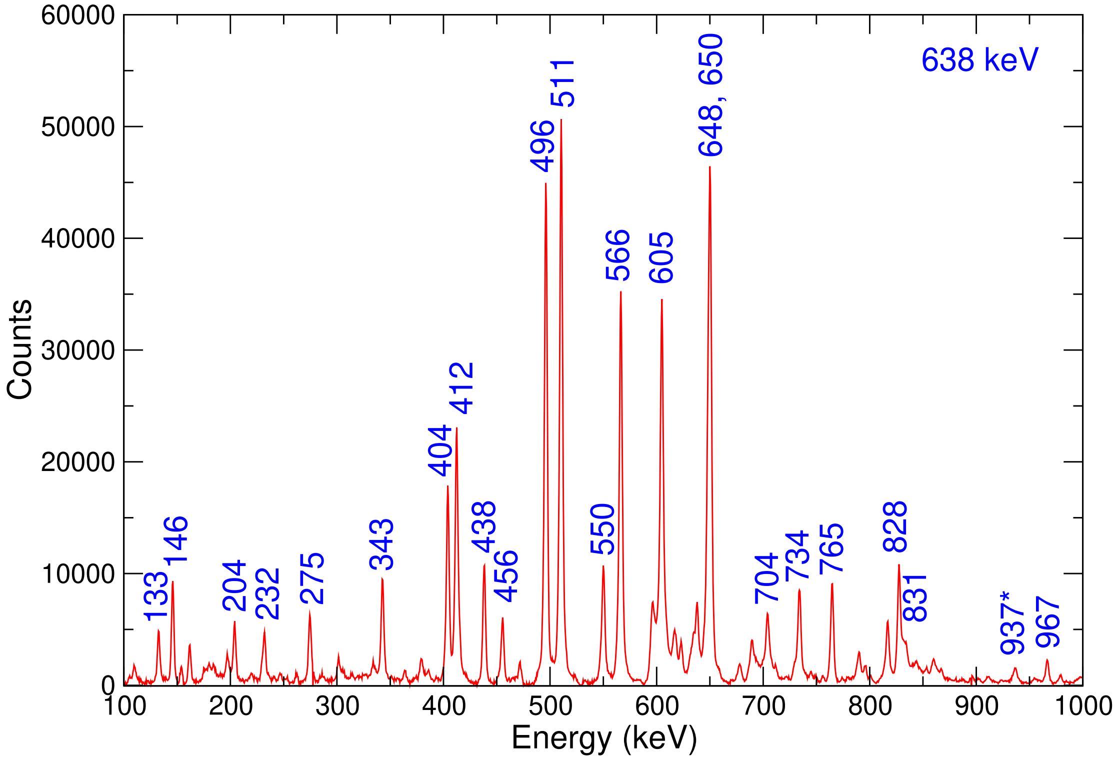

FIGURE A.6: Spectrum showing the γ-ray transitions in coincidence with 638 keV. Members of the ground-state structure are shown in black.

A.3.2 Sequences built on the known states

Sequences 1, 2, 8, and 11 (S1, S2, S8, and S11) are new structures that are built on previously reported states [76, 77]. S1 is a structure built on the known 2_2^+ state. It has only two levels, and three γ-ray transitions. Two of the three transitions were previously reported. They decay out of the 2^+ state of S1 to the 2^+ state of S4 and to the 3^- state of S6. The level at 1824 keV is reported for the first time in this work. It decays via the 306 keV to the 2^+ level.

Two new levels of S2 built on the known level at 2906 keV were identified. This structure is linked to S3 through the 790-keV transition, see Fig. A.4. Sequence 8 is built on the previously observed 7^+ level at 2392 keV [76]. This level decays via the three transitions to the 6^+, 6^+ and 7^- states of sequences 3, 4, and 6, respectively. Two new levels at 3176 and 4069 keV built on this 7^+ known state were identified in the current work.

Sequence 11 is built on the known 12^- level at 4420 keV which decays via the 232-keV

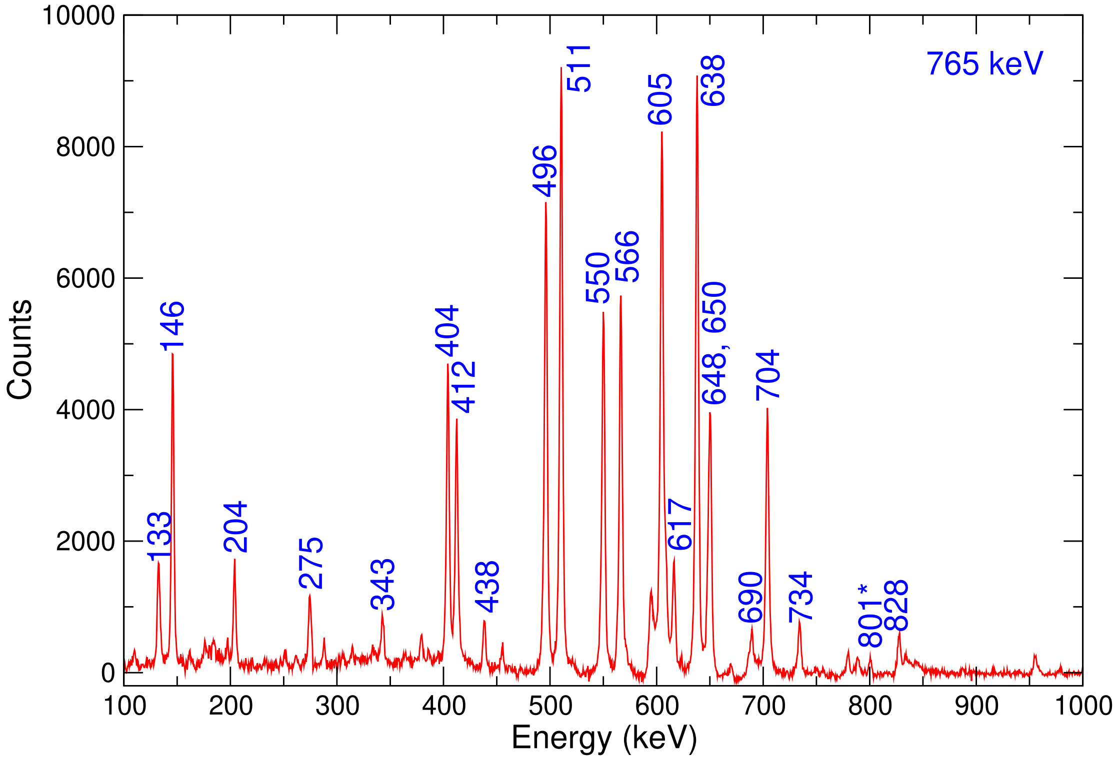

FIGURE A.7: Spectrum showing the γ-ray transitions in coincidence with 765 keV of S6.

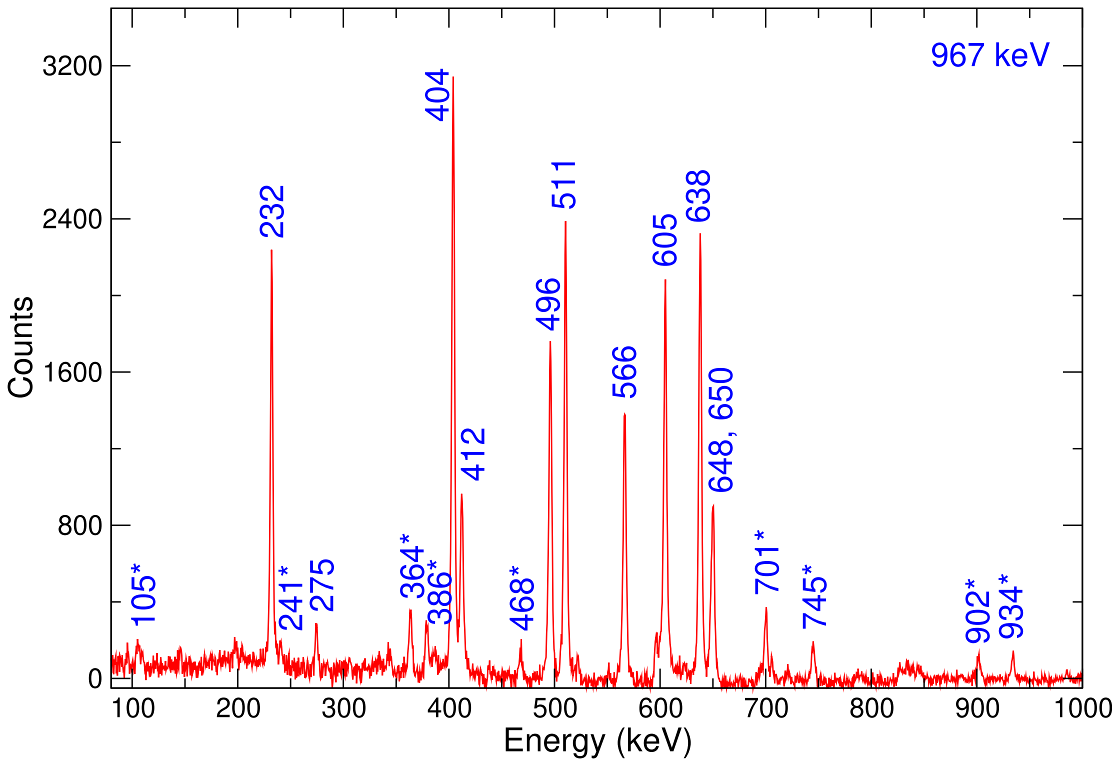

FIGURE A.8: Spectrum showing the γ-ray transitions in coincidence with 967 keV of S7.

transition to the 12^- state of S7. A new member of S11 that decays to S7 was also identified, see A.4. The known 12^- level of S11 is fed by three new γ-ray transitions. A gated spectrum illustrating these new γ-ray transitions is shown in Fig. A.11.

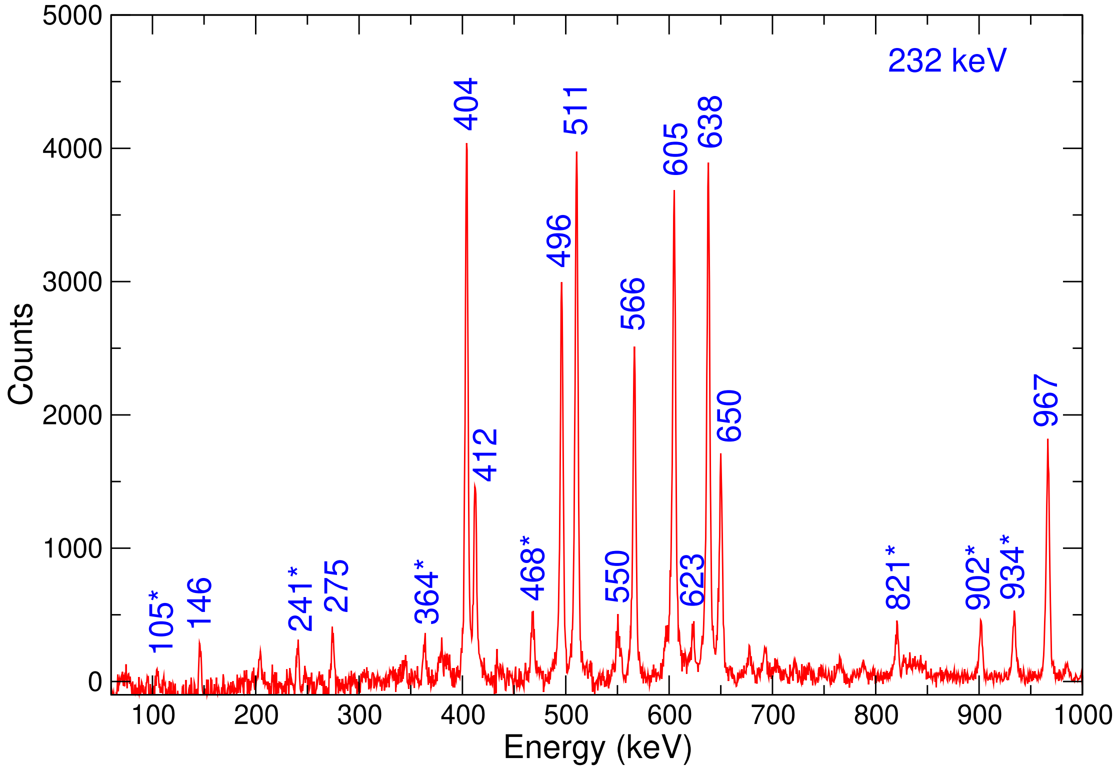

Figure A.9: Gated spectrum showing the new transitions of S11 and those that are in coincidence with 232 keV. New transitions are marked with asterisk.

A.3.3 Sequences built on the new levels

Sequences 9, 10, and 12 (S9, S10, and S12) are reported for the first time in this work. We report two new levels grouped as sequence 9. It decays via the 853-keV transition to S6. A gate on this transition is shown in Fig. A.10. Structure 10 is new, comprises two levels and decays via the 902-keV transition to the previously observed level at 4420 keV. Two levels built above this level were observed up to excitation energy of 5252 keV. This last level is fed by a new 105-keV transition, as shown in the Fig. A.4. New members of this structures are shown in the spectra of Figs. A.8 and A.9.

Sequence 12 was identified for the first time. It is connected to S6 through the 937-keV transition. A spectrum gated on this linking transition is displayed in Fig. A.11. Several new states mainly decaying towards S6 were identified in this research work.

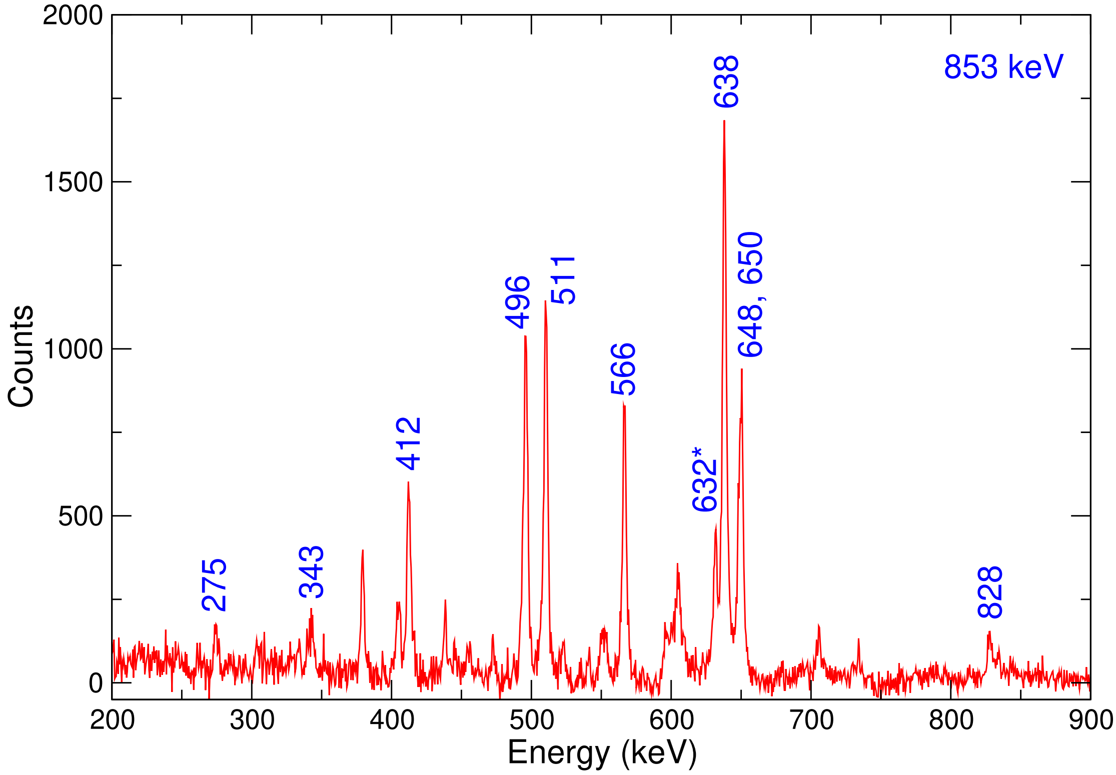

Figure A.10: Coincidence spectrum, gated on the linking 853-keV transition of S10. The new transition is marked with asterisk.

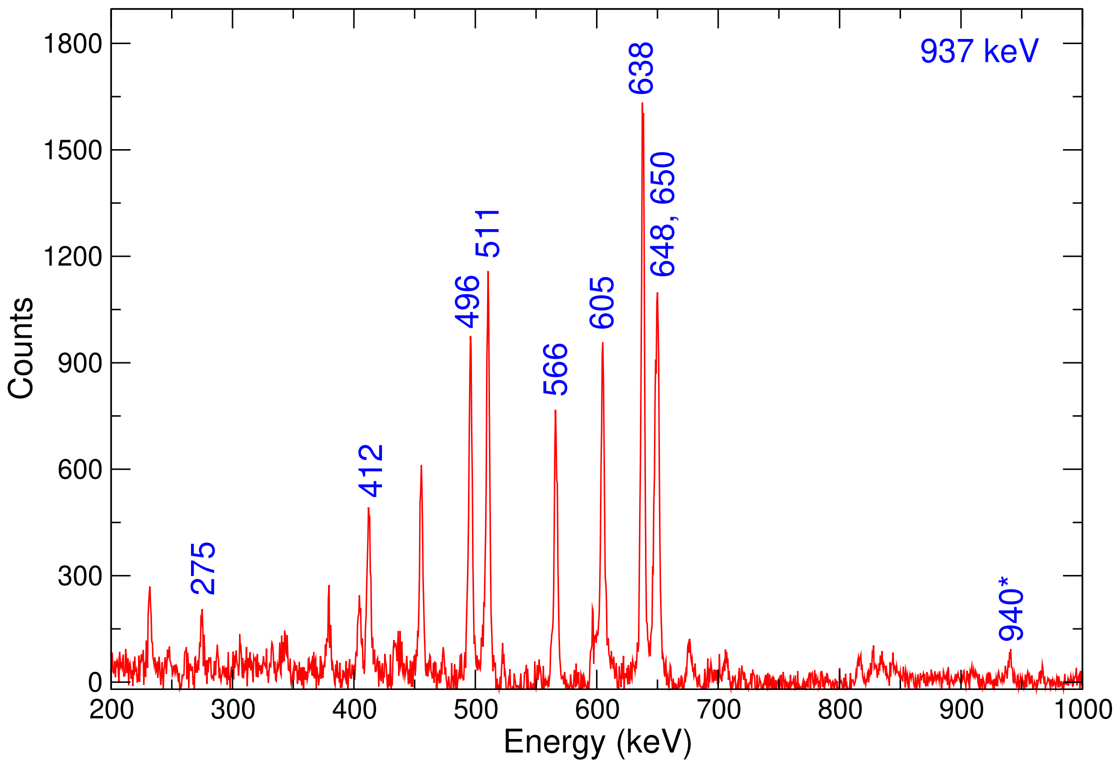

Figure A.11: Gated spectrum on the new 937-keV transition of S12. The new transition is marked with asterisk.

A.4 Summary

The excited states in ^{150}Gd have been studied at iThemba LABS through the ^{150}Sm(^{4}He, 4n)^{150}Gd reaction. The AFRODITE array was used for detection of the γ-rays emitted in the experiment. A number of new γ-ray transitions and new levels at high excitation energy were identified in the present work. The decay scheme of ^{150}Gd has been considerably extended. The data analysis did not produce new information on the low-spin states. For instance the previously observed transitions depopulating the excited 0_2^+ and 2_2^+ states at 1207 and 1430 keV could not be observed in our data. We could also not confirm the presence of the 1062-keV E3 transition previously reported to connect the 5_1^- and 4_1^+ states. A collective $E3$ transition is a strong evidence for the presence of an octupole phonon excitation. While the data did not provide new information on the low-spin states, which was the initial aim of this experiment, many new transitions were identified at high spins. The present study for these transitions was confined to γ-coincidence analysis. The spin and parity assignments for the new states and the possible mode of excitation that generates them will be studied in a follow-up work.

Bibliography

[1] C. Y. Wu *et al.* *Nucl. Phys. A*, 607:178–234, 1996. doi: 10.1016/0375-9474(96)00181-9. URL https://doi.org/10.1016/0375-9474(96)00181-9.

[2] J. M. Allmond, R. Zaballa, A. M. Oros-Peusquens, W. D. Kulp, and J. L. Wood. *Phys. Rev. C*, 78:014302, 2008. doi: 10.1103/PhysRevC.78.014302. URL https://doi.org/10.1103/PhysRevC.78.014302.

[3] J. F. Sharpey-Schafer *et al.* *Eur. Phys. J. A*, 55:15, 2019. doi: 10.1140/epja/i2019-12665-x. URL https://doi.org/10.1140/epja/i2019-12665-x.

[4] R. Gupta *et al.* *Chinese Journal of Physics*, 72:191–206, 2021. doi: 10.1016/j.cjph.2021.04.0231. URL https://doi.org/10.1016/j.cjph.2021.04.0231.

[5] R. D. Bagnell *et al.* *Phys. Lett. B*, 66(2):129–132, 1977. ISSN 0370-2693. doi: https://doi.org/10.1016/0370-2693(77)90157-5. URL https://www.sciencedirect.com/science/article/pii/0370269377901575.

[6] D. G. Burke. *Phys. Rev Lett.*, 73:1899, 1994. doi: 10.1103/PhysRevLett.73.1899. URL https://doi.org/10.1103/PhysRevLett.73.1899.

[7] D. G. Burke. *Phys. Lett. B.*, 406:200, 1997. doi: 10.1016/S0370-2693(97)00658-8. URL https://doi.org/10.1016/S0370-2693(97)00658-8.

[8] Z. P. Li *et al.* *Phys. Rev. C*, 79:054301, 2009. doi: 10.1103/PhysRevC.79.054301. URL https://doi.org/10.1103/PhysRevC.79.054301.

[9] J. Xiang *et al.* *Nucl. Phys. A*, 873:1–16, 2012. doi: 10.1016/j.nuclphysa.2011.10.002. URL https://doi.org/10.1016/j.nuclphysa.2011.10.002.

[10] S. N. T. Majola *et al.* *Phys. Rev. C*, 100:044324, 2019. doi: 10.1103/PhysRevC.100.044324. URL https://doi.org/10.1103/PhysRevC.100.044324.

[11] X. Q. Yang *et al.* *Phys. Rev. C*, 103:054321, 2021. doi: 10.1103/PhysRevC.103.054321. URL https://doi.org/10.1103/PhysRevC.103.054321.

[12] A. S. Davydov and G.F. Philippov. *Nucl. Phys.*, 8:237, 1958. doi: 10.1016/0029-5582(58)90153-6. URL https://doi.org/10.1016/0029-5582(58)90153-6.

[13] S. G. Nilsson. *Binding States of Individual Nucleons in Strongly Deformed Nuclei.* Dan.Mat.Fys.Medd 29, no 16, 1955.

[14] P. B. Semmes and I . Ragnarsson. Proceedings of the international conference on high-spin physics and gamma-soft nuclei. page 500, Pittsburg, 1990.

[15] F. Iachello. *Phys. Rev. Lett.*, 85:3580–3583, 2000. doi: 10.1103/PhysRevLett.85.3580. URL https://link.aps.org/doi/10.1103/PhysRevLett.85.3580.

[16] F. Iachello. *Phys. Rev. Lett.*, 87:052502, 2001. doi: 10.1103/PhysRevLett.87.052502. URL https://link.aps.org/doi/10.1103/PhysRevLett.87.052502.

[17] L. Wilets and M. Jean. *Phys. Rev.*, 102:788–796, 1956. doi: 10.1103/PhysRev.102.788. URL https://link.aps.org/doi/10.1103/PhysRev.102.788.

[18] A. S. Davydov and A. A. Chaban. *Nuclear Physics*, 20:499–508, 1960. ISSN 0029-5582. doi: https://doi.org/10.1016/0029-5582(60)90191-7. URL https://www.sciencedirect.com/science/article/pii/0029558260901917.

[19] D. H. Feng, G. Robert, and S. R Deans. *Phys. Rev. C*, 23:1254–1258, 1981. doi: 10.1103/PhysRevC.23.1254. URL https://link.aps.org/doi/10.1103/PhysRevC.23.1254.

[20] K. Pomorski and J. Dudek. *Phys. Rev. C*, 67:044316, 2003. URL https://doi.org/10.1103/PhysRevC.67.044316.

[21] C.F. von Weizsäcker. *Z. Phys*, 96:431, 1935. URL https://doi.org/10.1007/BF01337700.

[22] H. A. Bethe and R. F. Bacher. *Rev. Mod. Phys*, 8:82, 1936. URL https://doi.org/10.1103/RevModPhys.8.82.

[23] M. G. Mayer. *Phys. Rev.*, 78:16–21, 1950. doi: 10.1103/PhysRev.78.16. URL https://link.aps.org/doi/10.1103/PhysRev.78.16.

[24] M. G. Mayer. *Phys. Rev.*, 78:22–23, 1950. doi: 10.1103/PhysRev.78.22. URL https://link.aps.org/doi/10.1103/PhysRev.78.22.

[25] O. Haxel *et al.* *Phys. Rev.*, 75:1766–1766, 1949. doi: 10.1103/PhysRev.75.1766.2. URL https://link.aps.org/doi/10.1103/PhysRev.75.1766.2.

[26] M. G. Mayer. *Phys. Rev.*, 74:235–239, 1948. doi: 10.1103/PhysRev.74.235. URL https://link.aps.org/doi/10.1103/PhysRev.74.235.

[27] A. Andreyev *et al.* *Nature*, 405:430–433, 2000. doi: doi.org/10.1038/35013012. URL https://doi.org/10.1038/35013012.

[28] A. Bohr and B. R. Mottelson. *Nuclear Structure, Volume .II.* Singapore: Word Scientific, 1998.

[29] W. Greiner and Joachim A. Maruhn. *Nuclear Models.* Springer and Berlin and Heidelberg, 1996. URL https://link.springer.com/book/10.1007/978-3-642-60970-1.

[30] J. M. Eisenberg and W. Greiner. *Nuclear Models*, volume 1. North Holland Publishing Company, 1970.

[31] D. J. Rowe and J. L. Wood. *Fundamentals of Nuclear Models: Foundational Models.* World Scientific, 2010.

[32] R. F. Casten. *Nuclear Structure From A Simple Perspective.* Oxford University Press, Oxford, 1990.

[33] K. S. Krane. *Introductory Nuclear Physics.* John Wiley & Sons. inc., 1987.

[34] F. S. Stephens. *Rev. Mod. Phys*, 47:43, 1975. URL https://doi.org/10.1103/RevModPhys.47.43.

[35] S. M. Harris. *Phys. Rev.*, 138:B509–B513, 1965. doi: 10.1103/PhysRev.138.B509. URL https://link.aps.org/doi/10.1103/PhysRev.138.B509.

[36] P. J. Celliers *et al.* Present status and new developments at nac", epac'2000. page 533, Vienna, June, 2000.

[37] J. L. Conradie *et al.* New priorities and developments at nac", proc. of the 16th int. conf. on cyclotrons and their applications. volume 600 of *AIP conf. Proc.*, page 120, East Lansing, May, 2001.

[38] J. F. Sharpey-Schafer. *Nucl. Phys. News*, 14:5, 2004. doi: 10.1080/10506890491034686. URL https://doi.org/10.1080/10506890491034686.

[39] URL http://npg.dl.ac.uk/MIDAS/base.html.

[40] D. C. Radford. *Nucl. Instr. Meth.*, 361:297, 1995.

[41] D. C. Radford. (2000). URL http://radware.phy.ornl.gov/rw/esclev/-esclev.html.

[42] R. A. Bark. (2011). URL http://www.tlabs.ac.za/wp-content/uploads/pdf/RobWorkshop2011.pdf.

[43] URL http://lise.nscl.msu.edu/pace4.html(2016).

[44] T. S. Dinoko. *PhD. thesis, SEARCH FOR LOW SPIN COLLECTIVE STRUCTURES IN ^{158}Er and ^{159}Er, University of the Western Cape*, 2014.

[45] R. Bock. Heavy ion collisions. North Holland Publishing Company, page 2, Amsterdam, 1980.

[46] S. S. Ntshangase. *PhD. thesis, DEVELOPMENT OF A RECOIL DETECTOR AND THE STUDY OF EXOTIC ASYMMETRIC SHAPES IN NUCLEI, University of Cape Town*, 2011.

[47] J. H. L. Mott and J. M. Daniel. *Clin. Oncol.*, 33:451–454, 2021. doi: 10.1016/j.clon.2021.02.004. URL https://doi.org/10.1016/j.clon.2021.02.004.

[48] S. N. T. Majola. *PhD. thesis, EXPLORING THE SPECTROSCOPY OF VIBRATIONAL LEVELS IN THE 160 MASS REGION, University of Cape Town*, 2015.

[49] J. H. Lee *et al. J. of Kor. Phys. Soc.*, 40:793, 2002.

[50] C. Wheldon *et al. Nucl. Phys. A*, 652:103–131, 1999. doi: 10.1016/S0375-9474(99)00160-8. URL https://doi.org/10.1016/S0375-9474(99)00160-8.

[51] R. Spanhoff *et al. Phys. Rev. C*, 18:1, 1978. doi: 10.1103/PhysRevC.18.493. URL https://doi.org/10.1103/PhysRevC.18.493.

[52] C. M. Baglin. *Nucl. Data Sheets*, 99:1, 2003. doi: 10.1016/S0090-3752(88)80025-5. URL https://doi.org/10.1016/S0090-3752(88)80025-5.

[53] R. C. Thompson *et al. Nucl. Phys. A*, 242:1–12, 1975. doi: doi.org/10.1016/0375-9474(75)90029-9. URL https://doi.org/10.1016/0375-9474(75)90029-9.

[54] P. E. Garrett. *J. Phys. G*, 27:R1, 2001. doi: 10.1088/0954-3899/27/1/201. URL https://doi.org/10.1088/0954-3899/27/1/201.

[55] J. F. Sharpey-Schafer *et al. Eur. Phys. J. A*, 47:6, 2011. doi: 10.1140/epja/i2011-11006-7. URL https://doi.org/10.1140/epja/i2011-11006-7.

[56] D. Bucurescu *et al. Phys. Rev. C*, 73:064309, 2006. doi: 10.1103/PhysRevC.73.064309. URL https://doi.org/10.1103/PhysRevC.73.064309.

[57] L. Mdletshe *et al. Eur. Phys. J. A*, 54:176, 2018. doi: 10.1140/epja/i2018-12613-4. URL https://doi.org/10.1140/epja/i2018-12613-4.

[58] W. D. Kulp *et al. Phys. Rev. C*, 77:061301, 2008. doi: 10.1103/PhysRevC.77.061301. URL https://doi.org/10.1103/PhysRevC.77.061301.

[59] S. N. T. Majola *et al.* *Phys. Rev. C*, 91:034330, 2015. doi: 10.1103/PhysRevC.91.034330. URL https://doi.org/10.1103/PhysRevC.91.034330.

[60] N. Pietralla and O. M. Gorbachenko. *Phys. Rev. C*, 70:011304(R), 2004. doi: 10.1103/PhysRevC.70.011304. URL https://doi.org/10.1103/PhysRevC.70.011304.

[61] J. Smallcombe *et al.* *Phys. Lett. B*, 732:161, 2014. doi: 10.1016/j.physletb.2014.03.034. URL https://doi.org/10.1016/j.physletb.2014.03.034.

[62] W. D. Kulp *et al.* *Phys. Rev. C*, 76:034319, 2007. doi: 10.1103/PhysRevC.76.034319. URL https://doi.org/10.1103/PhysRevC.76.034319.

[63] S. P. Bvumbi *et al.* *Phys. Rev. C*, 87:044333, 2013. doi: 10.1103/PhysRevC.87.044333. URL https://doi.org/10.1103/PhysRevC.87.044333.

[64] S. Jehangir *et al.* *Phys. Rev. C*, 97:014310, 2018. doi: 10.1103/PhysRevC.97.014310. URL https://doi.org/10.1103/PhysRevC.97.014310.

[65] G. L. Zimba *et al.* *Eur. Phys. J. A*, 54:59, 2018. doi: 10.1140/epja/i2018-12496-3. URL https://doi.org/10.1140/epja/i2018-12496-3.

[66] J. Ollier *et al.* *Phys. Rev. C*, 83:044309, 2011. doi: 10.1103/PhysRevC.83.044309. URL https://doi.org/10.1103/PhysRevC.83.044309.

[67] J.F. Sharpey-Schafer *et al.* Evolution of γ bands. Proc. XLIX Int. Winter Meeting on Nucl. Phys., Bormio, Italy, 2011.

[68] J. F. Sharpey-Schafer *et al.* *Nucl. Phys. A*, 834(1):45c–49c, 2010. ISSN 0375-9474. doi: https://doi.org/10.1016/j.nuclphysa.2010.01.014. URL https://www.sciencedirect.com/science/article/pii/S0375947410000151.

[69] M. A. Sithole *et al.* *Eur. Phys. J. A*, 55:178, 2019. doi: 10.1140/epja/i2019-12866-3. URL https://doi.org/10.1140/epja/i2019-12866-3.

[70] R. A. Bark *et al.* Studies of positive-parity low-spin states in the a = 150 region. *EPJ Web Conf.*, 178:02012, 2018. doi: 10.1051/epjconf/201817802012. URL https://doi.org/10.1051/epjconf/201817802012.

[71] S. N. T. Majola *et al.* *Phys. Rev. C*, 101:044312, 2020. doi: 10.1103/PhysRevC.101.044312. URL https://link.aps.org/doi/10.1103/PhysRevC.101.044312.

[72] P. B. Semmes and I . Ragnarsson. Future directions in nuclear physics with 4π gamma detection systems of the new generation. volume 259 of *AIP Conf. Proc.*, page 566, 1992.

[73] J. M. Rees *et al.* *Phys. Rev. C*, 83:044314, 2011. doi: 10.1103/PhysRevC.83.044314. URL https://doi.org/10.1103/PhysRevC.83.044314.

[74] E. A. McCutchan *et al.* *Phys. Rev. C*, 76:024306, 2007. doi: 10.1103/PhysRevC.76.024306. URL https://doi.org/10.1103/PhysRevC.76.024306.

[75] K. Krien *et al.* *Phys. Rev. C*, 7:2484–2499, 1973. doi: 10.1103/PhysRevC.7.2484. URL https://link.aps.org/doi/10.1103/PhysRevC.7.2484.

[76] D. R. Haenni and T. T. Sugihara. *Phys. Rev. C*, 16:120–131, 1977. doi: 10.1103/PhysRevC.16.120. URL https://link.aps.org/doi/10.1103/PhysRevC.16.120.

[77] D. R. Haenni and T. T. Sugihara. *Phys. Rev. C*, 16:1129–1145, 1977. doi: 10.1103/PhysRevC.16.1129. URL https://link.aps.org/doi/10.1103/PhysRevC.16.1129.